Control of plasma profiles and stability through localised Electron Cyclotron Current Drive

Control of plasma profiles and stability through localised Electron Cyclotron Current Drive

De beheersing van plasma-profielen en -instabiliteiten door toepassing van cyclotron stroomaandrijving

(met een samenvatting in het Nederlands)

Proefschrift

ter verkrijging van de graad van doctor aan de Universiteit Utrecht op gezag van de rector magnificus, prof.dr. W.H. Gispen, ingevolge het besluit van het college voor promoties in het openbaar te verdedigen op donderdag 22 juni 2006 des middags te 14.30 uur

door

Oleksiy Merkulov

geboren op 27 augustus 1980
te Tsjernigow, Oekraïne

Promotor : Professor Dr. F.C. Schüller
Co-promotor : Dr. E. Westerhof

The work described in this thesis was performed as part of the research programme of the *'Stichting voor Fundamenteel Onderzoek der Materie'* (FOM) with financial support from the *'Nederlandse Organisatie voor Wetenschappelijk Onderzoek'* (NWO) and EURATOM, and was carried out at the Institut für Plasmaphysik, Forschungszentrum Jülich, Germany.

pentru Mariuţa, Elena şi Constantin

Contents

Chapter 1

Introduction

The work presented in this thesis has been conducted within the research field of high temperature plasma physics.

1.1 Basics of nuclear fusion

Two positively charged light nuclei can fuse to a heavier nucleus when they are so close together that they overcome their mutual electrostatic repulsion. In such fusing process a mass defect, Δm, arises that is transformed into energy: $E = \Delta m c^2$. This process is the base for energy production by controlled thermonuclear fusion. If the released energy is at least partially given to the kinetic energy of the light nuclei such that they on their turn will fuse one has reached a situation of a self-maintained 'burn' process. There are several possible fusion reactions that are of interest for controlled thermonuclear fusion. The reactions which involve hydrogen isotopes, deuterium D and/or tritium T, are the most interesting for the nuclear fusion, since they have a large cross-section of the reaction and release a significant amount of energy:

$$\mathrm{D} + \mathrm{T} \longrightarrow {}^4\mathrm{He}(3.5\,\mathrm{MeV}) + \mathrm{n}(14.1\,\mathrm{MeV}) \tag{1.1}$$

$$\mathrm{D} + \mathrm{D} \longrightarrow \begin{cases} \mathrm{T}(1.0\,\mathrm{MeV}) + \mathrm{p}(3.0\,\mathrm{MeV}) \\ {}^3\mathrm{He}(0.8\,\mathrm{MeV}) + \mathrm{n}(2.5\,\mathrm{MeV}) \end{cases} \tag{1.2}$$

$$\mathrm{D} + {}^3\mathrm{He} \longrightarrow {}^4\mathrm{He}(3.7\,\mathrm{MeV}) + \mathrm{p}(14.6\,\mathrm{MeV}) \tag{1.3}$$

The first reaction is the primary candidate for use in a future reactor. It has the biggest cross-section and releases very energetic 14 MeV neutrons. The state of matter in which 'burn' by fusion can occur is a quasi-neutral gas of ions and electrons which is called plasma. The temperatures required to surpass the potential barrier associated with the Coulomb interaction are typically 10^8 to 10^9 K. The Sun is a natural example of a working thermonuclear plasma reactor. The required density and temperature for the fusion reactions inside the Sun are reached due to the gravitational force, which balances the plasma's tendency to expand. There is no possibility to confine plasma with the help of gravitational forces on Earth. Moreover, the hot plasma cannot be in contact with a material wall. Such contact can be prevented by the application of

magnetic field: magnetic confinement. Charged particles follow the magnetic field lines and, therefore, a plasma can be kept within a vacuum chamber if no field lines leave this chamber.

Up to now the tokamak is the most promising and successful device to implement the magnetic confinement scheme. Figure 1.1 schematically shows the main components of the tokamak and its magnetic field structure. The plasma in the tokamak is confined inside a vacuum vessel with a toroidal shape. The toroidal magnetic field is generated by coils surrounding the vessel. However, the toroidal magnetic field only is not enough to confine the plasma since the electrons and ions experience a common drift in the horizontal direction under the influence of charge separation in the direction vertical to the plane of the torus. Consequently, the plasma would rapidly expand in the direction of the large major radius. This effect can be compensated by a poloidal magnetic field which results from a toroidal plasma current. The poloidal field causes the total field lines to connect top to bottom of the the toroidal surfaces thereby annihilating the charge separation. In the tokamak the plasma current is induced through a large transformer where the plasma is the secondary circuit of this transformer. The sum of the poloidal and toroidal magnetic fields results in helical magnetic field lines which lie on nested magnetic surfaces.

The presented work was performed within the framework of the "Trilateral Euregio Cluster" (TEC) agreement, which combines the efforts of the EURATOM associations from the Netherlands, Belgium and Germany in common fusion research. The experimental research is based at the TEXTOR (Tokamak EXperiment for Technology Oriented Research) tokamak at the Institut für Plasmaphysik, Forschungszentrum Jülich, Germany. The TEXTOR tokamak has a major radius $R_0 = 1.75$ m, a minor radius $a = 0.46$ m and can sustain a plasma discharge for up to 10 s. One of the features of the TEXTOR tokamak is that it has a circular plasma cross-section, which simplifies the theoretical predictions.

1.2 Challenges of tokamak physics

There are a number of issues which complicate the simple idea of magnetic confinement of the plasma inside the torus. The successful operation of a thermonuclear reactor is based on a burning plasma in a steady state. The plasma is prone to various instabilities which perturb the equilibrium, degrade the plasma performance and, finally, may lead to a plasma disruption. Some dangerous instabilities can be avoided by careful design of the plasma scenario. However, some instabilities, such as sawtooth oscillations, are often present in most real plasmas and potentially can trigger more dangerous ones, such as a neoclassical tearing mode. The first challenge is to develop control schemes over the plasma instabilities. Such a system normally includes the detection component—which is a separate challenge in itself—and an active-control component. Control over various plasma instabilities has been successfully demonstrated on various machines by means of additional heating and non-inductive current drive.

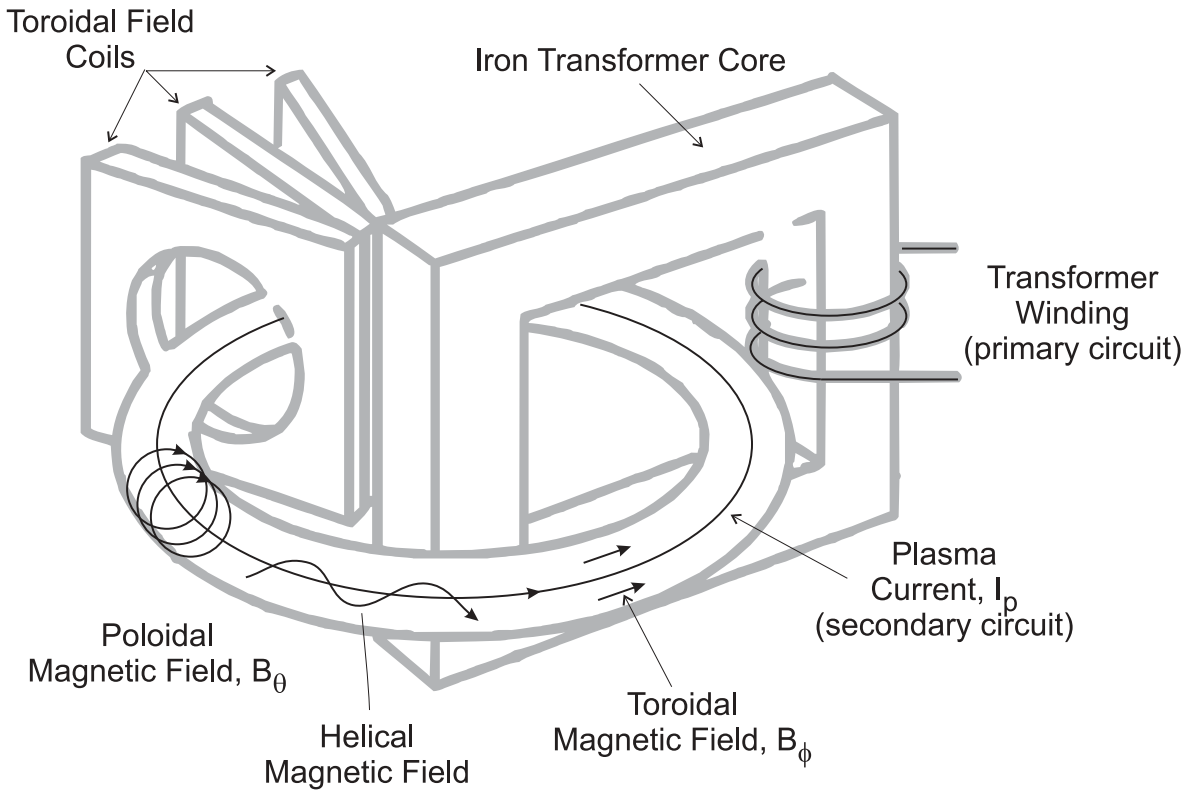

Figure 1.1: Schematic drawing of the tokamak with the magnetic field structure inside the vacuum vessel.

Even when these kind of macroinstabilities are brought under control the plasma is in a state of turbulence due to microinstabilities. This turbulence leads to an enhanced heat conduction cooling down the plasma. The art of developing a self-sustained burning plasma is therefore directly related to reducing the turbulence heat conduction to accepted levels. Also precise control of plasma profiles is needed.

Both challenges require proper usage of additional heating methods and current drive. It is obvious that a future reactor will have additional heating as a part of the design. Different scenarios involving additional heating methods have been investigated and there are many more to study. Moreover, the simultaneous use of several heating methods can lead to synergistic effects and requires a proper theoretical description.

Next item is the particle exhaust, which is necessary to keep the core of the plasma hot and free of impurities. The present concept, so-called divertor, is that plasma has to have an X-point which is created in the equilibrium, where the magnetic field is zero, and is located close to the plasma edge. Such an X-point divides the plasma in the large bulk area with closed magnetic surfaces surrounded by a layer in which field lines end up on the divertor plates. Particles diffuse through the last closed magnetic surface and end up on the divertor plates. These plates have to be designed to withstand high heat loads for a long period of time. The design of the divertor requires a thorough knowledge and deep understanding of the plasma interaction with material boundaries.

There are more problems to be solved on the way to an economically feasible thermonuclear reactor and their detailed outline can be found, for instance, on the web site of the ITER project [1]. The ITER tokamak is the next logical step taken by the fusion community on the international level towards controlled nuclear fusion. The main objective of this project is to demonstrate that it can generate 10 times more power than the total input power.

1.3 State of the art

Here we discuss the relevance of this thesis to the present achievements in tokamak physics. First, we start with the well known internal instability, the sawtooth instability. The sawtooth oscillations are well studied and observed in many tokamaks. Modest sawteeth oscillations are helpful in a burning plasma to expel Helium 'ash' created by the burn process in the centre of the plasma. Too large sawteeth can induce damaging other macroinstabilities like neoclassical tearing modes (NTM) or in the worst case plasma disruption. Sawteeth oscillations are caused by magnetic topology in the core of the plasma as a result of the current distribution. Because of the importance of this instability in future burning plasmas, it requires methods for active control of the current density profile in the plasma. Plasma current can be driven in the classical (Ohm's) way by applying an electric field on a conductive medium such as plasma itself. Such a driving electric field can, in a toroidal system, only be induced by transformer action, i.e. inductive current drive. However, current can also be driven by injection of neutral beams or by microwave radiation, i.e. non-inductive current drive. The sawtooth period control with the help of non-inductive current drive has been realised and demonstrated on several machines, such as ASDEX-Upgrade [3] and JET [2]. However, there is no systematic study in order to determine what is a minimum or necessary requirement for the current drive to perform sawtooth control. Following Porcelli's model [4] for the sawtooth period, the critical value of the shear at the $q = 1$ surface determines the moment of the crash. The shear is a measure for the change in direction of the magnetic field lines as a function of position in the plasma. Chapter 4 presents a simplified model for the shear evolution just after the sawtooth crash in the presence of non-inductive current drive. The purpose of this model is to provide simple criteria for the position, width and amount of the applied non-inductive current. These criteria are necessary to have a substantive impact on the evolution of the shear and, consequently, on the sawtooth period. The derived criterion is then used to analyse the experiments which study the effects of the electron cyclotron current drive (ECCD) on the sawtooth period.

The next topic is the current diffusion calculations during ECCD. The standard approach is to take into account the non-inductive current as a contribution to Ohm's law and use the neoclassical plasma resistivity. However, it has been reported that there is an observable synergy between ECCD and the inductive current [5, 6]. Non-inductive current is carried by electrons and follows from non-Maxwellian part of velocity distribution. This distribution can be calculated by means of a Fokker-Planck code involving both the electric field and the microwave radiation. Chapter 5 derives and discusses

the model which couples the Fokker-Planck code and the magnetic diffusion calculations in a self-consistent manner. In this way, the plasma resistivity is derived on the basis on the Fokker-Planck code and, therefore, accounts for effects of the non-Maxwellian distribution of the electrons. The parallel electric field plays the role of the link between the current diffusion and the evolution of the momentum distribution function. The results are then compared with the standard method and Harvey's non-linearity criterion is adopted to indicate the presence of substantial synergy between the ECCD and the inductive current.

1.4 Contributions by this thesis

Chapter 2 introduces numerical codes—which have been used extensively throughout the presented work—and the underlying physical concepts. It begins with the ASTRA transport code, which solves the set of transport equations, and calculates various evolutions of plasma parameters such as density and temperature. Next, the physical concepts of plasma equilibrium—a solution of the so-called Grad-Shafranov equation—and the transport set of equations, as implemented in the ASTRA code, are outlined. The propagation and absorption of electron cyclotron waves (ECW) in the plasma are treated using the geometric optics (GO) approximation and with the beam tracing (BT) technique. The GO approximation provides a set of ordinary differential equations, whose numerical implementation is straightforward. However, this method does not take into account the wave properties, such as diffraction, of the propagating ECW beam. The diffraction of the beam is particulary important in the region around the focal point of the beam where GO predicts a zero width of the beam leading to infinite beam power density. The BT approach takes advantage of some GO assumptions, such as a weak spatial dependence of the propagating wave, yet keeps the diffraction properties of the waves. The GO approximation and the BT technique are realised in the TORAY ray tracing code and the TORBEAM beam tracing code, respectively. The TORAY code can be coupled with the Fokker-Planck code to provide a very accurate estimation of the driven current but at the cost of computing time. On the contrary, the TORBEAM code is very practical in calculating the absorption profile and the estimated current drive, on the basis of experimental profiles, in a reasonable time.

Chapter 3 discusses the theoretical models given in literature for the internal plasma instability which is known as 'sawtooth' instability. Sawtooth oscillations are periodic oscillations of the central temperature and density. A slow rise of the central temperature called the 'ramp phase' is followed by a fast drop or the sawtooth 'crash'. The sawtooth crash is triggered by the instability of the internal kink mode with toroidal and poloidal n=1, m=1 numbers, respectively. During the crash the plasma current, particles and energy in the central region—up to a certain radius—are redistributed, resulting in almost flat profiles. The theoretical description of the sawtooth oscillation is divided in two parts. First, Kadomtsev's model of the fast magnetic reconnection during the sawtooth crash is considered. This model defines the way the magnetic flux reconnects during the crash and allows the calculation of final profiles for the magnetic flux. Second, the sawtooth trigger model is outlined. This model, derived by Porcelli,

defines the threshold for the onset of the internal kink mode and establishes the set of conditions for the plasma potential energy to trigger the internal kink instability. For some plasma conditions the threshold criterion can be written in terms of a critical shear at the $q = 1$ surface, above which the internal resistive kink is triggered. Finally, an application of Porcelli's model to typical TEXTOR plasma conditions is presented.

In Chapter 4 the effects on the sawtooth period by localised non-inductive current drive are studied. According to Porcelli's model presented in Chapter 3 the sawtooth crash is triggered when the magnetic shear at the $q = 1$ surface exceeds a critical value. This critical value depends on the plasma parameters, such as local pressure gradient length, temperature and density. The sawtooth period control can be realised by changing the shear at the $q = 1$ surface. The localised non-inductive current drive as a result of ECW injection is used to affect the shear evolution. A simple theoretical model, based on the poloidal field evolution equation, is derived and a scan throughout a wide range of current drive parameters is performed. This simple model is also compared with a full transport model, which includes a more complete simulation of the temperature evolution. As a result, a simple requirement for the amount of non-inductive current for sawtooth control is proposed. Furthermore, sawtooth behaviour in discharges with identical heating profiles but different current drive efficiencies has been compared with experimental results. In both the cases of co- and counter-current drives the anticipated effects of the localised current drive are confirmed.

Chapter 5 investigates the current penetration in the presence of electron cyclotron current drive (ECCD) on the resistive time scale with a full Fokker-Planck model which includes a self-consistent calculation of the parallel electric field. The existence of synergy between the inductive electric field and the non-inductive current drive invalidates the applicability of Ohm's law, $j - j_{\mathrm{cd}} = \sigma E$, in its common approximation where σ is the neoclassical conductivity for a thermal plasma. The parallel electric field in this case can be obtained from the full Fokker-Planck calculations which in this version include a model for the magnetic diffusion. The proposed solution is to obtain at every time step of the Fokker-Planck model a self-consistent approximation to the plasma resistivity. This resistivity is used in the parallel current diffusion calculation in order to obtain the inductive electric field at the next time step. The results of these Fokker-Planck calculations, including the self-consistent evolution of the inductive electric field, are presented. The synergy between the inductive electric field and the ECCD leads to a number of interesting results which cannot be obtained with the standard model—which considers the neoclassical resistivity of the plasma without a concurrent microwave field and a separate Fokker-Planck calculations for a given microwave field but without a concurrent electric field.

Finally, Chapter 6 is dedicated to experimental observations of the current ramp-up phase in the presence of additional heating. Two sets of experiments, aimed at different aspects of the plasma behaviour, are presented. The first set of discharges was performed with the preliminary 110 GHz electron cyclotron resonance heating (ECRH) system and was concerned with the build up of electron transport barriers during the ramp-up phase. The 140 GHz ECRH system assisted in the second set of experiments in order to achieve quiet current ramp-up with minimal MHD activity. Current penetration calculations were performed on both sets using the ASTRA transport code.

Good agreement between the ASTRA calculations and experiment is found as long as no substantial MHD activity is present in the plasma. Under these circumstances ASTRA is proven to be an excellent tool for predicting current diffusion phenomena and operating scenarios for current ramp-up of tokamak plasmas.

1.5 List of related publications and presentations

The list of publications and conference contributions made within the framework of this thesis research is given below.

Journal publications

1. **"Sawtooth period control by localized non-inductive current drive"**, A. Merkulov, E. Westerhof, F.C. Schüller, M. R. de Baar, A. Krämer-Flecken, Y. Liang, and TEXTOR Team, submitted to Nuclear Fusion
   Chapter 4

2. **"Fokker-Planck modelling of Electron Cyclotron Current Drive including self-consistent magnetic diffusion"**, A. Merkulov, E. Westerhof, F.C. Schüller, submitted to Plasma Physics and Control Fusion
   Chapter 5

3. **"Electron Cyclotron Resonance Heating on TEXTOR"**, E. Westerhof, J.A. Hoekzema, G.M.D. Hogeweij, R.J.E. Jaspers, F.C. Schüller, C.J. Barth, W.A. Bongers, A.J.H. Donné, P. Dumortier, A.F. van der Grift, J.C. van Gorkom, D. Kalupin, H.R. Koslowski, A. Krämer-Flecken, O.G. Kruijt, N.J. Lopes Cardozo, P. Mantica, H.J. van der Meiden, A. Merkulov, A. Messiaen, J.W. Oosterbeek, T. Oyevaar, A.J. Poelman, R.W. Polman, P.R. Prins, J. Scholten, A.B. Sterk, C.J. Tito, V.S. Udintsev, B. Unterberg, M. Vervier, G. van Wassenhove, and TEC Team, Nuclear Fusion 43 (2003) 1371
   Chapter 6

Conference/Workshop proceedings

1. **"Fokker-Planck modelling of Electron Cyclotron Current Drive including magnetic diffusion self-consistently"**, A. Merkulov, E. Westerhof, F.C. Schüller, 11th European Fusion Theory Conference, Aix en Provence, 26-28 September 2005

2. **"Sawtooth period control by localized non-inductive current drive"**, A. Merkulov, F.C. Schüller, E. Westerhof, M.R. de Baar, A. Krämer-Flecken, Y. Liang, and TEXTOR Team, "Theory of Fusion Plasmas", Proceedings of Joint Varenna-Lausanne Int. Workshop on Theory of Fusion Plasmas, Varenna, Italy, August 30 - September 3, 2004, J.W. Connor, O. Sauter, and E. Sindoni (Editors), Societa Italiana di Fisica, Bologna, 2004, p. 279.

3. **“Electron transport barriers in TEXTOR plasmas”**, R. Jaspers, G.M.D. Hogeweij, A. Merkulov, E.Westerhof, F.C. Schüller, A.J.H. Donné, I.Classen, M.R. de Baar and the TEXTOR-team, 30th EPS Conference on Contr. Fusion and Plasma Phys., St. Petersburg, 7-11 July 2003 ECA Vol. 27A, P-2.133

4. **“Safety factor profile evolution during the current ramp phase”**, A. Merkulov, G.M.D. Hogeweij, R.J.E. Jaspers, H.R. Koslowski, A. Krämer-Flecken, F.C. Schüller, E. Westerhof, Plasma Physics and Short Time-Scale Physics Springmeeting of DPG(Deutsche Physikalische Gesellschaft), 24 - 28 March 2003, Aachen

Bibliography

[1] Official ITER web page, www.iter.org

[2] Sauter O *et al* 2002 *Phys. Rev. Lett.* **88** 105001

[3] Mück A *et al* 2005 *Plasma Phys. Control. Fusion* **47** 1633

[4] Porcelli F *et al* 1996 *Plasma Phys. Control. Fusion* **38** 2163

[5] Westerhof E *et al* 2001 *Fusion Engineering and Design* **53** 259266

[6] Petty C C *et al* 2002 *Nuclear Fusion* **42** 1366-1375

Chapter 2

Theoretical Framework and Numerical Tools

2.1 Introduction

Numerical codes have become an irreplaceable tool, assisting scientists in understanding the experimental behaviour of plasma as well as predicting its evolution in various conditions. Recent technological leaps in the computer's development bring new possibilities for numerical calculations. With extra computational power it is possible to solve more difficult problems in multi-dimensional space, yet needing a reasonable amount of computational time. However, every numerical code is an implementation of one or another physical model which must be described and well understood before realisation.

This chapter discusses the theoretical framework of numerical codes used throughout this thesis. Section 2.2 introduces the ASTRA transport code and the basic underlying physics, which is implemented in the code. This code solves a system of 1D transport equations and is used to calculate the evolution of various plasma parameters such as electron temperature and density, and plasma equilibrium. Plasma parameters can be influenced by additional heating—which can be provided by different schemes, such as electron cyclotron resonance heating (ECRH), ion cyclotron resonance heating(ICRH), neutral beam injection (NBI) and lower hybrid (LH) resonance heating. Additional heating increases plasma temperature and therefore lowers plasma resistivity, which leads to a longer time of inductive operation. Also, the ECRH and the LH can assist in creating internal transport barriers which increases the confinement time. Finally, the generated non-inductive current drive can replace partly or fully the inductively driven ohmic current which results in a longer pulse time. The TEXTOR tokamak is equipped with a 140 GHz and 110 GHz gyrotrons for ECRH and two NBI injectors in co- and counter-directions. The power absorption and the amount of current drive cannot be calculated within the ASTRA code and require additional models to provide these parameters.

Section 2.3 describes the TORAY ray tracing code with a geometric optics (GO) approximation, which are used to calculate trajectories of radio frequency (RF) waves in the plasma. This code is very useful in preparing the experiments in order to estimate

the proper launching parameters of the ECRH. Section 2.4 discusses the TORBEAM beam tracing code based on another theoretical approach to calculate the propagation of RF waves in the plasma. In contrast to GO approximation, the beam tracing approach takes into account the wave properties, such as diffraction, of the injected beam, which play an important role for absorbtion calculations around the focal region. Section 2.5 outlines an extension of the ASTRA code which has been developed to calculate the NBI power deposition profile and generated current drive. Finally, Appendix 2.A presents sample calculations with the ASTRA code—optimising the properties of NBI current drive by varying parameters of the NBI facility at TEXTOR—and Appendix 2.B cover, using the TORAY codes, the operational limits for full absorption of the 140 GHz EC waves. Additionally, the Fokker-Planck code RELAX—which is used for the calculations of current drive—is described in Chapter 5.

2.2 The ASTRA transport code

2.2.1 Introduction

The ASTRA (Automatic System for TRansport Analysis) code [1] is more than a transport code in a conventional sense. It is a flexible programming system capable of creating numerical codes for predictive or interpretative transport modelling, for stability analysis and for processing experimental data. It is also not exclusively restricted to tokamak applications. The main features of the ASTRA system relevant to plasma experiments consist of

- an extensive library of modules describing different physical processes and data treatment;
- a graphical interface enabling transparent and user-friendly control during the calculations and for flexible data presentation;
- an interface to several experimental databases, so that experimental profiles can be taken directly from the database without a format conversion.

The physical quantities represented in the ASTRA code share the same implementation of data transformation routines, such as transition from the experimental grid to the internal grid of the code. This decreases the possibility of errors in any physical model derived with the ASTRA system and the modular organisation of the system allows easy composition of the required physical model.

Another significant feature of the system is the generation of interactive codes. The user can observe the time evolution of plasma parameters during program execution, interrupt it and change data presentation and control parameters thus influencing the course of the modelling. This enables the testing of different transport hypotheses at run time and so increases the efficiency of the modelling. The code can also run in background mode, which is useful for routine calculations, or for time consuming cases, e.g., when many additional heating schemes are involved. All output information is then saved and can be retrieved afterwards to study the time evolution of the

discharge. The ASTRA code is a constantly evolving tool and the latest documentation and improvements can be found on the home page of the code [2].

Within this thesis the ASTRA code has been primarily used in an interpretive mode, meaning that transport calculations were based on the experimental temperature and density profiles. Additional heating at the TEXTOR tokamak is provided by a 140 GHz ECRH and two neutral beam injectors. The NBI is modelled with a custom developed plug-in module which is discussed in detail in Section 2.5. The power deposition and non-inductive current drive generated by the ECRH are calculated by the TORBEAM beam tracing code (see Section 2.4). For this thesis the reconstruction of the plasma equilibrium and the current penetration are one of the main questions to be answered by these calculations. The plasma equilibrium is the base for topology used by ASTRA as described in the following sub-paragraphs.

2.2.2 Axisymmetric plasma equilibria

A tokamak is an axisymmetric system and, therefore, its equilibrium is independent of the toroidal angle ϕ and its magnetic field lines are conserved in nested toroidal magnetic surfaces. To achieve equilibruim the magnetic forces in the plasma must be balanced by plasma pressure

$$\vec{j} \times \vec{B} = \nabla p, \tag{2.1}$$

where $\vec{j}$ is the plasma current density, $\vec{B}$ is the magnetic field and p is the plasma pressure. It can be shown that $\vec{B} \cdot \nabla p = 0$ by taking the scalar product with $\vec{B}$ of both sides of this equation . Hence, magnetic surfaces are surfaces of constant pressure. In the same way the scalar product of the Equation (2.1) with $\vec{j}$ gives $\vec{j} \cdot \nabla p = 0$ and consequently the current lines also lie in the magnetic surfaces.

Let us define the axisymmetric coordinate system in the cylindrical form: R is the distance from the symmetry axis, z is the height above some arbitrary reference plane and ϕ is the toroidal angle (see Figure 2.1). Since we have an axisymmetric system it is convenient to introduce two arbitrary scalar functions Ψ and I which represent poloidal and current flux, respectively. The function Ψ is determined by the poloidal flux enclosed within each magnetic surface and is therefore a constant on that surface. The magnetic field can be expressed as a function of these two fluxes

$$\vec{B} = I\vec{\nabla}\phi + \vec{\nabla}\phi \times \vec{\nabla}\Psi. \tag{2.2}$$

This representation guarantees that $\vec{B}$ is divergence free since $\nabla I \cdot \nabla \phi = 0$. Substituting Equation (2.2) into Ampere's law,

$$\vec{j} = \frac{1}{\mu_0} \nabla \times \vec{B}, \tag{2.3}$$

we obtain

$$\mu_0 \vec{j} = \vec{\nabla} I \times \vec{\nabla}\phi - \vec{\nabla}\ \phi \triangle^* \Psi, \tag{2.4}$$

where

$$\triangle^* \Psi \equiv R^2 \vec{\nabla} \cdot \frac{\vec{\nabla}\Psi}{R^2} = \frac{\partial^2 \Psi}{\partial R^2} - \frac{1}{R}\frac{\partial \Psi}{\partial R} + \frac{\partial^2 \Psi}{\partial Z^2} \tag{2.5}$$

is known as the magnetic differential operator. Finally, combining Equation (2.4) with the pressure balance Equation (2.1) one can obtain

$$\triangle^* \Psi = -I(\Psi)\frac{dI(\Psi)}{d\Psi} - \mu_0 R^2 \frac{dp(\Psi)}{d\Psi}. \tag{2.6}$$

This equation is referred to as the Grad-Shafranov equation and describes the plasma equilibrium in terms of the flux function Ψ.

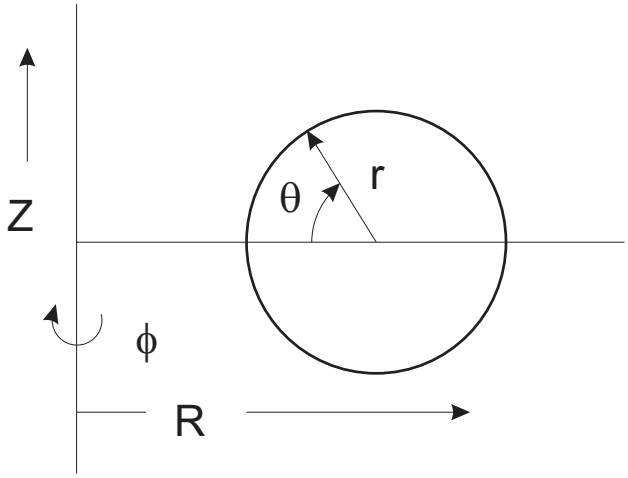

Figure 2.1: Axisymmetric coordinate system.

A large number of analytical results are obtained using the large-aspect ratio approximation for plasmas with circular cross-section. The main assumption being that all quantities are expanded in terms of the inverse aspect-ratio

$$\varepsilon = \frac{a}{R_0} \ll 1, \tag{2.7}$$

where a is the minor radius and R_0 is the major radius of the tokamak. It can be shown that the solution of the Grad-Shafranov Equation (2.6) for this approximation is represented by concentric circular flux surfaces and each of them is displaced by the distance $\Delta(r)$ with respect to the centre of the plasma (see Figure 2.2). The displacement on-axis $\Delta_S = \Delta(0)$ is called the Shafranov shift. The large-aspect ratio approximation works particularly well for the TEXTOR tokamak, since it has a circular cross section and $a/R_0 \approx 0.26$. For TEXTOR conditions, the shift as a function of minor radius can be approximated by a parabolic profile

$$\Delta(r) = \Delta_S \left(1 - \left(\frac{r}{a}\right)^2\right). \tag{2.8}$$

For a large-aspect ratio the Shafranov shift can be found from the following equation [6]:

$$\left(\frac{d\Delta}{dr}\right)_a = -\frac{a}{R_0}\left(\beta_p + \frac{l_i}{2}\right), \tag{2.9}$$

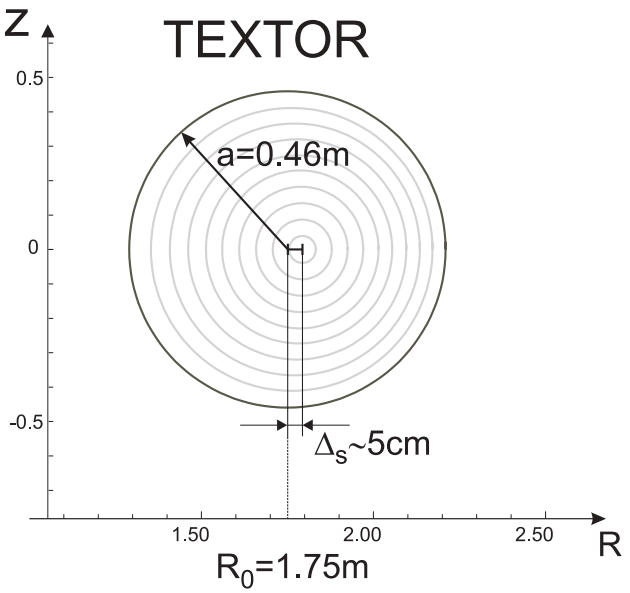

Figure 2.2: Equilibrium flux surfaces as calculated by the ASTRA code for the typical TEXTOR plasma discharge. The displacement Δ_S shows the Shafranov shift.

where β_p is the poloidal pressure and l_i is the internal inductance of the plasma. The poloidal pressure is given by

$$\beta_p = \frac{4\mu_0 \int_0^a p(r) r dr}{a^2 B_\theta^2(a)}, \tag{2.10}$$

where $p(r)$ is the pressure profile and $B_\theta(r)$ is the poloidal magnetic field. For a parabolic pressure profile, $p(r) = p_0\,(1-(r/a)^2)$, the poloidal pressure is $\beta_p = \mu_0 p_0 / B_\theta^2(a)$. The internal inductance of the plasma is defined as

$$l_i = \frac{2 \int_0^a B_\theta^2(r) r dr}{a^2 B_\theta(a)}, \tag{2.11}$$

and it reflects the shape of the plasma current profile. Higher values of l_i correspond to peaked current density, whereas lower values of l_i correspond to wider current density profiles. For example, parabolic profile for a current density, $j(r) = j_0(1-(r/a)^2)$, gives $l_i = 14/15$. Combining equations (2.8) and (2.9) we obtain an expression for the Shafranov shift

$$\Delta_S = \frac{1}{2}\frac{a^2}{R_0}\left(\beta_p + \frac{l_i}{2}\right). \tag{2.12}$$

This expression is used for the calculations of the Shafranov shift in the experiments in Chapter 4, where $l_i \approx 1$ is assumed and the poloidal beta is obtained from the diamagnetic measurements.

It is useful to note here that the described magnetic field topology has an effect on the kinetic velocity of the plasma particles. The magnetic field at the inboard side of the toroidal surface (small R) is larger than at the outboard side (large R). Particles moving along the field lines will therefore come from areas with low field to areas with

high field. Due to conservation of magnetic momentum the ratio of their kinetic velocity components perpendicular and parallel to the magnetic filed, $\upsilon_\perp/\upsilon_{||}$, will change as a function of their poloidal position. Particles with large $\upsilon_\perp/\upsilon_{||}$ at the low field side (LFS) will even reflect at a certain poloidal poloidal angle and are trapped bouncing at the LFS between the reflection points. This particle trapping has a pronounced effect on transport and current drive depending on the ratio between the collision frequency and the bounce frequency. In TEXTOR the collision frequency is for most of the plasma lower than the bounce frequency because of the high temperature and is therefore in the so-called 'banana regime'. The effect of trapping on current drive is taking care of in used Fokker-Planck codes.

2.2.3 Equilibrium solver in ASTRA

Two versions of the equilibrium solver are presently provided by the ASTRA system. The simpler version [11] solves the equilibrium Equation (2.6) using a 3-moment approach. It is assumed that the plasma configuration is up-down symmetric and each magnetic surface can be parameterised as

$$\begin{cases} R(\rho,\theta) = R_0 + \Delta(\rho) + \rho\left(\cos\theta - \delta(\rho)\sin^2\theta\right) \\ Z(\rho,\theta) = \rho\lambda(\rho)\sin\theta \end{cases}, \tag{2.13}$$

where ρ is the minor radius of every magnetic surface in the equatorial mid-plane, $\triangle(\rho)$ is the Shafranov shift, $\lambda(\rho)$ is the elongation and $\delta(\rho)$ is the triangularity of each flux surface. In this representation the boundary surface is specified by five parameters: R_0, ρ_B, $\triangle(\rho_B)$, $\lambda(\rho_B)$, $\delta(\rho_B)$. This is equivalent to a prescription of four characteristic points on the boundary surface. These are the two points in the mid-plane $\{R = R_0 + \triangle(\rho_B) \pm \rho_B, Z = 0\}$ and the two points most remote from the plane $\{R = R_0 + \triangle(\rho_B) - \rho_B\delta(\rho_B), Z = \pm\rho_B\lambda(\rho_B)\}$. TEXTOR has circular cross section, $\lambda(\rho) = 1$, $\delta(\rho) = 0$ and therefore the system of equations 2.13 is simplified to

$$\begin{cases} R(\rho,\theta) = R_0 + \Delta(\rho) + \rho\cos\theta \\ Z(\rho,\theta) = \rho\sin\theta \end{cases}, \tag{2.14}$$

which represent nested circles with each having a horizontal shift $\Delta(\rho)$. An example of the calculated equilibrium with the ASTRA code is shown in Figure 2.2.

2.2.4 Safety factor and magnetic shear

One of the important parameters describing a tokamak plasma is the safety factor, q, which is equal to the number of toroidal rotations of the magnetic field line after one poloidal revolution around the plasma. It plays an important role in describing the stability of the plasma. In the large aspect ratio approximation, the safety factor profile is given by

$$q(r) = \frac{rB_\phi}{R_0 B_\theta(r)}, \tag{2.15}$$

where r is the minor radius of the flux surface, B_ϕ is the toroidal magnetic field. Using Ampere's law, the q profile can be written as

$$q(r) = \frac{2\pi r^2 B_\phi}{\mu_0 I(r) R}, \tag{2.16}$$

where $I(r)$ is the toroidal plasma current inside the minor radius r. Local plasma instabilities are often connected with the presence of rational magnetic surfaces, which correspond to the rational values of q

$$q = \frac{m}{n}. \tag{2.17}$$

Here m is the integer number of toroidal and n is the integer number of poloidal turns around the plasma, after which a magnetic line is closed on itself. Irrational q values correspond to magnetic line which never closes and therefore ergodically cover the magnetic surface. One of the plasma instabilities—which appears in the plasma when a $q = 1$ surface is present—is a subject of this thesis and is described in more detail in Chapters 3 and 4.

A related quantity that turns out to be crucial for the occurrence of instabilities is the shear, s, in the magnetic field distribution. It is a measure for the change in direction of the field lines sa a function of radius:

$$s(r) \equiv \frac{r}{q(r)} \frac{dq(r)}{dr} \tag{2.18}$$

2.2.5 Transport equations

The transport equations are a set of equations which have to be solved in order to determine the radial profiles of density, electron and ion temperature, as functions of time. They contain transport coefficients which linearly relate the fluxes of particles, energy, and electric charge to the thermodynamic forces, such as the pressure, the electric field and temperature gradients for each charged particle species in the plasma. When these linear transport relations are combined with the conservation laws for particles and energy, and with Maxwell's equations they provide a closed set of equations—which predict the temporal evolution of the plasma from a properly chosen set of initial and boundary conditions.

The ASTRA code adopts the set of the transport equations derived in [11]. The basic set of transport equations in the ASTRA code includes equations for the electron density n_e, electron temperature T_e, ion temperature T_i and the poloidal flux ψ.

$$\begin{cases} \frac{1}{V'}\frac{\partial}{\partial t}(V' n_e) + \frac{1}{V'}\frac{\partial}{\partial \rho}\Gamma_e = S_e \\ \frac{3}{2}(V')^{-5/3}\frac{\partial}{\partial t}\left((V')^{5/3} n_e T_e\right) + \frac{1}{V'}\frac{\partial}{\partial \rho}\left(q_e + \frac{5}{2} T_e \Gamma_e\right) = P_e \\ \frac{3}{2}(V')^{-5/3}\frac{\partial}{\partial t}\left((V')^{5/3} n_i T_i\right) + \frac{1}{V'}\frac{\partial}{\partial \rho}\left(q_i + \frac{5}{2} T_i \Gamma_i\right) = P_i \\ \sigma_{||}\frac{\partial \psi}{\partial t} = \frac{R_0}{\mu_0 \rho}\frac{\partial}{\partial \rho}\left(G_2 \frac{\partial \psi}{\partial \rho}\right) - \frac{V'}{2\pi\rho}(j_{BS} + j_{CD}) \end{cases} \tag{2.19}$$

where $< f >= \frac{\partial}{\partial V}\int_V f dV$ denotes the flux surface average of the given function f, ρ is the effective minor radius, V is a volume integral inside the given flux surface,

$V' = \frac{\partial V}{\partial \rho}$, $G_2 \equiv \frac{V'}{4\pi^2}\left\langle\left(\frac{\nabla\rho}{r}\right)^2\right\rangle$, B_0 is the toroidal magnetic field, j_{BS} is the so-called bootstrap current density, j_{CD} is non inductive current density, $\sigma_{||}$ is the parallel plasma conductivity, P_e and P_i are the sources of electron and ion energy, Γ_e and Γ_i are electron and ion fluxes. The first equation follows from the particle conservation law, the next two represent the energy conservation laws and the last equation is a form of Faraday's law. To form a closed set of equation they are combined with the transport matrix, which relate fluxes to the thermodynamic forces

$$\begin{pmatrix} \frac{\Gamma_e}{n_e} \\ \frac{q_e}{n_e T_e} \\ \frac{q_i}{n_i T_i} \\ V' G_1 \frac{\mu_0 j_{BS}}{B_\theta} \end{pmatrix} = -V' G_1 \begin{pmatrix} D_n & D_e & D_i & D_E \\ \chi_n^e & \chi_e & \chi_i^e & \chi_E^e \\ \chi_n^i & \chi_e^i & \chi_i & \chi_E^i \\ C_n & C_e & C_i & 0 \end{pmatrix} \cdot \begin{pmatrix} \frac{1}{n_e}\frac{\partial n_e}{\partial \rho} \\ \frac{1}{T_e}\frac{\partial T_e}{\partial \rho} \\ \frac{1}{T_i}\frac{\partial T_i}{\partial \rho} \\ \frac{E_{||}}{B_p} \end{pmatrix} \tag{2.20}$$

where $G_1 \equiv \langle(\nabla\rho)^2\rangle$ and the diffusion coefficients in the second matrix can be given either as analytical functions derived from the kinetic theory or as experimental measurements. In practice it is rare to use the complete set of transport equations. For example, the electron density n_e or electron temperature T_e can often be replaced with the experimentally measured data. The flexibility of the ASTRA code allows to compute only quantities which are necessary for the current problem. The rest of the variables are simply ignored in this case, leading to the decrease in a computational time.

Chapters 4 and 6 include modelling of the current diffusion performed with the ASTRA code. In these chapters the ASTRA code was used in interpretive mode, which means that temperature and density profiles are supplied from the experiment. Therefore, only the last equation from the set of equations 2.19 was used. For the large aspect ratio and at low plasma pressure, ($V \approx 2\pi^2\rho^2 R_0$, $V' \approx 4\pi^2\rho R_0$), the current diffusion equation is given by

$$\sigma_{||}\frac{\partial \psi}{\partial t} = \frac{R_0}{\mu_0 \rho}\frac{\partial}{\partial \rho}\left(G_2 \frac{\partial \psi}{\partial \rho}\right) - 2\pi\rho R_0 (j_{\mathrm{BS}} + j_{\mathrm{CD}}). \tag{2.21}$$

Usually the plasma conductivity $\sigma_{||}$ is calculated assuming a thermal velocity distribution of electrons. The bootstrap current j_{BS} is caused by the effect of trapped particles and is driven by gradients in temperature and density and can be calculated from the transport matrix (2.20)

$$4\pi^2\rho G_1 \mu_0 \frac{j_{\mathrm{BS}}}{B_\theta} = C_n \frac{1}{n_e}\frac{\partial n_e}{\partial \rho} + C_e \frac{1}{T_e}\frac{\partial T_e}{\partial \rho} + C_i \frac{1}{T_i}\frac{\partial T_i}{\partial \rho} \tag{2.22}$$

where bootstrap coefficients C_n, C_e and C_i were equal to neoclassical Hirshman coefficients [24]. The non-inductive current drive j_{CD} is a sum of the NBI current drive, which is calculated by NBCD procedure (see Section 2.5.3), and EC current drive, which is calculated by the TORBEAM code (see Section 2.4). Finally, in Chapter 5 the assumption of a thermal plasma conductivity for the prediction of non-inductive current penetration is scrutinised by comparison of the ASTRA calculations with Fokker-Planck code calculations.

2.3 The TORAY ray tracing code

2.3.1 Introduction

A model for additional heating in the plasma is not part of the set of transport equations discussed in the previous Section 2.2. The additional heating contributes to the quantities P_e, P_i in the transport equations (2.19) as a source of electron and ion energy, respectively. Moreover, non-inductive current drive can be generated as a result of the interaction between the plasma and injected waves or particles, which is taken into account as j_{CD} in equations (2.19).

This section concentrates on the propagation of EC waves in the plasma and their numerical modelling with the TORAY [13] code—which incorporates the geometric optics approximation to describe the propagation of EC waves. Firstly, the propagation and accessibility of EC waves in the plasma are introduced. Then, the geometric optics approximation for the wave propagation in the plasma is discussed. Finally, the ray tracing equations as a central part of the TORAY code are outlined.

The TORAY code uses ray tracing equations to compute trajectories of EC waves in the plasma. Moreover, it calculates the absorbed power along the ray trajectory and generated current drive. However, the geometric optics approximation breaks down in several situations which can occur during the ECRH injection. One of them is a wrong description of the EC wave interaction with the plasma in the presence of strong wave focusing. The ECRH system of TEXTOR produces collimated beams with the focus in the centre of the plasma. Therefore, the calculations of the power deposition and the current drive for the TEXTOR experiments are performed with the TORBEAM beam tracing code, which is described in Section 2.4. The TORBEAM code implements another theoretical model for EC wave propagation, which takes into account diffraction effects. However, the TORAY code has an interface with the RELAX Fokker-Planck code (see Chapter 5)—to describe electron cyclotron current drive(ECCD) with a more detailed physics model on the basis of the calculated ray trajectories. The TORAY code supplies several quantities calculated along the ray trajectories to the RELAX code, such as coordinates of the crossed flux surfaces and the parallel refractive index.

The TORAY code supports several models for the plasma equilibrium to calculate the plasma density and the magnetic field along the ray trajectories. One of them is a simple circular cross section equilibrium and another one is based on the experimental profiles and is supplied by an external equilibrium solver. TORAY can hold up to 10 beams injected into the plasma and each of them can contain up to 1000 rays. The initial conditions such as launching position, wave power, frequency are set individually for every beam.

2.3.2 Electron Cyclotron Waves

EC waves injected into the plasma are generated with the gyrotron millimetre wave source. For example, the TEXTOR tokamak is equipped with 110 GHz and 140 GHz gyrotrons—the latter is capable of producing up to 800 kW of power in a continuous 10 s pulse. The injected EC waves interact directly only with the electrons and then

the absorbed energy is transmitted to the ions by electron-ion collisions. The interaction happens when the wave frequency, ω, is resonant with the electron cyclotron frequency, ω_{ce},

$$\omega = n\omega_{ce} = n\frac{eB}{\gamma m_e}, \tag{2.23}$$

where n is the harmonic number, γ is the relativistic mass increase and B is the magnetic field. The toroidal magnetic field in a tokamak is inversely proportional to the major radius and can be expressed in the midplane as

$$B(r) = \frac{B_0 R_0}{R_0 + r}, \tag{2.24}$$

where B_0 is a magnetic field in the centre of the tokamak, R_0 is a major radius and r is a minor radius coordinate. Due to this radial dependence of the toroidal magnetic field, the resonance area is localised in a narrow layer in the radial direction. Therefore, when EC waves, with high power density, are injected, the interaction with the electrons is limited within the intersection of the resonance layer and the wave beam. Such localisation of relatively high power makes possible the study of the local properties of the plasma and, moreover, provides opportunities for plasma control experiments.

To obtain the linear response of the homogeneous, quasi-neutral plasma to the injected EC waves, we describe the wave as a plane electromagnetic wave with the electric field

$$\vec{E}(\vec{r}, t) = \vec{E}\exp\left(i(\vec{k}\cdot\vec{r} - \omega t)\right) \tag{2.25}$$

and a similar expression for the magnetic field, $\vec{B}(\vec{r}, t)$. When this solution is substituted into the Maxwell's equations:

$$\nabla \times \vec{E} = -\frac{\partial \vec{B}}{\partial t}, \tag{2.26}$$

$$\nabla \times \vec{B} = \mu_0 \vec{j} + \frac{1}{c^2}\frac{\partial \vec{E}}{\partial t}, \tag{2.27}$$

and taking into account that in linear theory $\vec{j} = \hat{\sigma}\vec{E}$—where $\hat{\sigma}$ in the general case is the conductivity tensor of the plasma—the wave equation is obtained

$$\left(\vec{k}\vec{k} - k^2\hat{I} + \frac{\omega^2}{c^2}\hat{\varepsilon}\right)\cdot\vec{E} = 0, \tag{2.28}$$

where $\hat{I}$ is the identity tensor and $\hat{\varepsilon} = I + \frac{i}{\varepsilon_0}\hat{\sigma}\omega$ is the dielectric permittivity tensor. The left multiplier in Equation (2.28) is called the dispersion tensor, $\hat{\Lambda}$,

$$\hat{\Lambda} = \left(\vec{k}\vec{k} - k^2\hat{I} + \frac{\omega^2}{c^2}\hat{\varepsilon}\right). \tag{2.29}$$

Nontrivial solutions of Equation (2.28) exist when

$$D(\omega, \vec{k}) \equiv \det\hat{\Lambda} = 0, \tag{2.30}$$

where $D(\omega, \vec{k})$ defines the dispersion relation. For further discussion it is convenient to introduce the refractive index, $N = |\vec{N}|$, where

$$\vec{N} = \frac{\vec{k}c}{\omega} \tag{2.31}$$

and the parallel, $N_{||}$, and the perpendicular (to the magnetic field), $N_{\perp}$, refractive indices.

In the cold plasma approximation—which considers the limit that the thermal velocity $v_{ts} \to 0$—the dispersion relation 2.30 has two solutions which correspond to the O-mode and X-mode and is known as the Appleton-Hartree solution

$$N^2_{O,X} = 1 - \frac{\omega^2_{pe}}{\omega^2} \frac{2(\omega^2 - \omega^2_{pe})}{2(\omega^2 - \omega^2_{pe}) - \omega_{ce}(\sin^2\theta -, +\rho)}, \tag{2.32}$$

where

$$\rho^2 = \sin^4\theta + 4\cos^2\theta \frac{\omega^2 - \omega^2_{pe}}{\omega\omega_{ce}}, \tag{2.33}$$

where $\omega_{pe} = \frac{n_e e^2}{\varepsilon_0 m_e}$ is the plasma frequency. The O- and X-modes have different polarisations and dispersion relations. For perpendicular (to the magnetic field) propagation the O-mode has a wave electric field parallel to the magnetic field and therefore is linearly polarised. In contrast, for the same perpendicular injection the X-mode is elliptically polarised with $\vec{E} \perp \vec{B}$.

The analysis of the dispersion relation 2.32 for the refractive index indicates that the O-mode has a single cut-off frequency at $\omega = \omega_{pe}$ and the X-mode has two cut-off frequencies which for propagation perpendicular to the magnetic field can be written as

$$\omega_{\pm} = \pm\frac{\omega_{ce}}{2} + \left(\omega^2_{pe} + \frac{\omega^2_{ce}}{4}\right)^{1/2}. \tag{2.34}$$

The X-mode has two branches, namely, the fast branch with the cut-off frequency $\omega = \omega_+$ and the slow branch with the cut-off frequency ω_-. There is also a resonance for the X-mode at the upper hybrid frequency

$$\omega = \omega_{UH} = \left(\omega^2_{pe} + \omega^2_{ce}\right)^{1/2}. \tag{2.35}$$

Since the plasma frequency is a function of the electron density the existence of a cut-off frequency can limit the accessibility of the cyclotron resonance layer in the plasma. The O-mode has a single cut-off and therefore, for certain conditions, the central region of the plasma might not be accessible. For example, let us consider options for the TEXTOR toroidal magnetic field $B_t = 2.5$ T, which corresponds to $\omega_{ce}/2\pi = 70$ GHz. The 70 GHz fundamental harmonic O-mode has a density cut-off of $6 \cdot 10^{19}\mathrm{m}^{-3}$, which is an accessible density during TEXTOR operations. The 140 GHz second harmonic O-mode has poorer absorption and cannot be considered as an option. The 70 GHz fundamental X-mode experiences the density cut-off at ω_+ when launched from the low-field side. The high-field side launch is a technically difficult task. Therefore, the TEXTOR ECRH system operates at 140 GHz second harmonic

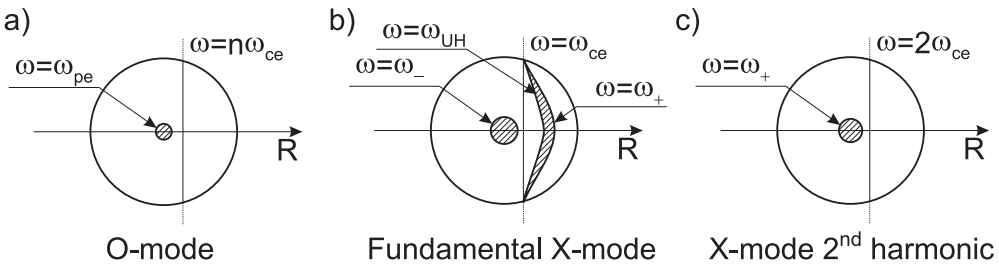

Figure 2.3: The shaded areas represent the inaccessible regions of the plasma due to the density cut-off for the a) O-mode b) fundamental X-mode. and c) 2nd and higher harmonics X-mode.

X-mode which has both good absorption and a high density cut-off of $12 \cdot 10^{19}\,\mathrm{m}^{-3}$. Figure 2.3 schematically shows the accessible regions of the plasma for different harmonics. More information on the theory of waves in the plasma can be found in the textbooks [3, 4, 5].

2.3.3 Ray tracing

To calculate the trajectory of the EC wave beam in the plasma the TORAY code [13] solves the ray tracing equations—which are obtained in the lowest order of Wentzel-Kramers-Brillouin (WKB) approximation. This approximation assumes that the wave properties have weak spatial and temporal dependencies, which can be expressed as two inequalities

$$L \gg \left|\frac{2\pi}{k}\right| \quad \text{and} \quad \tau \gg \left|\frac{2\pi}{\omega}\right|, \tag{2.36}$$

where L is a length scale and τ is a time scale on which wave properties change—$|2\pi/k|$ and $|2\pi/\omega|$ are the local wave length and the local oscillation period, respectively. Let us consider the local dispersion relation

$$D(\omega, \vec{r}, \vec{k}, t) = 0, \tag{2.37}$$

which has the unique solution ω for a wave with a given wave-vector, $\vec{k}$, located in a given point $(\vec{r}, t)$ in space and time:

$$\omega = \Omega(\vec{k}, \vec{r}, t). \tag{2.38}$$

It can be shown that with such constraints the solution for the wave propagation can be found from the ray equations

$$\frac{d\vec{r}}{dt} \equiv \vec{v}_{gr} = \frac{\partial\Omega}{\partial\vec{k}} = -\frac{\partial D/\partial\vec{k}}{\partial D/\partial\omega} \tag{2.39}$$

and

$$\frac{d\vec{k}}{dt} = -\frac{\partial\Omega}{\partial\vec{r}} = \frac{\partial D/\partial\vec{r}}{\partial D/\partial\omega}, \tag{2.40}$$

where $\vec{v}_{gr}$ is a group velocity. In the approximation of the time independent plasma equilibrium—which is a reasonable approximation considering the time an EC wave travels through the tokamak plasma—the ray equations can be rewritten with respect to the arc-length s as a parameter along the ray trajectory. That is

$$\frac{d\vec{r}}{ds} = -\mathrm{sgn}\left(\frac{\partial D}{\partial \omega}\right)\frac{\partial D/\partial \vec{k}}{|\partial D/\partial \vec{k}|} \tag{2.41}$$

and

$$\frac{d\vec{k}}{ds} = \mathrm{sgn}\left(\frac{\partial D}{\partial \omega}\right)\frac{\partial D/\partial \vec{r}}{|\partial D/\partial \vec{k}|}. \tag{2.42}$$

The TORAY code enables both possibilities to trace the ray in a time or arc-length dependent manner. The lowest order of the WKB expansion does not provide information about the energy absorption along the ray. To calculate the absorbed power the first order of the WKB approximation has to be calculated. However, the TORAY code implements the alternative way of the calculation of the power absorption, which is based on the on the calculation of the imaginary part of the perpendicular wave vector $k_{\perp}^{''}$. The absorbed power, dP_{abs}, along the arc element ds is calculated in the code as

$$dP_{\mathrm{abs}} = 2k_{\perp}^{''} ds_{\perp} P_{\mathrm{ray}} \tag{2.43}$$

where P_{ray} is the power of the ray, and $ds_{\perp}$ is the arc element projected along the direction of the perpendicular wave vector. This method is derived in the approximation of weak absorption—which is valid when $k^{''} \ll k^{'}$, where $k^{'}$ is the real part of the wave vector.

When waves with a finite $N_{||}$ are injected, the Doppler shift causes the cyclotron resonant absorption to preferentially heat electrons travelling in one direction. These heated electrons lose their momentum slower than other electrons and as a result a net current is generated. As it comes close or even crosses the trapped passing boundary, the cyclotron resonance can also induce electron trapping. The resulting effect of asymmetric trapping also leads to net current generation known as the Ohkawa current [7]. The TORAY code incorporates the model for current drive by Cohen [23], which includes relativistic, electron-ion collisions and trapped particles effects. The detailed description of the TORAY code and implemented features can be found in [13].

2.4 The TORBEAM beam tracing code

2.4.1 Introduction

The 140 GHz ECRH system at TEXTOR is tuned to produce focused beams with the focal point in the centre of the plasma. Therefore, it is important to use a beam tracing code like TORBEAM, which accounts for diffraction effects around the focal point, rather than the ray tracing approach—in order to calculate the absorbed power profile and the generated current drive in real plasma conditions.

One of the conditions that validates the geometric optics approximation is that the wave length of the EC wave, λ, is much smaller than the length scale of the plasma inhomogeneity, L,

$$\lambda \ll L \tag{2.44}$$

Normally this condition is well satisfied for the millimetre range of EC waves. However, while this condition is necessary, it is not sufficient for the applicability of geometric optics. The sufficient criterion, known as Fresnel condition, adds another length scale, namely, the wave beam width W, and can be written as

$$L\lambda < W^2 \tag{2.45}$$

If this condition is violated than the geometric optics approximation breaks down and wave behaviour such as diffraction starts to play a role. It is particularly important for focused EC wave beams in the vicinity of the focal point. The difference between the ray tracing approximation and the beam tracing technique (which will be discussed in the next section) is schematically shown in Figure 2.4. Around the focus the ray tracing algorithm gives a beam width converging to zero, which means that the beam power density approaches infinity. Please note that outside the focusing region the geometric optics approximation can be restored. There are several methods to solve the set of Maxwell's equations—which take advantage of the condition 2.44 without neglecting diffraction—such as a parabolic equation [16, 17] and a complex-eikonal [18, 19, 20] method. However, all these methods lead to a set of partial differential equations, which are more demanding in terms of computational algorithms then the set of ordinary differential equations (equations 2.41 and 2.42) of the geometric optics approximation.

On the other hand, the beam tracing approach—which is implemented in the TORBEAM [10] code—produces a set of ordinary differential equations(ODE). Therefore, the beam tracing approach can benefit from much less complicated numerical algorithms to solve the set of ODE. The beam tracing equations calculate the trajectory of the axis of the beam together with other characteristics of the beam, such as curvature of the phase front and the amplitude of the beam.

It was shown [19, 21] that in situations when the focal point of the injected beam is in the vicinity of the absorption layer, the geometric optics approximation predicts a very narrow power absorption profile—which is localised around the focus—with unrealistic values of the power density. On the contrary, the beam tracing approach gives the diffractive broadening of the beam around the focus and therefore prevents the extreme localisation of the absorbed power.

2.4.2 Beam tracing

The beam tracing(BT) equations employ the same approximation as the geometric optics, namely, the EC wave length, λ, is much smaller then the inhomogeneity scale of the plasma, L, and can be written as a condition for the parameter μ

$$\mu \equiv \frac{\omega L}{c} \gg 1, \tag{2.46}$$

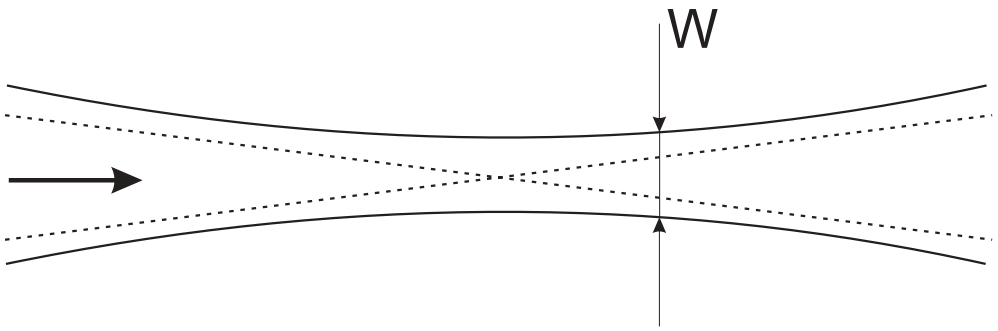

Figure 2.4: The schematic behaviour of the ray tracing (dotted lines) and the beam tracing (solid lines) approximations around the focal region of the wave. In the focal area the geometric optics approximations leads to the zero beam width W, and therefore infinite energy of the beam, whereas the beam approximation predicts a finite beam width.

where $\omega/2\pi$ is the wave frequency. In addition, the BT approach assumes another inequality, which is true for a typical experimental setup,

$$\lambda \ll W \ll L, \tag{2.47}$$

where W is a width of the injected beam. The solution for the electric field, $\vec{E}$, can be obtained from the wave equation, which is a combination of the two Maxwell's equations,

$$\frac{c^2}{\omega^2}\vec{\nabla} \times (\vec{\nabla} \times \vec{E}) - \hat{\varepsilon} \cdot \vec{E} = 0, \tag{2.48}$$

where $\hat{\varepsilon}$ is the dielectric tensor describing the plasma response. A solution is sought in the following form

$$\vec{E}(\vec{r}) = A(\vec{r})\vec{e}(\vec{r}) \exp\left\{i\mu\left(s(\vec{r}) + i\phi(\vec{r})\right)\right\}, \tag{2.49}$$

where $A(\vec{r})$ is the amplitude and $\vec{e}(\vec{r})$ is the unit vector responsible for the polarisation of the wave. The phase of the wave, $\bar{s} \equiv s(\vec{r}) + i\phi(\vec{r})$, has a real part, which has the same meaning as in the geometric optics approximation and an imaginary part, which contains the information on the transverse structure of the beam. The complex phase of the wave field—in the approximation of the Gaussian beam (meaning that the wave field of the beam has a Gaussian profile)—can be expanded around the beam axis

$$s(\vec{r}) = s_0(\vec{r}) + K_\alpha[x_\alpha - q_\alpha] + \frac{1}{2}s_{\alpha\beta}[x_\alpha - q_\alpha][x_\beta - q_\beta], \tag{2.50}$$

$$\phi(\vec{r}) = \frac{1}{2}\phi_{\alpha\beta}[x_\alpha - q_\alpha][x_\beta - q_\beta], \tag{2.51}$$

where $\alpha, \beta = 1, 2, 3$ and summation is performed over repeated indices. The variables q_α and K_α represent the position of the beam axis and the wave vector on it, respectively. The second order coefficients $s_{\alpha\beta}$ and $\phi_{\alpha\beta}$ are related to the curvature of the wave front and the width of the amplitude profile. These quantities $q_\alpha, K_\alpha, s_{\alpha\beta}$ and $\phi_{\alpha\beta}$ can be found as a solution of the following set of ordinary differential equations

$$\frac{dq_\alpha}{d\tau} = \frac{\partial H}{\partial k_\alpha}, \quad \frac{dK_\alpha}{d\tau} = -\frac{\partial H}{\partial x_\alpha}, \tag{2.52}$$

$$\frac{ds_{\alpha\beta}}{d\tau} = -\frac{\partial^2 H}{\partial x_\alpha \partial x_\beta} - \frac{\partial^2 H}{\partial x_\beta \partial k_\gamma} s_{\alpha\gamma} - \frac{\partial^2 H}{\partial x_\alpha \partial k_\gamma} s_{\beta\gamma} - \frac{\partial^2 H}{\partial k_\gamma \partial k_\delta} s_{\alpha\gamma} s_{\beta\delta} + \frac{\partial^2 H}{\partial k_\gamma \partial k_\delta} \phi_{\alpha\gamma} \phi_{\beta\delta}, \tag{2.53}$$

$$\frac{d\phi_{\alpha\beta}}{d\tau} = -\left(\frac{\partial^2 H}{\partial x_\alpha \partial k_\gamma} + \frac{\partial^2 H}{\partial k_\gamma \partial k_\delta} s_{\alpha\delta} \right) \phi_{\beta\gamma} - \left(\frac{\partial^2 H}{\partial x_\beta \partial k_\gamma} + \frac{\partial^2 H}{\partial k_\gamma \partial k_\delta} s_{\beta\delta} \right) \phi_{\alpha\gamma}, \tag{2.54}$$

where

$$H \equiv \det \left[(c/\omega)^2 (-k^2 \hat{I} + \vec{k}\vec{k}) + \hat{\varepsilon}_h \right] = 0 \tag{2.55}$$

is the dispersion function from the geometric optics approximation. It is seen that Equations (2.52) are similar to the ray tracing equations and describe the trajectory of the beam axis or the central ray. The derivatives of the H in formulas (2.52), (2.53) and (2.54) are to be taken on the central ray. The damping of the wave is calculated on the central ray and is given by

$$\frac{d|A|^2}{d\tau} = -\left(\vec{\nabla} \cdot \frac{\partial H}{\partial \vec{k}} + 2\vec{e}^* \cdot \hat{\varepsilon}_a \cdot \vec{e} \right) |A|^2. \tag{2.56}$$

Because the elements of the matrices $s_{\alpha\beta}$ and $\phi_{\alpha\beta}$ are not independent, the equations 2.52, 2.53 and 2.54 have to be completed with extra six constraints:

$$s_{\alpha\beta} \frac{\partial H}{\partial k_\beta} + \frac{\partial H}{\partial x_\alpha} = 0, \tag{2.57}$$

$$\phi_{\alpha\beta} \frac{\partial H}{\partial k_\beta} = 0. \tag{2.58}$$

Finally, the total number of equations to be solved is 19: 6 equations from the central ray (see Equation (2.52)) + 12 equations for the $s_{\alpha\beta}$ and $\phi_{\alpha\beta}$ quantities (see Equations (2.53) and (2.54)) + 1 equation for the wave amplitude (see Equation (2.56)). Please note, the total number of equations to be solved can be significantly smaller comparing with the ray tracing codes, where the number of equations to be solved is $7 \times n_r$ (n_r is a number of rays). Therefore, the beam tracing algorithm can be faster than the ray tracing one in the case of many individual rays.

Since the beam tracing approach is described by a set of ordinary differential equations, the main task of the TORBEAM code is to supply all coefficients—which appear in Equations (2.52), (2.53), (2.54) and (2.56)—to a standard Ordinary Differential Equations (ODE) solver. The current drive efficiency is calculated using the subroutine developed by Cohen [23], which takes into account effects of trapped particles. The comprehensive description of the beam tracing technique and a comparison with ray tracing calculations are given in [10, 21, 22].

2.5 NBI routines for the ASTRA transport code

2.5.1 Introduction

This Section covers several FORTRAN subroutines which calculate the NBI power deposition and driven current density profiles. These subroutines are implemented as plug-in modules for the ASTRA [1] transport code and have been used in many current diffusion calculations presented in this thesis.

2.5.2 Neutral beam power deposition subroutine

The neutral beam power deposition (NBPD) procedure calculates the NBI deposition profile on the basis of the injection geometry at the TEXTOR tokamak and plasma parameters. Firstly, the physical model behind the calculations is described. Secondly, the interface between the NBPD procedure and the ASTRA code is given.

Physics behind

The injected neutrals get ionised due to interaction with plasma and contribute to NBI current drive. Here we describe one of the methods how to calculate the power deposition profile, neglecting the drift of ions. Therefore, we assume that power absorbtion takes place together with the ionisation of neutrals. Neutral beam density attenuates along the beam line due to NB-plasma interaction and is given by

$$n(x,y,z) = n_0(x,y)e^{-\int_0^z n_e(x,y,z,)\sigma(x,y,z)dz} \equiv n_0(x,y)\xi(x,y,z), \tag{2.59}$$

where x, y, z form a coordinate system relative to the beam (see Figure 2.5), $\sigma(x,y,z)$ is the cross section of the interaction between neutral beam and the plasma, $n_e(x,y,z)$ is the electron density and $n_0(x,y)$ is the initial distribution of the density in the beam before entering the plasma.

To simplify the integration procedure along the beam coordinate z let us assume that every beam consists of a bunch of the parallel pencil beams. By definition the density distribution in every pencil beam is represented by a δ function. The choice of the computational grid does not affect the consequent computations in this section, though in the NBPD procedure the pencil beams are equally distributed over the beam footprint (see Figure 2.5). The total number of pencil beams affects the accuracy as well as computational time. Reasonable results are achieved with 15 horizontal and 20 vertical points resulting in a total of 300 pencil beams. The density in each pencil beam can be written as

$$n_{i,j}(z) = n_0(x_i,y_j)\xi(x_i,y_j,z)\delta(x-x_i,y-y_i), \tag{2.60}$$

where x_i and y_j are the coordinates of the pencil beam, and i, j are indexes of the pencil beam. The total beam density is the sum over all pencil beams

$$n(x,y,z) = \sum_{i,j} n_{i,j}(z). \tag{2.61}$$

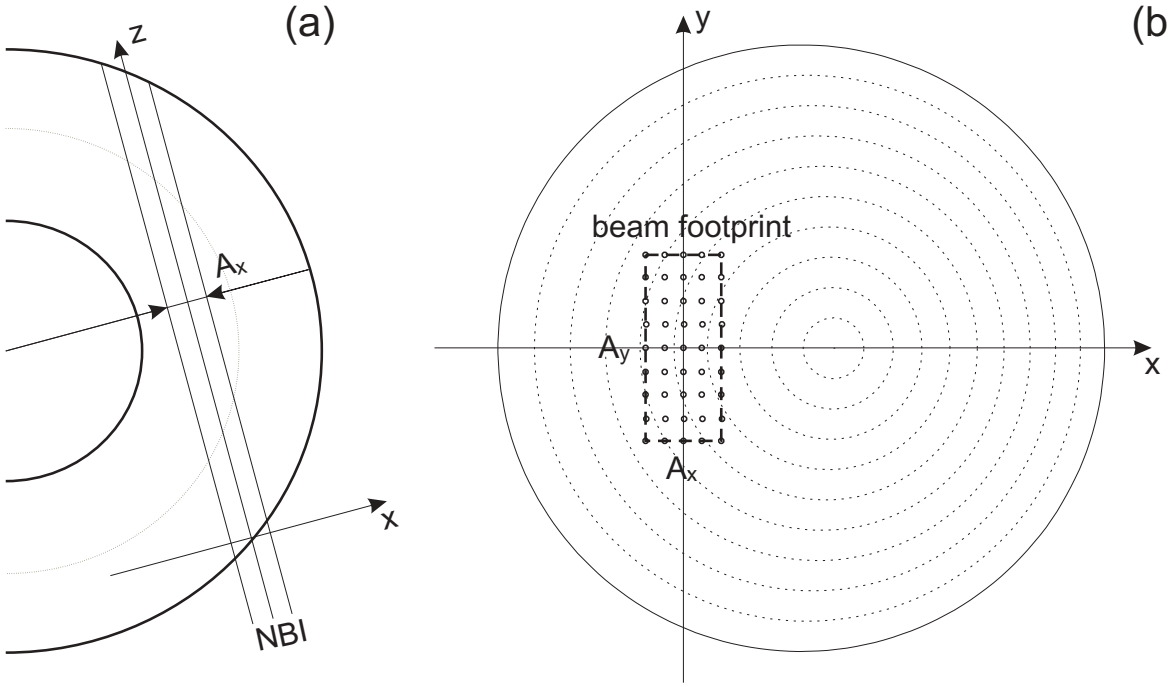

Figure 2.5: a) Toroidal cross section of the tokamak during NBI injection. The A_x is the beam width, A_y is the beam height, and x and z are coordinates relative to the beam line. b) Poloidal cross section perpendicular to the beam line. The dashed rectangle shows the beam footprint. Points inside the footprint schematically represent the computational grid.

We consider that the neutral beam has a two-dimensional Gaussian distribution of the density when entering the plasma

$$n(x,y,0) = e^{-\left(\frac{x}{W_x}\right)^2-\left(\frac{y}{W_y}\right)^2}, \tag{2.62}$$

where W_x and W_y are Gaussian widths. The power of the beam at any point is proportional to the integral of the density $P(z) \sim \int\int n(x,y,z)dxdy$, therefore the ratio between the total injected power P_0 and the power at the position z can be written as

$$\frac{P(z)}{P_0} = \frac{\sum_{i,j} n_0(x_i,y_j)\xi(x_i,y_j,z)}{\sum_{i,j} n_0(x_i,y_j)}. \tag{2.63}$$

The absorbed power, P_{abs}, as a function of z is given by

$$P_{\text{abs}}(z) = P_0 - P(z) = P_0\frac{\sum_{i,j} n_0(x_i,y_j)\left(1-\xi(x_i,y_j,z)\right)}{\sum_{i,j} n_0(x_i,y_j)}. \tag{2.64}$$

The absorbed power as a function of the z coordinate is transformed than to the power deposition profile, $P_{\text{dep}}(r)$, as a function of minor radius. The coordinates of flux surfaces are taken directly from ASTRA variables, ensuring the correct transformation at each time step.

Usage from ASTRA

The interface between the ASTRA code and the NBPD procedure is provided by the subroutine $/sbr/nbpd.f$. This subroutine incorporates all the physics discussed in the previous section and can be modified by the user. Table 2.1 contains a list of input and output parameters for the NBPD procedure.

Parameter	Units	Type	Description
TTE[in]	keV	ASTRA Array	Electron temperature
DDE[in]	$10^{19}\mathrm{m}^{-3}$	ASTRA Array	Electron density
POWER[in]	MW	Real	Total injected beam power
EBEAM[in]	keV	Real	Energy of the beam
MBEAM[in]	AMU	Real	Mass of the beam ions
CBEAM[in]		Real	Beam charge
VTARGET[in]	m	Real	The size of the V-target
PNBI[out]	$\mathrm{MW/m}^3$	ASTRA Array	NBI power deposition profile
APOWER[out]	MW	Real	Total absorbed power

Table 2.1: The input and output parameters for the NBPD subroutine. The V-target is a device in the TEXTOR NBI-system to truncate the beam width.

2.5.3 Neutral beam current drive subroutine

The neutral beam current drive (NBCD) procedure calculates the NBI current drive efficiency on the basis of the NBI power deposition profile and plasma parameters. Firstly, the physical model behind the calculations is described. Secondly, the interface between the NBCD procedure and ASTRA code is given.

Physics behind

This section closely follows the discussion from section 3.14, 'Current Drive'[6]. Neutral beam injection produces a current of fast ions circulating around the torus. The slowing down of these fast ions by collisions with electrons causes the electrons to drift toroidally in the same direction as the fast ions. The electron current due to this drift is in the reverse direction to the fast ion current, so there is some cancellation between these two components. The degree of cancellation depends on the charge, Z_f, of the fast beam ions, the effective plasma ion charge, Z_eff, and the number of trapped electrons. In the usual regime, where the electron thermal velocity significantly exceeds the fast ion velocity, use of the Fokker-Planck equation to calculate the beam driven current in the large aspect-ratio approximation and in the low collisionality banana regime gives,

$$I = I_f \left(1 - \frac{Z_\mathrm{f}}{Z_\mathrm{eff}} + 1.46\sqrt{\varepsilon}\frac{Z_\mathrm{f}}{Z_\mathrm{eff}} A(Z_\mathrm{eff})\right) \tag{2.65}$$

where I is the net driven current, I_f is the fast ion current and $\varepsilon = r/R$ is the inverse aspect ratio. For fast ion velocities which are much less than the electron thermal velocity, as is normally the case, values of the function A range from 1.67 for $Z_{\text{eff}} = 1$, to 1.18 for $Z_{\text{eff}} = 4$. For the calculations of TEXTOR discharges the value of the function A is set to 1.5. In Equation (2.65) the second term on the right hand side represents the reverse electron current in the absence of trapped electrons and the third term takes their effect into account. The fast ion current density can also be written in terms of the fast ion source rate per unit volume, S,

$$j_f = S\tau_{cx} e Z_{\text{f}} \upsilon_{||} \tag{2.66}$$

The radial profile of the beam deposition is calculated by the NBPD procedure(see Section 2.5.2), which takes into account the injection geometry.

Furthermore, to compute the local fast ion current density, j_f, a two-dimensional Fokker-Planck or Monte Carlo calculation of the beam ion velocity distribution is generally necessary, including the effects of trapping of the fast ions. In the absence of trapping, a relatively simple analytic solution can be found and the current density is given by,

$$j_f = \frac{S\tau_s e Z_{\text{f}} \upsilon_0}{(1+u_c^2)} \int_0^1 f_1(u) u^3 du, \tag{2.67}$$

where τ_s is the fast ion slowing down time and u is the fast ion velocity normalised to the injection velocity, υ_0. The ion-electron slowing down time is taken from [9]

$$\tau_s^{-1} = 1.6 \times 10^{-9} \frac{n_e Z_{\text{f}}^2 \lambda_{ie}}{m_f T^{-3/2}}, \tag{2.68}$$

where λ_{ie} is a Coulomb logarithm $\lambda_{ie} = 23 - ln\left(n_e^{1/2} T_e^{-3/2}\right)$. The distribution function f_1 is the first order Legendre polynomial component of f given by

$$f_1 = u^{2\beta} \left[\frac{1+u_c^3}{u^3+u_c^3}\right]^{(1+2\beta/3)}, \tag{2.69}$$

where

$$\beta = \frac{m_i Z_{\text{eff}}}{2 m_f \bar{Z}}, \tag{2.70}$$

$$u_c^3 = \frac{3\sqrt{\pi}}{4} \frac{m_e \bar{Z} \upsilon_{Te}^3}{m_i \upsilon_0^3}, \tag{2.71}$$

and

$$\bar{Z} = \sum_i \frac{m_f n_i Z_i^2}{m_i n_e}, \tag{2.72}$$

the subscript i refers to the plasma ions.

Finally, the fast ion source rate, S, can be expressed through the deposited NBI power per unit volume $P_d = \frac{1}{2} m_f \upsilon_0^2 S$, which gives

$$j_f = P_d \frac{2\tau_s e Z_{\text{f}}}{m_f \upsilon_0 (1+u_c^2)} \int_0^1 f_1(u) u^3 du. \tag{2.73}$$

The deposited neutral beam power, P_{dep}, is calculated by the NBPD procedure (see Section 2.5.2) and takes into account the injection geometry.

Interface with ASTRA

The interface between the ASTRA code and the NBCD procedure is provided by the subroutine $/sbr/nbcd.f$. This subroutine incorporates all the physics discussed in the previous section and can be modified by the user. Table 2.2 contains a list of input and output parameters for the NBCD procedure.

Parameter	Units	Type	Description
TIME[in]	s	Real	Current time of the simulation
START[in]	s	Real	Start time of the NBI injection
ABEAM[in]	amu	Real	Mass of the beam's ions
EBEAM[in]	keV	Real	Energy of the beam
TRAPPING[in]		Integer	[1,0] - [on/off] trapping effects
TTE[in]	keV	ASTRA Array	Electron temperature
DDE[in]	$10^{19}\mathrm{m}^{-3}$	ASTRA Array	Electron density
PNBI[in]	$\mathrm{MW/m}^3$	ASTRA Array	NBI power deposition profile
JNBI[out]	$\mathrm{MA/m}^3$	ASTRA Array	Generated driven current density

Table 2.2: The input and output parameters for the NBCD subroutine.

2.5.4 NBCD3 subroutine

The neutral beam at the TEXTOR tokamak contains three different beam fractions with full beam energy, half and one third of the total beam energy. Therefore, to calculate the current drive efficiency at TEXTOR the NBCD and NBPD subroutines have to be called three times with different values of the beam energy. The subroutine NBCD3 has been introduced to simplify calculations and allows to have only one subroutine call. Table 2.3 shows the input and output parameters for the NBCD3 subroutine. It has almost identical set of parameters as the NBCD and NBPD procedures excepting extra three arguments which specify the distribution of the energy fractions in the beam.

Appendices

2.A Optimisation of the neutral beam current drive by varying V-target

The neutral beam injection system at the TEXTOR tokamak is equipped with a graphite V-target that defines the aperture of the beam and, thereby, limits the injected power [8].

Parameter	Units	Type	Description
TIME[in]	s	Real	Current time of the simulation
START[in]	s	Real	Start time of the NBI injection
TTE[in]	keV	ASTRA Array	Electron temperature
DDE[in]	10^{19}m^{-3}	ASTRA Array	Electron density
POWER[in]	MW	Real	Total injected beam power
FR1[in]		Real	Beam fraction with the full energy
FR2[in]		Real	Beam fraction with 1/2 of the energy
FR3[in]		Real	Beam fraction with 1/3 of the energy
EBEAM[in]	keV	Real	Energy of the beam
MBEAM[in]	AMU	Real	Mass of the beam ions
CBEAM[in]		Real	Beam charge
VTARGET[in]	m	Real	The size of the V-target
ABEAM[in]	amu	Real	Mass of the beam's ions
TRAPPING[in]		Integer	[1,0] - [on/off] trapping effects
PNBI[out]	MW/m^3	ASTRA Array	NBI power deposition profile
JNBI[out]	MA/m^3	ASTRA Array	Generated driven current density
APOWER[out]	MW	Real	Total absorbed power

Table 2.3: The input and output parameters for the NBCD3 subroutine.

Another effect of the variable V-target is the increase/decrease of the Gaussian width of the neutral beam density profile at the entrance to the plasma. Hence, by decreasing the V-target, the power deposition profile and, consequently, NBI driven current density profile become more localised. With a more narrow non-inductive current drive it is easier to affect the evolution of the safety factor profile, q. In this section predictions of the current penetration during the plasma current ramp-up with various sizes of the V-target are presented.

The discharge #89937 with central ECRH has been chosen as a basis for transport calculations in this section. This discharge has 1MW of NBI power during the current ramp-up phase and a fully open V-target, which gives the height of the beam of 50 cm. In the experiment, a fast initial ramp (first 100 ms) up to I_p = 200 kA is followed by a slower ramp up to 350 kA at t = 600 ms. Central ECRH (270 kW, t = 250 - 450 ms) is applied for additional electron heating. To study the possibility to tailor the current density profile by NBCD under these plasma conditions, the size of the V-target has been varied from 0.1 m to 0.5 m in a series of calculations with NBCD module (see 2.5.3). The calculated NB driven current density is plotted in Figure 2.6. As expected the smallest V-target produces the narrowest current density profile. However, because the produced profile with 0.1 m V-target is more peaked, also the total NB driven current is decreased. The total NB current drive as a function of time is shown in Figure 2.7 for different sizes of the V-target.

The ASTRA code [1] has been used to perform current diffusion calculations, which consider neoclassical transport coefficients and experimental electron density and temperature profiles. The Figure 2.8 shows the evolution of the minimal value of the

safety factor for different sizes of the V-target. Even the most peaked non-inductive current density, which corresponds to the 0.1 m V-target, could not significantly affect the current penetration. This can be explained by the difference in the total driven current by a factor of two for the fully open, 0.5 m, and almost closed, 0.1 m, V-target. In conclusion, the V-target can be used to tailor the non-inductive current density profile. However, due to the decrease in the generated driven current with the closing of the V-target, the effect on the current penetration becomes insignificant.

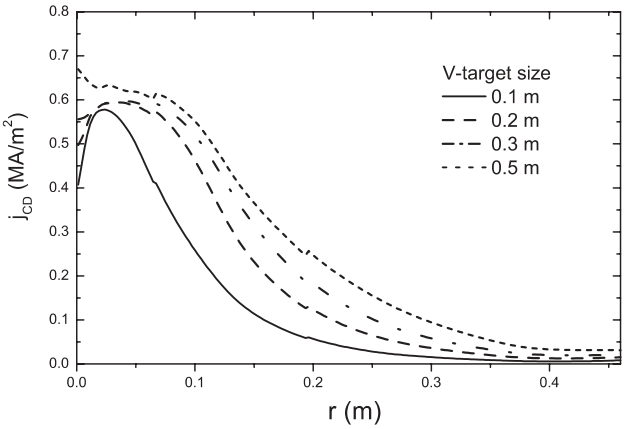

Figure 2.6: The non-inductive NB driven current density as a function of minor radius for different sizes of the V-target. Calculations are performed on the basis of the experimental data for 89937 discharge at t=600 ms.

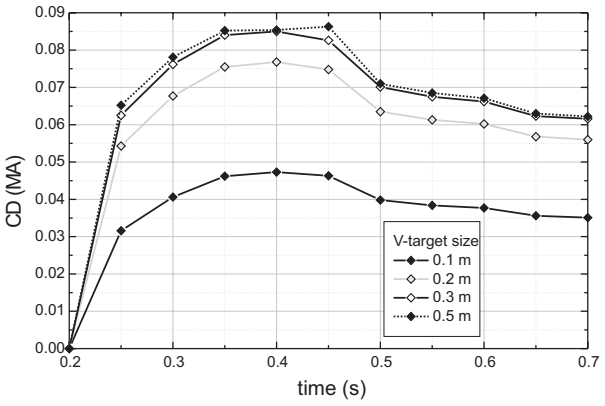

Figure 2.7: The evolution of the NBI current drive for different sizes of the V-target. Calculations are performed on the basis of the experimental data for 89937 discharge.

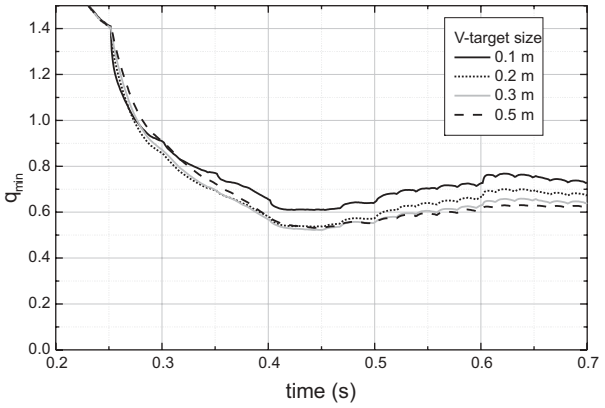

Figure 2.8: The evolution of the minimal value of the q profile for different sizes of the V-target. Calculations are performed on the basis of the experimental data for 89937 discharge.

2.B Absorption calculations of the 140GHz EC waves in TEXTOR

In 2002 the 140 GHz gyrotron—which was one of the major contributions of the FOM team in the framework of Trilateral Euregio Cluster(TEC) agreement—replaced the previous 110 GHz ECRH system. The gyrotron is capable of delivering up to 800 kW in a continuous pulse up to 3 s. The gyrotron operates in X-mode and normally only the 2^{nd} harmonic is present in the plasma. However, the 3^{rd} harmonic might appear in the plasma at the low field side if the toroidal magnetic field is too low. The TORAY ray tracing code was used to calculate the absorption of the 140 GHz EC waves for some TEXTOR plasma conditions. The waves are injected perpendicular to the magnetic field in the midplane of the tokamak.

The electron temperature profile is taken to be a simple profile

$$T_{\text{e}}(r) = (T_{\text{e}_{\text{max}}} - T_{\text{e}_{\text{min}}}) \left(1 - \left(\frac{r}{a}\right)^2\right)^3 + T_{\text{e}_{\text{min}}} \tag{2.74}$$

where the central temperature $T_{\text{e}_{\text{max}}} = 2.0\,\text{keV}$ and the edge temperature $T_{\text{e}_{\text{min}}} = 0.16\,\text{keV}$. The electron density profile has been also chosen in a parabolic shape and is given by

$$n_{\text{e}}(r) = (n_{\text{e}_{\text{max}}} - n_{\text{e}_{\text{min}}}) \left(1 - \left(\frac{r}{a}\right)^2\right)^{1.2} + n_{\text{e}_{\text{min}}} \tag{2.75}$$

where the electron central density $n_{\text{e}_{\text{max}}} = 6 \cdot 10^{19}\text{m}^{-3}$ and the electron edge density $n_{\text{e}_{\text{min}}} = 0.06 \cdot 10^{19}\text{m}^{-3}$. A circular plasma equilibrium was considered with a safety factor in the centre $q_0 = 1$ and at the edge $q_a = 4$. Figure 2.9 shows the absorbed power normalised to injected EC power as a function of the toroidal magnetic field. The toroidal magnetic field for usual TEXTOR operations varies between 2 T and 2.5 T, hence, the second harmonic is fully absorbed in plasma and the third harmonic does not enter the plasma. However, for the magnetic field below 2 T, where the 2^{nd} harmonic is partially absorbed, it is possible that the 3^{rd} harmonic enters the plasma. Figure 2.10 plots the absorbed power normalised to the injected EC power as a function of the minor radius. It is seen that for the toroidal magnetic field below 2 T the 2^{nd} and 3^{rd} harmonics can be present simultaneously in the plasma at the high and low field sides, respectively.

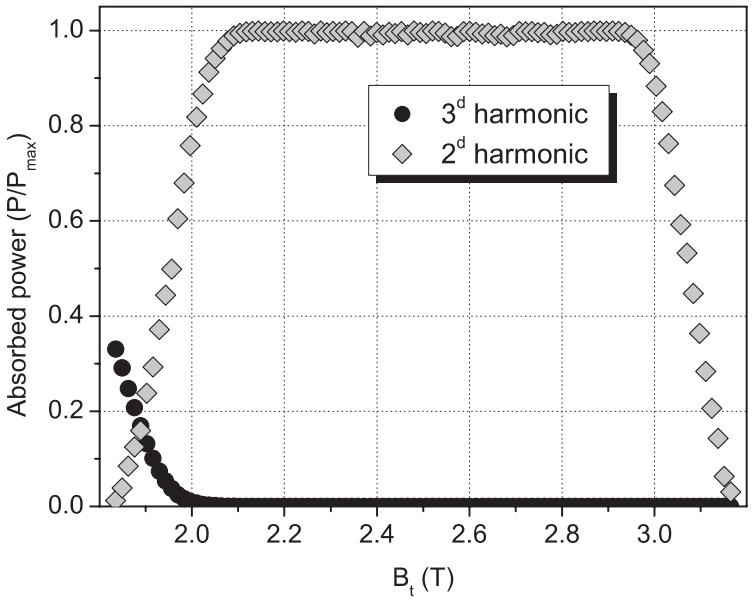

Figure 2.9: The absorbed power normalised to the injected EC power as a function of the toroidal magnetic field.

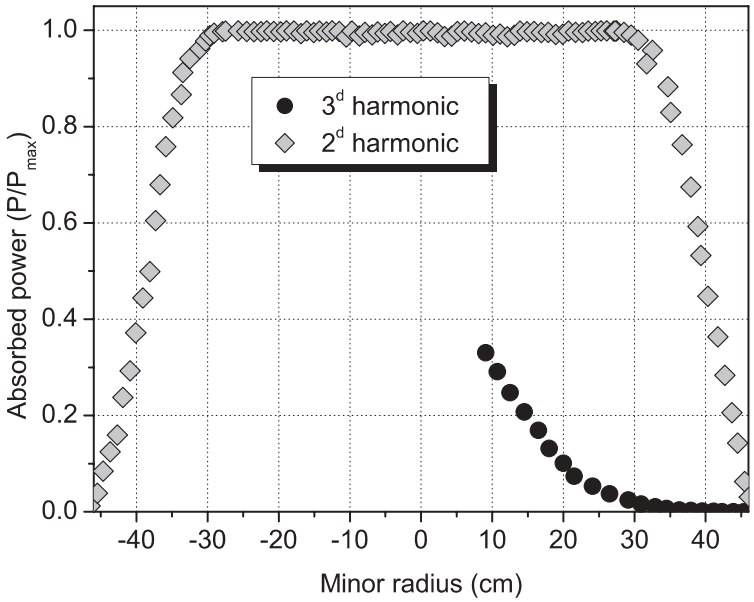

Figure 2.10: The absorbed power normalised to the injected EC power as a function of the minor radius.

Bibliography

[1] Pereverzev G *et al* August 1991 *ASTRA, Report IPP 542*

[2] ASTRA manual, *http://www.ipp.mpg.de/~git/astra/*

[3] Stix T H *The theory of plasma waves*, AIP, New York, 1992

[4] Swanson D G *Waves in plasmas*, Academic Press, San Diego, 1989

[5] Cairns R A *Radiofrequency heating of plasmas*, IOP Publishing, Bristol, 1991

[6] Wesson J *Tokamaks*, Clarendon Press, Oxford, 2004, p 122

[7] Ohkawa T 1946 *General Atomic Report*, 4356.007.001

[8] Uhlemann R *et al* 1999 *Fusion Technology* **35** 42

[9] NRL Plasma Formulary, http://wwwppd.nrl.navy.mil/nrlformulary/

[10] Poli E *et al* 2001 *Computer Physics Communication* **136** 90

[11] Hinton F L *et al* 1978 *Reviews of Modern Physics* **48** 239

[12] Zakharov L E *et al* 1999 *Phys. Plasmas* **6** 4693

[13] Westerhof E 1989 *Implementation of Toray at JET*, Rijnhuizen Report **RR-89-183**

[14] Bernstein I B 1975 *Phys. Fluids* **18** 320

[15] Bornatici M *et al* 1983 *Nuclear Fusion* **23** 1153

[16] Aamodt R E 1994 *Phys. Plasmas* **1** 6

[17] Phillips C K *et al* 1986 *Phys. Fluids* **29** 1608

[18] Mazzucato E 1989 *Phys. Fluids B* **1** 1855

[19] Nowak S *et al* 1993 *Phys. Fluids B* **5** 1945

[20] Peeters A G 1996 *Phys. Plasmas* **3** 4386

[21] Poli E 2001 *Fusion Engineering and Design* **53** 9

[22] Pereverzev G V 1998 *Phys. Plasmas* **5** 3529

[23] Cohen R H 1987 *Phys. Fluids* **30** 2442

[24] Hirshman S P 1988 *Phys. Fluids* **31** 3150

Chapter 3

Theory of the sawtooth instability

3.1 Introduction

This chapter discusses the well known core plasma instability, which first was discovered in 1974 [1], known as the sawtooth instability—which is a relaxation oscillation of temperature and density [6]. This instability appears as a sawtooth oscillation on many different diagnostics surveying the plasma core. For example, Figure 3.1 shows the raw data from the central and the outer channels of the electron cyclotron emission (ECE) diagnostic, the signal of which is proportional to the electron temperature. The temperature variation in the outer region has an inverted behaviour compared to the centre of the plasma. During the ramp phase it is clear that the central temperature rises and, at the collapse, the associated thermal energy is released to the outer part of the plasma in the form of a heat pulse. The sawtooth instability and Kadomtsev's reconnection model [2] are introduced in Section 3.2. The Kadomtsev's model describes the sawtooth crash phase and the process of the magnetic reconnection which takes place during the crash. The stability criterion and the growth rate of the unstable mode in the framework of Porcelli's model [5] are discussed in Section 3.3. Porcelli's model describes the full sawtooth cycle and allows to make theoretical predictions of the sawtooth period. Finally, the application of Porcelli's model to the typical plasma conditions in the TEXTOR tokamak is presented in Section 3.4.

3.2 Sawtooth instability and Kadomtsev's reconnection model

The sawtooth collapse is driven by an instability which has an $m = 1$, $n = 1$ structure and usually starts when the safety factor profile on axis (see Section 2.2.4), $q(r)$, drops below unity. The q profile also oscillates in a sawtooth-like manner, that is, the q value on-axis falls during the ramp phase and rises at the collapse. The collapse phase is much shorter than the characteristic resistive time $\tau_R = \mu_0 r_1^2/\eta$, where r_1 is the radius of the $q = 1$ surface and η is the plasma resistivity. The resistive time is typically of the order of $\sim 10\,\text{ms}$ in TEXTOR, whereas the collapse phase could last $\sim 100\,\mu\text{s}$. A model with a fast magnetic reconnection was proposed by Kadomtsev [2] to explain the rapidity of the magnetic rearrangement during the collapse.

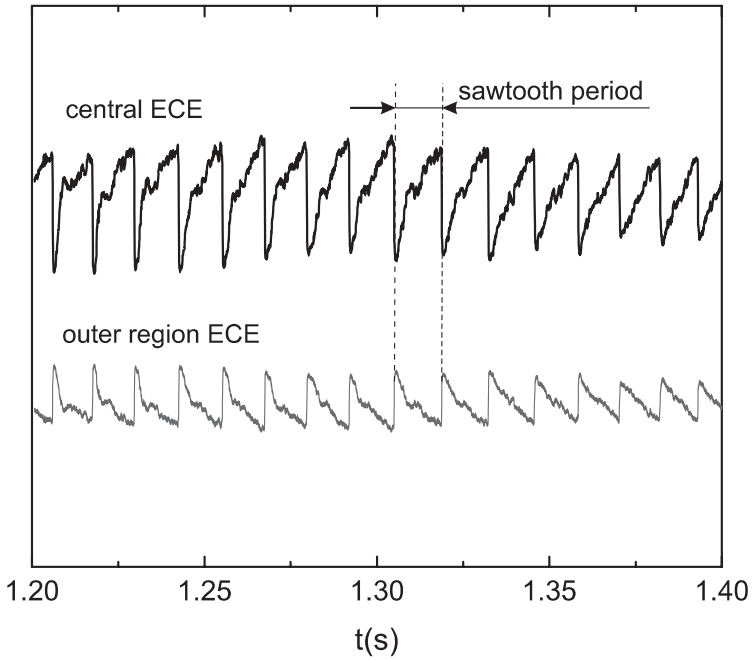

Figure 3.1: The raw signal from the central and the outer ECE channels during sawtooth oscillations.

The reconnection process, according to Kadomtsev, is concerned with the magnetic flux perpendicular to the helix, which is defined by the magnetic field lines on the $q = 1$ surface. The helical magnetic field B_h for the large aspect ratio approximation [3], $a/R << 1$, is

$$B_h = B_\theta - (r/R)B_\phi = B_\theta(1 - q), \tag{3.1}$$

where B_θ and B_ϕ are the poloidal and the toroidal magnetic fields, respectively, and the safety factor profile, $q(r) = rB_\phi/RB_\theta$. The corresponding helical flux is given by

$$\frac{d\psi_h}{dr} = B_h. \tag{3.2}$$

The helical magnetic field changes sign at the $q = 1$ surface and in Kadomtsev's model the helical flux between the magnetic axis and the $q = 1$ surface reconnects with an equal and opposite flux outside the $q = 1$ surface. The reconnection process is shown schematically in Figure 3.2 as a sequence of states of the magnetic structure. The reconnected flux forms an island (green lines in Figure 3.2) which grows and ultimately displaces the original core of the plasma (red lines in Figure 3.2). From Kadomtsev's model the characteristic time of the collapse is given by [3]

$$\tau_C \sim (\tau_R \tau_A)^{1/2}, \tag{3.3}$$

where $\tau_A = r_1\sqrt{\mu_0 n_i m_i}/B_h$ is an Alfvén time. Since $\tau_A \ll \tau_R$ Kadomtsev's model predicts the collapse time which is much closer to the experimental values than the resistive time. However, a discrepancy of one order of magnitude remains for hot tokamaks, such as JET, JT-60U.

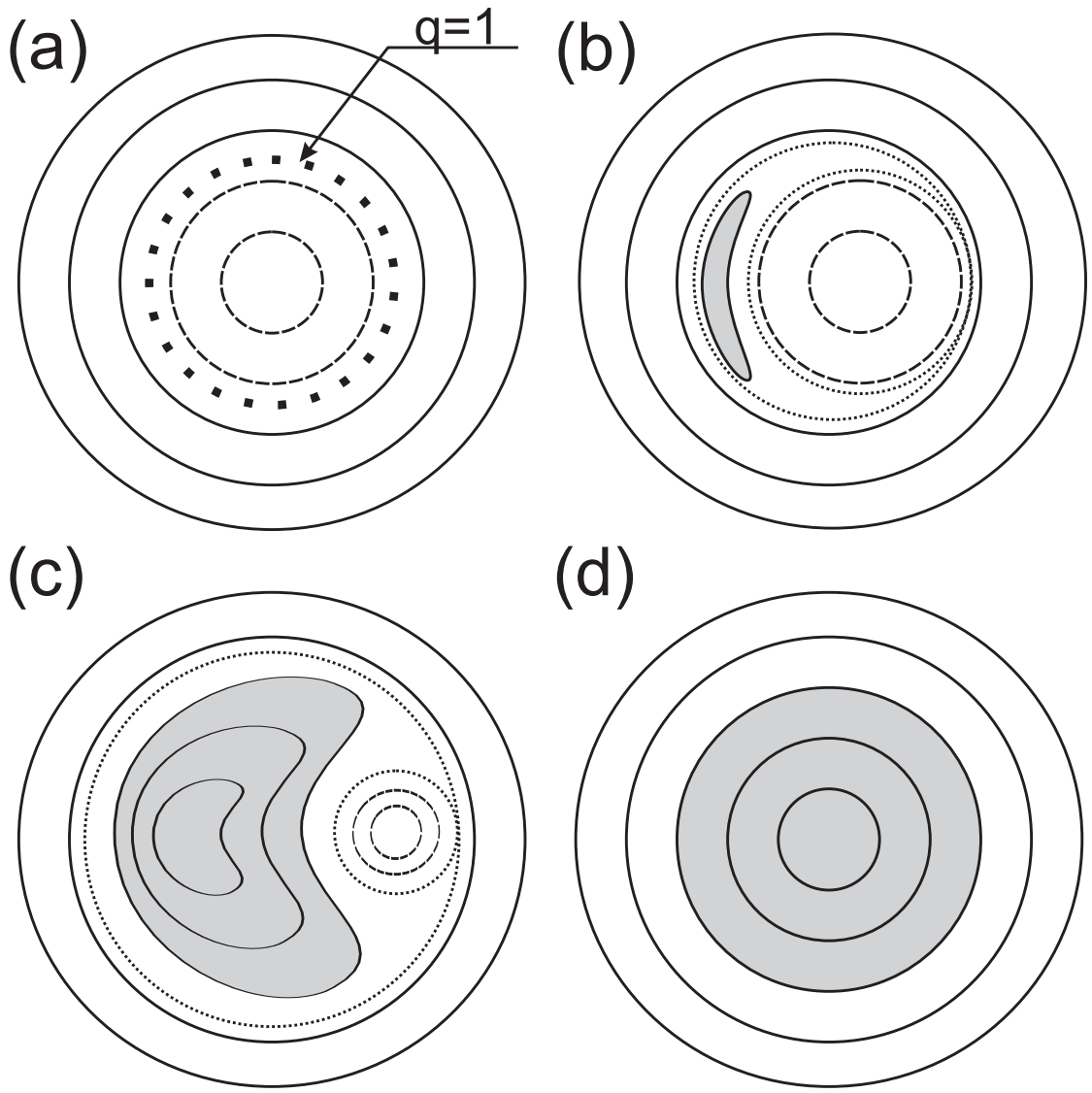

Figure 3.2: Development of the magnetic field structure during the sawtooth instability according to Kadomtsev's model. The m=1 instability(gray region) displaces the region inside the $q = 1$ surface(dashed lines). The dotted line indicates the separatrix.

To illustrate the main idea of Kadomtsev's reconnection model, let us calculate the reconnected helical flux and the safety factor profile. For simplicity we assume a parabolic profile for the plasma current density before the sawtooth crash

$$j(r) = j_0 \left(1 - \left(\frac{r}{a}\right)^2\right), \tag{3.4}$$

where j_0 is the on-axis current density. The corresponding safety factor profile is determined by

$$q(r) = \frac{q_0}{1 - \frac{1}{2}\left(\frac{r}{a}\right)^2}, \tag{3.5}$$

where q_0 is the safety factor on the magnetic axis. Substituting Equation (3.5) into Equation (3.1) and then integrating Equation (3.2) we obtain the initial helical flux before the sawtooth crash

$$\psi_{\text{ini}}(r) = \frac{B_\phi r^2}{8Rq_0}\left[4(1-q_0) - \left(\frac{r}{a}\right)^2\right]. \tag{3.6}$$

Kadomtsev's model suggests that the final helical flux can be calculated from the flux diagram shown in Figure 3.3a. Before the crash the regions dr_- and dr_+ are covered by equal flux elements, $d\Psi$. These regions, which are located on the inner and the outer sides of the r_1, will connect and form a single flux element $d\Psi$ covering the region rdr at the radius r. The reconnection starts around the $q = 1$ surface, where the initial helical flux reaches its maximum, Ψ_{max}. The flux element at the r_1 will form the new centre of the plasma and therefore the central value of the flux after the crash is equal to the maximum value of the flux before the crash. The poloidal area covered by the poloidal flux element $d\Psi$ is conserved throughout the crash, that is

$$rdr = r_-dr_- + r_+dr_+. \tag{3.7}$$

After integrating Equation (3.7),

$$\int_0^r rdr = \int_{r_-}^{r_1} r_-dr_- + \int_{r_1}^{r_+} r_+dr_+, \tag{3.8}$$

we obtain

$$r^2 = r_+^2(\psi) - r_-^2(\psi), \tag{3.9}$$

where r is the minor radius of the final helical flux after the magnetic reconnection. r_- and r_+ can be obtained directly from Equation (3.6) by

$$r_\pm^2(\psi) = a^2\left[2(1-q_0) \pm \sqrt{4(1-q_0)^2 - \frac{8Rq_0}{B_\phi a^2}\psi}\right]. \tag{3.10}$$

After substituting Equation (3.10) into 3.9 the final reconnected helical flux is given by

$$\psi_{\text{fin}} = \frac{B_\phi a^2}{8Rq_0}\left[4(1-q_0)^2 - \left(\frac{r}{\sqrt{2}a}\right)^4\right]. \tag{3.11}$$

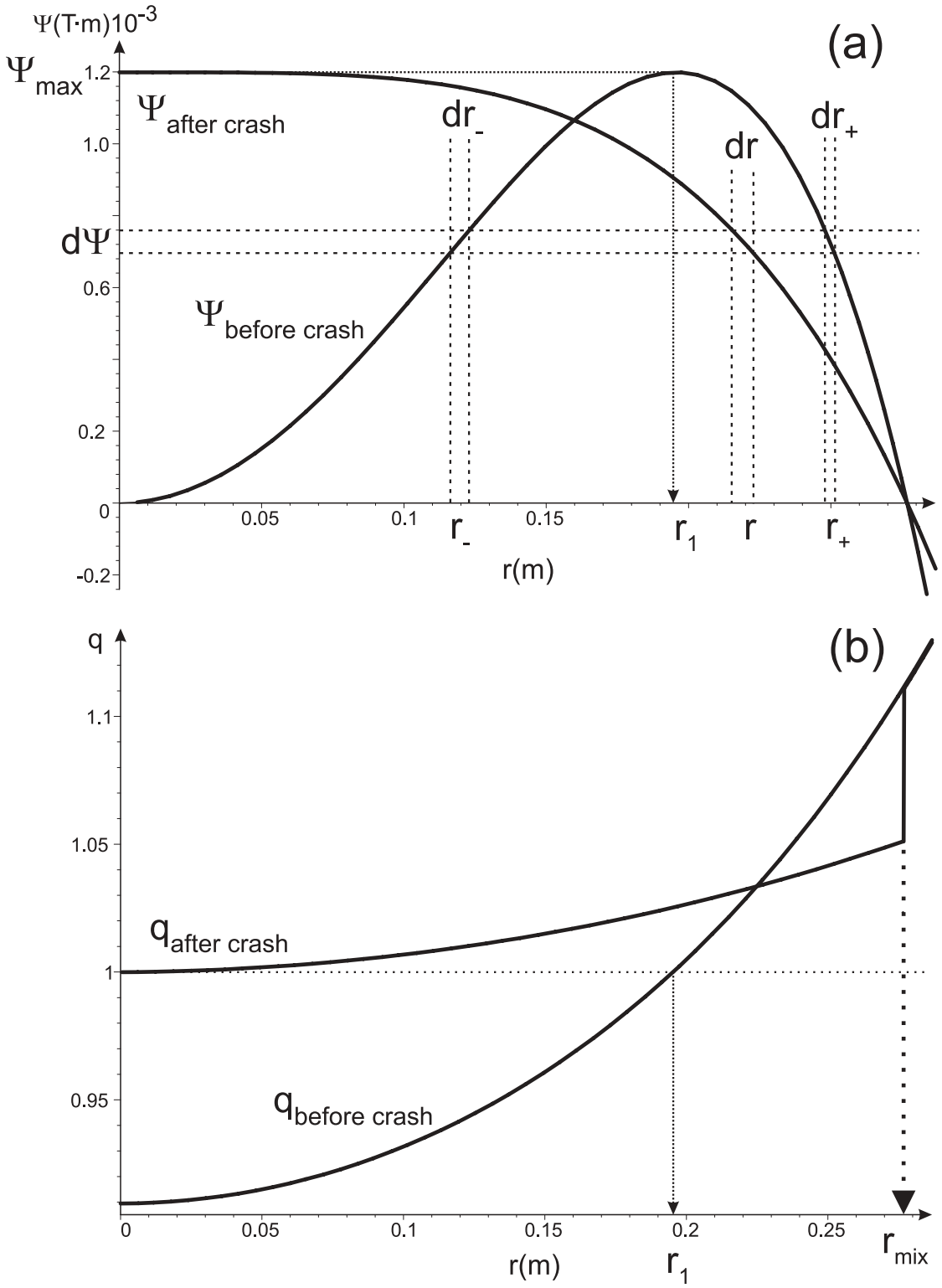

Figure 3.3: The safety factor, $q(r)$, and helical magnetic flux, $\Psi(r)$ profiles before and after the sawtooth crash according to the Kadomtsev's reconnection model. The calculation of the profiles is performed for the TEXTOR geometry with major radius $R = 1.75$ m, minor radius $a = 0.46$ m and toroidal magnetic field $B_\phi = 2.2$ T.

This final helical flux is defined up to the mixing radius r_{mix}, which determines the end of the reconnection region as shown in Figure 3.3. The helical flux changes sign at the mixing radius, $\psi_{\text{fin}}(r_{\text{mix}}) = 0$, and therefore from Equation (3.11)

$$r_{\text{mix}} = 2a\sqrt{1 - q_0}. \tag{3.12}$$

The rest of the helical flux beyond r_{mix} is left intact and hence, the total helical flux is a piecewise function. As a consequence, the final safety factor profile after the sawtooth crash has a discontinuity at the mixing radius (see Figure 3.3b). From Equations (3.1), (3.2) and (3.11) the final q profile inside the mixing radius is given by

$$q_{\text{fin}}(r) = \left[1 - \frac{r^2}{8a^2 q_0}\right]^{-1}, \qquad r < r_{\text{mix}}. \tag{3.13}$$

The q profile beyond the mixing radius is left unchanged as is the helical flux. The central value of the final q profile is equal to unity. Figures 3.3a and 3.3b summarise the changes in the helical flux and the safety factor profile from the initial to the final state. The above calculations can be repeated for the plasma equilibrium of any complexity by following the main idea of determining the new coordinates of the reconnected flux (see Equations (3.7) and (3.9)). For a more complicated plasma equilibrium the resulting flux is usually obtained numerically.

3.3 Model for the sawtooth trigger

The previous section discusses the sawtooth crash phase and the magnetic reconnection during the crash. This crash is triggered by the internal instability with toroidal n=1 and dominant poloidal m=1 mode numbers. This section discusses the method of analysing the stability boundaries of this mode by using the energy principle. Moreover, the growth rates of the unstable mode in different collisional regimes are considered.

One of the methods to analyse the stability of a dynamic system, such as magnetically confined plasma, is to evaluate the change in the potential energy of the system due to a small perturbation. The very well known example [4] is a ball either at the bottom of a trough or on the top of a hill (see Figure 3.4). In the first case if the ball is slightly displaced its potential energy increases, whereas in the second case for the same displacement the potential energy decreases. The system is stable in the first situation and unstable in the second.

This simple illustration reflects the energy principal of ideal MHD which is based on the concept that a plasma equilibrium is unstable if a small perturbation of the equilibrium lowers the potential energy. The change in the potential energy of the plasma as a result of a arbitrary displacement $\vec{\xi}$ is given by the volume integral

$$\delta W = -\frac{1}{2}\int \vec{\xi}\vec{F}dV, \tag{3.14}$$

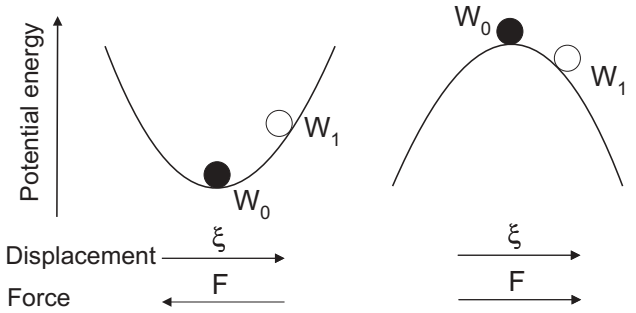

Figure 3.4: Illustration of the energy principle to analyse the stability of a dynamic system.

where $\vec{F}$ is the force arising from the displacement. The plasma is unstable if δW is negative for any small $\vec{\xi}$. Therefore, to conclude that an equilibrium is unstable it is enough to find only one displacement $\vec{\xi}$ which leads to negative δW.

The instabilities which are obtained assuming that the plasma is a perfectly conducting media are called ideal MHD instabilities. In reality the plasma has a finite resistivity which might affect the results of ideal MHD stability analysis. It is to be expected that the plasma is unstable if the ideal MHD theory predicts instability, however, the resistivity might be important in the nonlinear development of the unstable mode. On the other hand if the plasma is predicted to be ideal MHD stable, the plasma may or may not be stable.

The internal instability with the poloidal number m=1 and the toroidal number n=1, which triggers the sawtooth crash, is called internal kink instability. Let us look at the behaviour of this mode in different plasma approximations, such as ideal and resistive MHD. The ideal MHD calculation in the toroidal geometry is quite complicated, therefore, only the essential results are summarised here. It was shown [10] that for the circular cross section tokamak in a large aspect ratio approximation ($r/R << 1$), small $\Delta q = 1 - q(0)$ and for the family of q profiles $q(r) = 1 - \Delta q(1 - (r/r_1)^\nu)$, the potential energy of the plasma is proportional to

$$\delta W \sim 3\nu(1-q_0)\left[\frac{13}{48(\nu+4)} - \beta_{p1}\int_{r_1}^{a}\frac{dr}{r_1}\left(\frac{r}{r_1}\right)^{\nu-5}\right], \tag{3.15}$$

where

$$\beta_{p1} = \frac{2\mu_0\int_0^{r_1}(p(r)-p(r_1)2rdr)}{(B_\theta(r_1)r_1)^2}, \tag{3.16}$$

where q_0 is the safety factor on axis, $p(r)$ is a plasma pressure, r_1 is a minor radius of the $q = 1$ surface and $B_\theta(r_1)$ is a poloidal magnetic field at the $q = 1$ surface. From Equation (3.15) it follows that the for the $\nu < 4$ and $r_1 = 0$ the critical value of β_{p1} is given by

$$\beta_c = \left[\frac{13(4-\nu)}{48(4+\nu)}\right]^{\frac{1}{2}}. \tag{3.17}$$

If β_{p1} exceeds β_c than the ideal internal kink becomes unstable. From Equation (3.16) it is clear that the unstable mode in the ideal MHD is driven by the pressure gradient.

For the parabolic current density profile with $\nu = 2$ Equation (3.17) gives the instability for $\beta_{p1} > 0.3$.

The introduction of resistivity changes the mode dynamic when the potential energy δW is close to zero. Porcelli [5] proposed a model which combines stability boundaries and triggering conditions for different types of the unstable mode. In the following discussion we will use the normalisation of the energy functional adopted by Porcelli

$$\delta\hat{W} \equiv -\frac{4\delta W}{s_1 \xi^2 \varepsilon_1^2 R B^2}, \tag{3.18}$$

where s_1 is the shear at the $q = 1$ surface, ξ is the radial displacement of the magnetic axis, $\varepsilon_1 = \bar{r_1}/R$ ($\bar{r_1}$ is the average radius of the $q = 1$ surface), R is the major radius and B is the magnetic field. For the definition of shear see Section 2.2.4.

The macroscopic drive of the mode is described by the effective potential energy functional which includes the ideal MHD potential energy, $\delta\hat{W}_{\text{MHD}}$, contribution from the thermal trapped ions $\delta\hat{W}_{\text{trapped}}$ and kinetic effects related to high energy particles $\delta\hat{W}_{\text{fast}}$

$$\delta\hat{W} = \delta\hat{W}_{\text{MHD}} + \delta\hat{W}_{\text{trapped}} + \delta\hat{W}_{\text{fast}}. \tag{3.19}$$

According to this model the physics in a narrow 'resistive layer' around the $q = 1$ surface becomes important when the potential energy is close to marginal stability

$$-0.5\omega_{*i}\tau_A < \delta\hat{W} < \frac{\rho_i}{r_1}, \tag{3.20}$$

where ω_{*i} is the ion diamagnetic frequency, τ_A is the Alfvén time and ρ_i is the ion Larmor radius. The full expressions for these quantities can be found in the appendix to this chapter. In the asymptotic limit

$$-\delta\hat{W} > \max\left(\rho_i/r_1, 0.5\omega_{*i}\tau_A\right) \equiv \delta\hat{W}_{\text{crit}}, \tag{3.21}$$

when the layer physics effects become negligible the growth rate of the internal kink mode is given by

$$\gamma = -\frac{\delta\hat{W}}{\tau_A}. \tag{3.22}$$

A large positive value of the potential functional $\delta\hat{W} > \rho_i/r_1$ indicates that the mode changes its structure from the internal kink to the drift tearing mode. However, this is outside of the scope of this chapter, since the tearing mode does not lead to sawtooth oscillations. The schematic stability diagram—which indicates the nature of the unstable mode as a function of the potential energy functional $\delta\hat{W}$ and triggering condition—is shown in Figure 3.5.

Let us consider the region where the layer physics is important (see Inequality 3.20) and the potential energy is close to its marginal stability. The nature of the unstable mode and its growth rate are determined by several characteristics lengths. The width of the thin layer around the $q = 1$ surface, where the m=1 mode starts to reconnect,

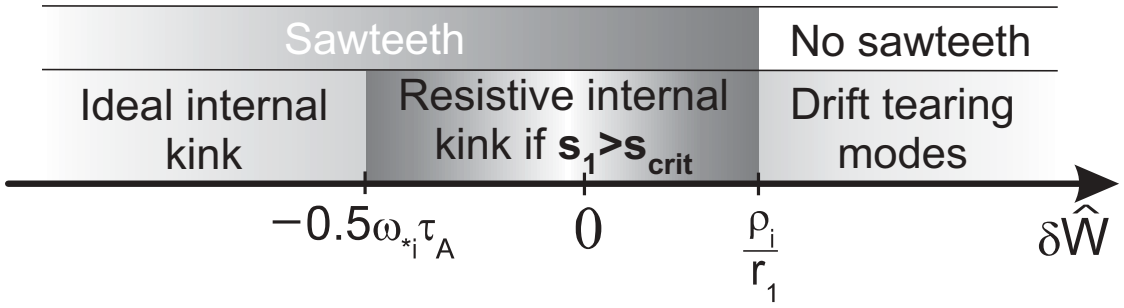

Figure 3.5: Schematic diagram of the sawtooth triggering condition as a function of the potential energy.

depends on the values of the ion Larmor radius ρ_i, the resistive layer width δ_η and the internal skin depth d_e(see appendix). If they satisfy the criterion $\rho_i > \delta_\eta > d_e$ than the internal kink is in 'ion-kinetic' regime and its growth rate is [15]

$$\gamma_\rho = \left(\frac{2(1+T_e/T_i)}{\pi}\right)^{2/7} \left(\frac{\rho_i}{r_1}\right)^{4/7} S^{-1/7} s_1^{6/7} \frac{1}{\tau_A}, \tag{3.23}$$

where S is the Lundquist number(see appendix) and s_1 is the shear at the $q = 1$ surface. In the situation, when the ion Larmor radius is smaller than the resistive layer width, $\delta_\eta > \rho_i > d_e$, the internal resistive kink becomes unstable with the growth rate

$$\gamma_\eta = s_1^{2/3} S^{-1/3} \frac{1}{\tau_A}. \tag{3.24}$$

According to Porcelli in this interval the m=1 mode can be stabilised by the ion diamagnetic and electron drift frequency effects. The stabilisation criterion requires that the diamagnetic frequency ω_{*i} is 2-4 times larger than the growth rate of the mode evaluated at $\omega_{*i} = 0$. Hence, the triggering condition can be written as

$$c_* \gamma > \omega_{*i}, \quad c_* \approx [2:4]. \tag{3.25}$$

Since the growth rates γ_η and γ_ρ depend on the shear at the $q = 1$ surface the stability criterion (3.25) can be rewritten as

$$s_1 > s_{1\text{crit}}. \tag{3.26}$$

Therefore, if condition (3.20) is satisfied, the sawtooth model specifies that the crash is triggered once the shear at the $q = 1$ surface exceeds a critical value $s_{1\text{crit}}$.

In conclusion, the sawtooth crash is triggered if one of the following conditions is met (the fast particle stabilisation condition is omitted here, since the TEXTOR tokamak has almost no fast ions)

$$-\delta\hat{W} > 0.5\omega_{*i}\tau_A, \tag{3.27}$$

$$-0.5\omega_{*i}\tau_A < \delta\hat{W} < \frac{\rho_i}{r_1} \text{ and } \omega_{\text{diai}} < c_* \max(\gamma_\rho, \gamma_\eta). \tag{3.28}$$

The most practical approach using the sawtooth crash theory is by coupling the crash triggering conditions (3.27),(3.28) and reconnection model in a transport code: after a sawtooth crash the subsequent rise phase can be simulated by the transport code until a plasma state is reached in which the sawtooth triggering conditions are again satisfied. At that point the normal discharge evolution can be interrupted to calculate the redistribution of the central plasma according to the sawtooth reconnection model. In this way, Porcelli's model [5] describes the full cycle of the sawtooth oscillation, covering the rise and the crash phases. The model for the rise phase with a build up of the shear until it reaches a critical values is discussed in Chapter 4.

3.4 Calculations of the critical shear for TEXTOR

This section contains a calculation of the sawtooth triggering conditions, described in the previous section, for the typical parameters of the TEXTOR plasma.

First, we have to determine the regime of the plasma with respect to the internal kink mode. Considering that for the typical TEXTOR plasma the terms describing the trapped thermal ions effects and the kinetic effects due to the fast particles in Equation (3.19) can be neglected, the potential energy is mainly determined by the ideal MHD energy, $\delta\hat{W}_{\mathrm{MHD}}$. For simplicity we assume a parabolic pressure profile

$$p(r) = p_0\left(1 - \left(\frac{r}{a}\right)^2\right) \tag{3.29}$$

and a monotonic $q(r)$ profile with a small $\Delta q = 1 - q(0)$. An analytic expression of the ideal MHD potential energy functional for the parabolic current density profile and small r_1/a is given by

$$\delta\hat{W}_{\mathrm{MHD}} = -3(1 - q(0))\left(\beta_{p1} - \frac{13}{144}\right), \tag{3.30}$$

where β_{p1} is defined in Equation (3.16) and B_θ is poloidal magnetic field.

For the typical poloidal beta in TEXTOR ~ 0.3 the ideal MHD energy is of the order of $3 \cdot 10^{-3}$, whereas $\rho_i/r_1 \sim 10^{-2}$ and $0.5\omega_{*i}\tau_A \sim 10^{-3}$. Therefore, for these parameters the condition (3.20) is fulfilled and the mode dynamic is determined by the layer physics effects. Assuming the ion and electron temperatures $T_{\mathrm{i}} = T_{\mathrm{e}} = 2\,\mathrm{keV}$, electron density $n_{\mathrm{e}} = 2 \cdot 10^{19}\,\mathrm{m}^{-3}$ and toroidal magnetic field $B_{\mathrm{t}} = 2.5\,\mathrm{T}$, the main scale lengths are $\rho_i \sim 0.28\,\mathrm{cm}$, $\delta_\eta \sim 0.17\,\mathrm{cm}$ and $d_e \sim 0.11\,\mathrm{cm}$. They satisfy the condition $\rho_i > \delta_\eta > d_e$, which determines the ion-kinetic collisional regime, and the growth rate of the resistive kink is determined by Equation (3.23). However, for a lower temperature it is possible that $\rho_i < \delta_\eta$ and the growth rate of the mode is given by Equation (3.24). Therefore, both growth rates have to be taken into account—when computing the stability criterion (3.25)—with the effective growth rate

$$\gamma_{\mathrm{eff}} = \max(\gamma_\rho, \gamma_\eta). \tag{3.31}$$

This condition considers that the more unstable mode drives the instability. Figures 3.6(a) and 3.6(b) show contours of the critical shear as a function of electron

temperature and density for two different values of the toroidal magnetic field, 2.2 T and 2.5 T—the constant c_* in the condition (3.25) was chosen equal to 2. The obtained values of the critical shear are in agreement with the calculation of the shear evolution at the $q = 1$ surface from Chapter 4.

3.5 Appendix: Relevant m=1 stability parameters

Here is the list of formulas for the quantities relevant to the m=1 mode instability.
Alvfén speed

$$\upsilon_A = \frac{B}{\sqrt{\mu_0 n_i m_i}}. \tag{3.32}$$

Alvfén time

$$\tau_A = \frac{\sqrt{3}R}{\upsilon_A}. \tag{3.33}$$

Pressure scale length at the $q = 1$ surface

$$r_{p1} = p(r_1) \left| \frac{dp}{dr} \right|^{-1}_{r=r_1}. \tag{3.34}$$

Diamagnetic frequency

$$\omega_{*i} = \frac{T}{eBr_1 r_{p1}}. \tag{3.35}$$

Resistive diffusion time

$$\tau_\eta = \frac{\mu_0 r_1^2}{\eta_{||}}. \tag{3.36}$$

Lundquist number

$$S = \frac{\tau_\eta}{\tau_A}. \tag{3.37}$$

Resistive kink layer width

$$\delta_\eta = s_1^{-1/3} S^{-1/3} \tau_A^{-1}. \tag{3.38}$$

Electron plasma frequency

$$\omega_{pe} = \sqrt{\frac{n_e e^2}{\varepsilon_0 m_e}}. \tag{3.39}$$

Inertial skin depth

$$d_e = \frac{c}{\omega_{pe}}. \tag{3.40}$$

Ion Larmor radius

$$\rho_i = \sqrt{\frac{mc^2 T}{e^2 B^2}}. \tag{3.41}$$

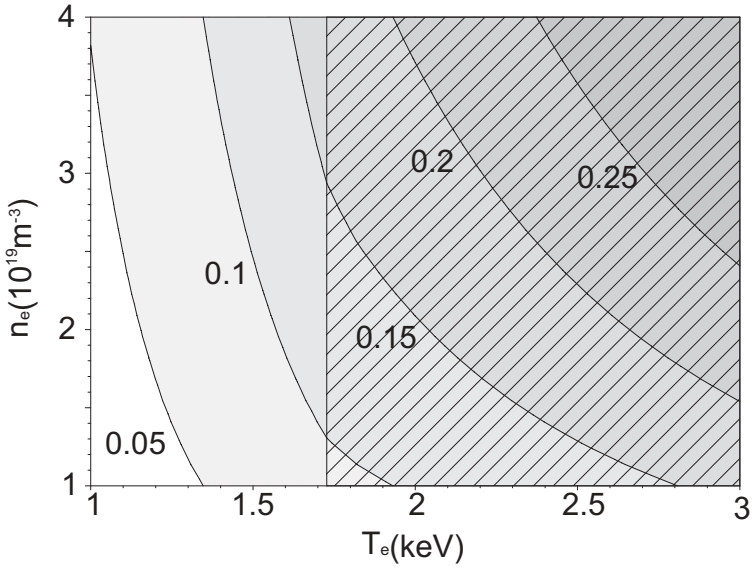

(a) B_t = 2.2 T

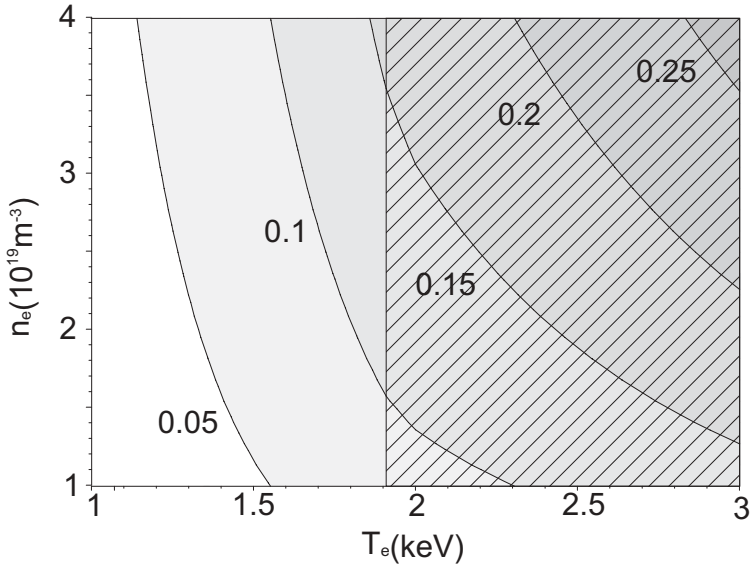

(b) B_t = 2.5 T

Figure 3.6: Contour plots of the critical shear as a function of the electron temperature and density at the q=1 surface for different values of the toroidal magnetic field. The contours are obtained for a parabolic pressure profile (see Equation (3.29)) and the $c_* = 2$ (see Equation (3.25)). Shaded regions indicate that the plasma is in the ion-kinetic regime and unshaded regions correspond to the resistive regime.

Bibliography

[1] Goeler S *et al* 1974 *Phys.Rev.Lett.* **33** 1201

[2] Kadomtsev B 1975 *Sov. J. Plasma Phys.* **1** 389

[3] Wesson J 2004 *Tokamaks, Third Edition, Clarendon Press-Oxford*

[4] Goedbloed J P and Poedts S *Principles of Magnetohydrodynamics: With Applications to Laboratory and Astrophysical Plasmas*, Cambridge, 2004

[5] Porcelli F *et al* 1996 *Plasma Phys. Control. Fusion* **38** 2163

[6] Hastie R 1998 *Astrophysics and Space Science*, **256** 177

[7] Kruskal M D *et al* 1958 *Phys. Fluids* **1** 275

[8] Porcelli F 1991 *Plasma Phys. Control. Fusion* **33** 1601

[9] Coppi B *et al* 1990 *Phys. Fluids* **2** 927

[10] Bussac M N *et al* 1975 *Phys.Rev.Lett.* **35** 1638

[11] Campbell D J *et al* 1988 *Phys.Rev.Lett.* **60** 2148

[12] Lutjens H *et al* 1992 *Nuclear Fusion* **32** 1625

[13] Kuvshinov B N *et al* 1987 *Sov. J. Plasma Phys.* **13** 527

[14] Antonsen T M *et al* 1993 *Phys. Fluids* **5** 4090

[15] Pegoraro F *et al* 1989 *Phys. Fluids* **1** 364

[16] Sauter O *et al* 1998 *Proceedings of the Joint Varenna-Lausanne International Workshop on "Theory of Fusion Plasmas"* 403

[17] Zakharov L *et al* 1993 *Phys. Fluids* **5** 2498

[18] Livinton F M *et al* 1994 *Phys.Rev.Lett.* **72** 2895

Chapter 4

Sawtooth period control by localised non-inductive current drive

A Merkulov†, E Westerhof†, F C Schüller†, M R de Baar†, A Krämer-Flecken‡, Y Liang‡, and TEXTOR Team‡

†FOM-Institute for Plasma Physics Rijnhuizen, Association EURATOM-FOM, Trilateral Euregio Cluster, The Netherlands, www.rijnh.nl

‡Institut für Plasmaphysik, Forschungszentrum Jülich GmbH, EURATOM Association, D-52425 Jülich, Germany.

This paper is submitted to Nuclear Fusion

Abstract.

Starting from the assumption that a sawtooth crash is triggered when a critical shear at the $q = 1$ surface is exceeded (Porcelli et al. 1996 Plasma Phys. Control. Fusion 38 2163), the effects of localised non-inductive current drive on the sawtooth period are studied. On the basis of simplified diffusion calculations it is shown that in order to significantly affect the sawtooth period the driven current must satisfy the criterion $I_{cd} > 2\left(\Delta r / r_{q=1}\right)^2 I_{q=1}$, where Δr is the Gaussian width of the driven current profile and $I_{q=1}$ the total current inside the $q = 1$ surface, $r_{q=1}$. Co-current deposited inside/outside the q=1 surface is shown to speed-up/slow-down the shear evolution at $q = 1$ and, consequently, to destabilize/stabilize sawteeth. The reverse is found for counter-current drive.
In order to confirm these predictions experimentally, the effects of electron cyclotron current drive on sawtooth oscillations have been studied in the TEXTOR tokamak. The experiments are complicated by the concurrent electron cyclotron heating, which also has a significant impact on the sawtooth period. By normalising the sawtooth period response as a function of the power deposition radius to a case with only heating, the effects of current drive can be separated. The results qualitatively confirm the model predictions.

4.1 Introduction

Most tokamak discharges exhibit central relaxation oscillations of the density and temperature called sawtooth oscillations [1]. During a sawtooth crash the particles, energy and current in the centre are redistributed resulting in almost completely flat profiles inside the $q = 1$ surface. This limits the maximum plasma pressure in the centre and, consequently, the obtainable fusion power in a tokamak reactor. In addition, the perturbations induced by sawteeth are seen to trigger other instabilities like neoclassical tearing modes [2], which can further deteriorate plasma performance. On the other hand, the sawtooth oscillations prevent the accumulation of impurities in the centre. For example, in a burning fusion plasma with deuterium and tritium, high energetic α particles are generated, becoming He ash after thermalisation. Studies [3, 4, 5] indicate that low transport of helium ash from the core to the edge compared to its production rate can quench the burning reaction. Therefore, control of the He ash in the centre of the plasma is one of the important issues in tokamak experiments. All above mentioned points call for active control of sawtooth oscillations in order to minimise their disadvantages, yet keeping their positive effects.

Sawteeth occur when the central safety factor q drops below one, and the sawtooth crash has been associated with a complete reconnection of the helical magnetic field on opposite sides of the $q = 1$ surface [6]. Porcelli *et al.* [7] have derived a sawtooth model in which the instability leading to the crash is triggered when the magnetic shear at $q = 1$ reaches a critical value [8]. This critical shear value depends on the plasma parameters like β and pressure gradient length inside and at the $q = 1$ surface. This suggest the possibility to control the sawtooth period by control of the evolution of the magnetic shear at the $q = 1$ surface. The most direct way to affect this shear evolution will be by means of localised noninductive current drive as with, for example, electron cyclotron waves. Experiments with electron cyclotron resonance heating (ECRH) and current drive (ECCD) indeed show a strong influence on the sawtooth period (see *e.g.* [9, 10, 11]). Modelling of the experiments on TCV with ECRH and ECCD has shown the importance of even relatively small, localised, noninductive currents [12]. Both the results from the TCV and ASDEX Upgrade experiments could be understood within the framework of the Porcelli model for the sawteeth [9, 11, 12]. In experiments on JT-60 the switch-on of ECRH or ECCD was also shown to lead to a strong transient effect on the sawtooth period [13]. These and other methods of sawtooth control are reviewed in [14].

In this paper, we present a simplified model for the poloidal field evolution following a sawtooth crash. This model includes effects of a localised noninductive current drive with a Gaussian profile and assumes Spitzer resistivity of the plasma. The purpose of this model is to provide simple criteria for the position, width and amount of the applied noninductive current, which are necessary to have a substantive impact on the evolution of the shear and, consequently, on the sawtooth period. In order to avoid calculations of the plasma transport the temperature profile is taken constant during the sawtooth crash. The ASTRA (Automated System for TRansport Analysis) numerical code [15] will be used to asses the validity of this approximation. ASTRA code solves the 1-D fluid transport equations. The simplicity of the model allows us

to scan throughout a wide range of current drive parameters as well as investigate the difference in the shear evolution for the full and partial reconnection cases. In Section 4.4 of this work the experimental verification of the model is demonstrated. As experimental scenario a magnetic field sweep was prepared to scan the deposition position of a localised noninductive current induced by ECRH. The results are analysed to separate the influences of the EC heating and the effect of the current drive. The TORBEAM code [22] is used to estimate the amount and the localisation of the noninductive current drive. This code is based on the beam tracing technique and, therefore, provides relatively fast yet reliable calculations. We shall see that even the simple poloidal field evolution model is capable of describing the main features which are observed in the experiments.

4.2 Shear evolution between sawtooth crashes

The large aspect ratio approximation for circular cross-section is used, such that the safety factor can be taken as $q = rB_\phi/R_0B_\theta$, where $B_{\phi,\theta}$ are the toroidal and poloidal fields, and R_0 is the major radius. The evolution of the poloidal magnetic field follows from the induction equation and Ohm's law and is written in normalised form as

$$\frac{\partial b}{\partial \tau} = \frac{\partial}{\partial x}\left[\frac{\bar{\eta}(x,\tau)}{x}\frac{\partial (xb)}{\partial x} - \bar{\eta}(x,\tau)\bar{j}_{cd}(x,\tau)\right]. \tag{4.1}$$

The bootstrap current is neglected in this representation. In order to allow a quick calculation of the poloidal field evolution, the temperature profile is taken constant $T_e(r) = T_0\left(1-\left(\frac{r}{a}\right)^2\right)^2$, thus neglecting the temperature evolution during the sawtooth cycle. This approximation will be justified at the end of Section 4.3 by comparison with transport code calculations including a more complete simulation of the temperature evolution. The temperature profile determines the steady state current density profile (in the absence of noninductive current drive) that would be obtained without sawteeth. The normalisation is based on this steady state profile, with radius and magnetic field being normalised to their values at the $q = 1$ surface: $x \equiv r/r^\infty_{q=1}$, and $b \equiv B_\theta/B^\infty_{\theta,q=1}$, where the superscript ∞ indicates the steady state. Time is normalised to the corresponding resistive diffusion time: $\tau \equiv t/\tau_R$ with $\tau_R = \mu_0(r^\infty_{q=1})^2/\eta_n$ and $\eta_n = 1.65\cdot 10^{-9}\ln\Lambda T_0^{-3/2}$ [keV], $Z_{eff} = 1$,where the Coulomb logarithm is taken $\ln\Lambda = 17$. Spitzer resistivity is used, neglecting neoclassical corrections. When normalised to η_n, this gives $\bar{\eta}(x) = (1-(\gamma x)^2)^{-3}$, where $\gamma = r^\infty_{q=1}/a$. The value γ determines the safety factor at the plasma edge, $q_a = \gamma^{-2}(1-(1-\gamma^2)^4)$. The calculations use the typical value $\gamma = 0.3$. The current density finally is normalised as $\bar{j} \equiv jB_{\theta,q=1}/\mu_0 r_{q=1}$. It is noted that $B_{\theta,q=1}/\mu_0 r_{q=1}$ corresponds to half the average current density inside $q = 1$. A noninductive current density localised at x_c is specified as $\bar{j}_{cd}(x) = A\exp(-(x-x_c)^2/W^2)$, with amplitude A and Gaussian width W.

In his seminal paper [6], Kadomtsev attributed the sawtooth crash to a complete reconnection of the helical flux on opposite sides of the $q = 1$ surface. The resulting safety factor profile after the crash is virtually flat with q very close to 1 up to the mixing radius, x_r. However, several experimental observations challenged the Kadomtsev

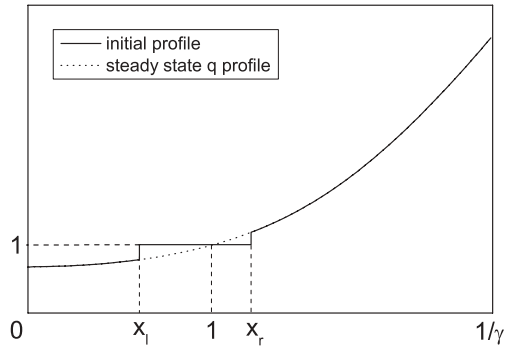

Figure 4.1: The initial distribution of the q profile.

model. The measurements of the $q-$profile indicated that the q value on axis remains below unity during the sawtooth period, with the formation of a region of the low shear around the $q = 1$ surface [17, 18, 19, 20, 21]. These findings suggest that partial reconnection can occur instead of full.

In a first series of calculations the initial condition is set by taking $q = 1$ for $x < x_r$, inline with the Kadomtsev model. For $x \geq x_r$ the initial $q-$profile is identical to its steady state value. The possibility of partial reconnection is included in our model by restricting the flat region in the initial q profile also from the left, i.e. $q = 1$ for $x_l < x < x_r$ (see Figure 4.1), while the initial q-profile inside x_l now is also taken identical to its steady state value. A second series of calculations has been performed to address the question of the influence of the flat region size to the shear evolution. Note that, the evolution of the shear at $q = 1$, which in normalised quantities is expressed as

$$s_{q=1} = x_{q=1} \left.\frac{dq}{dx}\right|_{q=1}, \qquad \text{with } q(x) = \frac{x}{b(x)}, \tag{4.2}$$

will in first approximation be independent of the extend of the region in which q is flattened, provided it is sufficiently large.

4.3 Results

A large number of calculations has been run for the given temperature profile and fixed values of $\gamma = r^{\infty}_{q=1}/a = 0.3$, corresponding to a safety factor at the edge of $q_a = 3.5$, and of the sawtooth mixing radius $x_r = 1.2$. In first approximation, assuming full reconnection, the flattened region of the q-profile has been extended to the centre of plasma by setting $x_l = 0$. Both the position x_c and amplitude A of the localised non-inductive current have been varied over a wide range for two values of the Gaussian width $W = 0.15$ and 0.30. To study the effect of the localised noninductive current, $s_{q=1}$ is evaluated in each calculation at $\tau = 2 \times 10^{-3}$. For TEXTOR plasma parameters ($T_0 = 3.3$ keV, $a = 0.46$ m) this corresponds to $t = 10$ ms, a typical sawtooth period. The results are plotted in Figure 4.2, in terms of contours of constant shear as a function of the position x_c and the total noninductive current normalised to the plasma current inside $q = 1$ in the steady state. White indicates the region where $s_{q=1}$ is virtually unaffected by the noninductive current. When localised just inside / outside $r^{\infty}_{q=1}$

a co-driven current is seen to increase / decrease $s_{q=1}$, resulting in a shorter / longer sawtooth period. As expected the reverse is found for counter-drive. The maximum effect is obtained when the noninductive current is localised approximately one Gaussian width away from the $r^{\infty}_{q=1}$ surface, *i.e.* for $x_c \approx 1 \pm W$. This is in agreement with experimental observations [12]. The effect on the shear is proportional to $I_{cd}/I_{q=1}$ and to the square width W^2. This is illustrated in Figure 4.3 which shows a cut through Figure 4.2b at $x_c = 1 + W$, where the effect on the shear evolution is largest, for $W = 0.3$ and two other values of W.

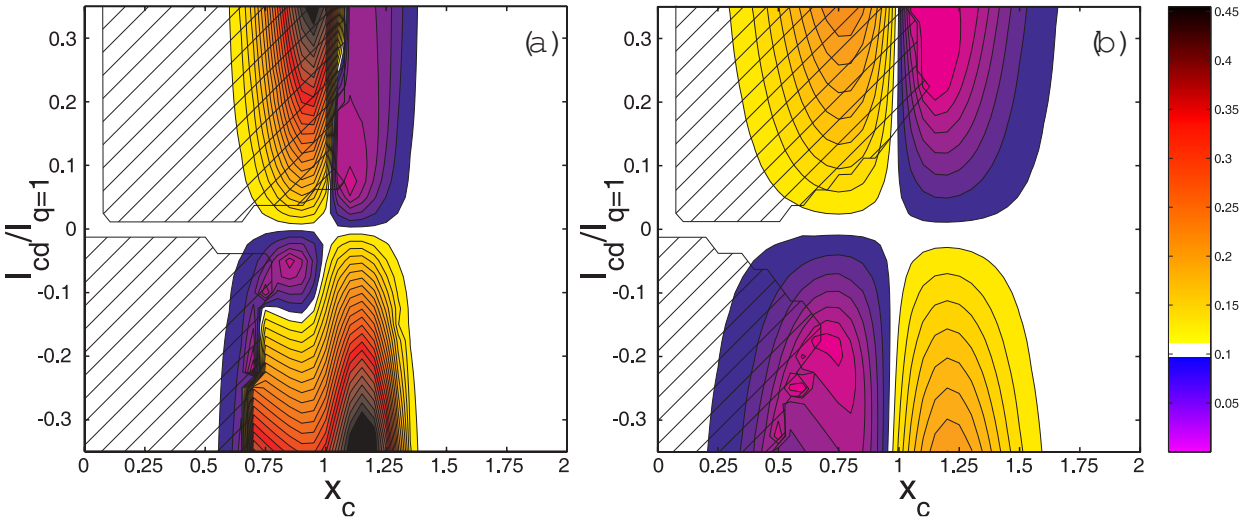

Figure 4.2: The value of $s_{q=1}(\tau = 0.002)$ as a function of deposition radius and the non-inductive current normalised to the total plasma current inside $q = 1$: a) for a normalised Gaussian width of the noninductive current profile $W = 0.15$ (15% of the $q = 1$ radius), and b) for $W = 0.3$. Without the noninductive current $s_{q=1}(\tau = 0.002) = 0.11$, corresponding to the middle of the white region. The shaded regions indicate the presence of multiple $q = 1$ surfaces in the solution.

Note that the actual position of the $q = 1$ surface is varying in time. At the time the shear has been evaluated, the deviation of $x_{q=1}$ from unity is at most a few percent in all reported cases. However, over a wide range of parameters (indicated by the shaded regions in Figure 4.2) with localisation of the noninductive current inside $r^{\infty}_{q=1}$, multiple $q = 1$ surfaces are found in the solution. The shear plotted in Figure 4.2 always refers to the outermost $q = 1$ surface. The additional $q = 1$ surfaces are mostly located close to the axes, and their significance is unclear.

In case of partial reconnection, the flattened region of the q-profile has been limited by setting the x_l parameter to a non zero value. To study the possible effect of the difference in the initial q-profile x_l is varied from 0 to 0.8, what corresponds to shrinking of the flat region in the safety factor profile from the centre almost up to the $q = 1$ surface. The shear plotted in Figure 4.4 is calculated for the Gaussian width of the noninductive current drive profile $W = 0.2$. The behaviour of the shear evolution remained essentially intact even by reducing initial flattening by factor of three ($x_l = 0.8$). At the same time the presence of multiple $q = 1$ surfaces reduced for a

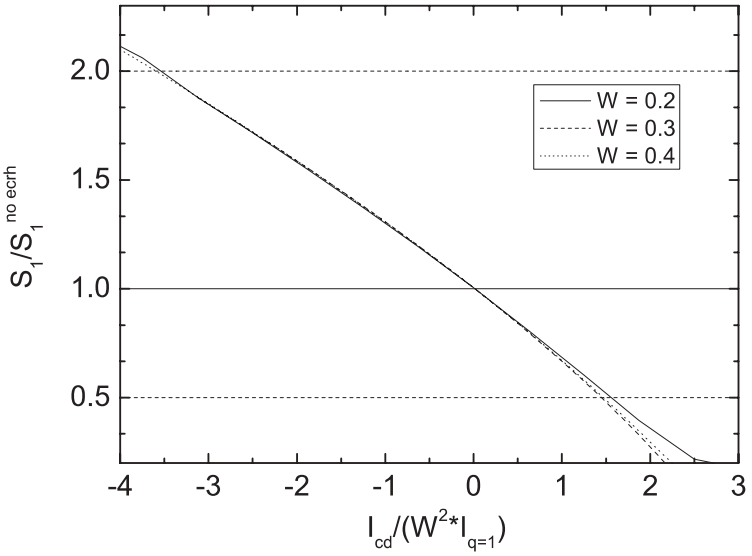

Figure 4.3: The value of $s_1(t = 10ms)$ normalised to the shear at the $q = 1$ surface in absence of current drive, as a function of the driven current normalised to $I_{q=1} * W^2$. The position of the current drive is taken at $x_c = 1 + W$, where the effect is maximum.

wide range of deposition position x_c and noninductive current I_{cd}, which is indicated by shaded regions in Figure 4.4. This result confirms the choice of the outermost $q = 1$ surface to be plotted as a solution of the shear evolution.

The ASTRA code has been used to assess the significance of the neglect of the temperature evolution after a sawtooth crash. The ASTRA calculations start with a flat temperature profile inside the mixing radius, conserving the total energy, and evolves linearly in time to the parabolic profile at $\tau = 0.002$ where the shear again is evaluated. Results of the ASTRA simulations are compared with the model calculations in Figure 4.5. The results calculated with the full temperature evolution in ASTRA only show a difference in terms of a slightly lower base level of the shear obtained in the absence of the noninductive current. The change in $s_{q=1}$ created by the noninductive current compares well with the model calculations. This justifies the approximation with a constant temperature profile in the model calculations.

Taking a factor of two change in the shear (either increasing or decreasing) as a necessary requirement for a significant change in the sawtooth period, the results of the model calculations can be summarised in terms of a required noninductive current for sawtooth period control given by

$$I_{cd} \gtrsim 2W^2 I_{q=1}, \tag{4.3}$$

where W is the Gaussian width of the noninductive current profile normalised to the $q = 1$ radius and $I_{q=1}$ is the total current inside $q = 1$. To achieve the desired effect this current must be localised accurately. When localised about one Gaussian width to the inside of $q = 1$, *i.e.* $x_c \approx 1 - W$, a co-driven current decreases the sawtooth period, while localisation outside $q = 1$, $x_c \approx 1 + W$ is required for increasing the sawtooth period. The reverse holds for counter current drive.

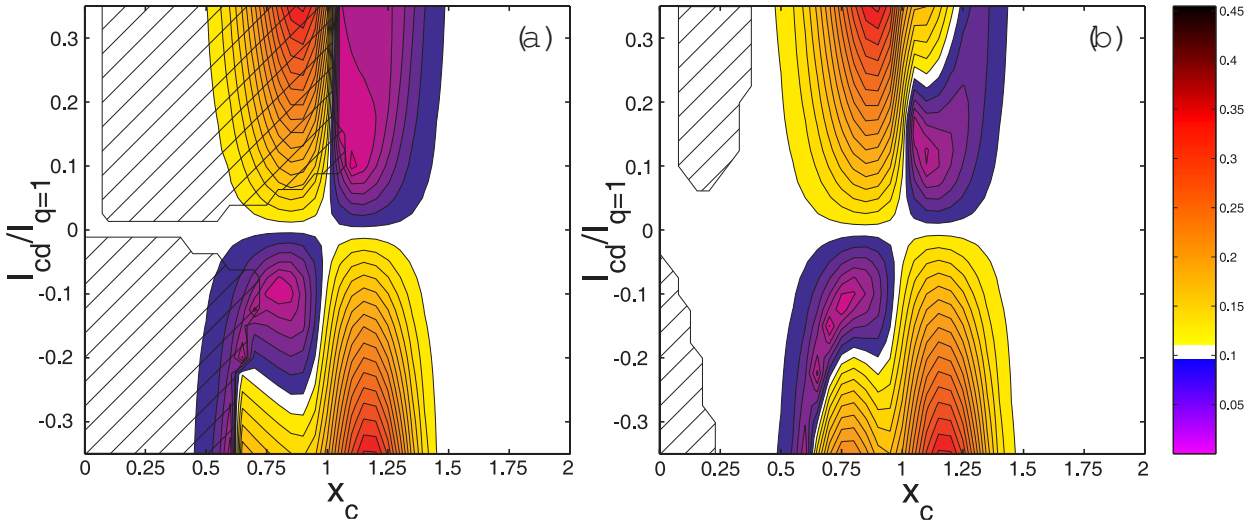

Figure 4.4: The value of $s_{q=1}(\tau = 0.002)$ as a function of deposition radius and the non-inductive current normalised to the total plasma current inside $q = 1$: a) initial q-profile is flat up to the centre ($x_l = 0, x_r = 1.2$) and b) initial q-profile is flat around $q = 1$ surface, $x_l = 0.8, x_r = 1.2$. A normalised Gaussian width of the noninductive current profile $W = 0.2$ (20% of the $q = 1$ radius). Without the noninductive current $s_{q=1}(\tau = 0.002) = 0.11$, corresponding to the middle of the white region. The shaded regions indicate the presence of multiple $q = 1$ surfaces in the solution.

4.4 Experiment

The TEXTOR tokamak is equipped with a 140GHz gyrotron which is capable of generating 800kW of microwave power in a three second pulse. This installation can be used to effectively heat the plasma with EC power as well as to drive substantial amount of ECCD. The long three second pulse makes possible to scan the ECCD deposition, by means of magnetic field sweep, in a wide range of minor radius. Finally, the launcher mirror can be steered in the large range of toroidal and poloidal angles ($\phi = -30^0 .. + 30^0, \theta = -15^0 .. + 15^0$) which is used to vary the ECCD profile width. However, the poloidal angle θ of the launcher mirror was set to zero in the experiment in order to obtain maximum current drive efficiency .

4.4.1 Experimental conditions

To separate the effect of ECCD and ECRH the plasma parameters were kept consistent through the set of plasma discharges. The current of the target plasma was fixed at $350kA$, which corresponds to the edge value of the safety factor of $q_a = 4.4$. Electron temperature $T_e = 2keV$ and line averaged electron density $n_e = 2 \cdot 10^{19}\,\mathrm{m}^{-3}$ were chosen to assure sufficient absorbtion of EC waves and providing considerable ECCD efficiency. The total plasma current, which is conserved inside $q = 1$ surface, $I_{q=1} = 135kA$ corresponds to a $r^{\infty}_{q=1} = 0.3a$ (see Figure 4.6). Two magnetic field ramp scenarios where used with a constant rate of 0.13 T/s. For the discharges with only EC heating and small launcher angles the magnetic field B_t was ramped down from 2.5 T

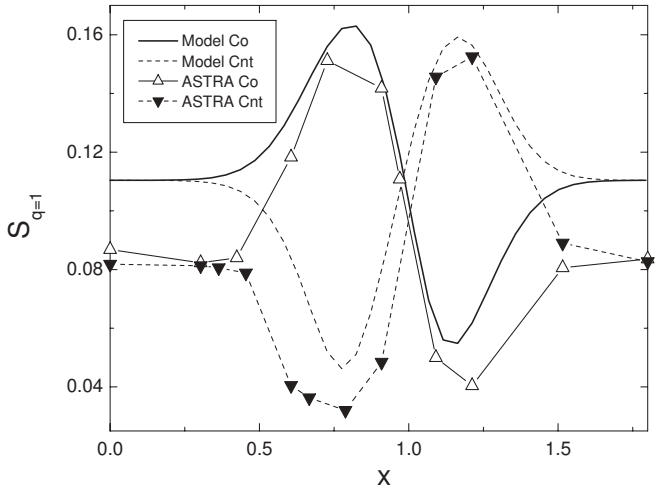

Figure 4.5: Comparison of $s_{q=1}(\tau = 0.002)$ from the model calculations with full ASTRA simulations of the $q-$ profile evolution. The triangles indicate the results from ASTRA calculations and the smooth curves those from the model. The solid and dashed curves correspond to co- and counter-drive, respectively. The parameters used are $I_{eccd}/I_{q=1} = 0.11$, $W = 0.25$, and $\gamma = 0.3$, which for TEXTOR ($R = 1.75$ m, $a = 0.46$ m) corresponds to : $I_p = 440kA, I_{eccd} = 17kA, B_t = 2.5T$.

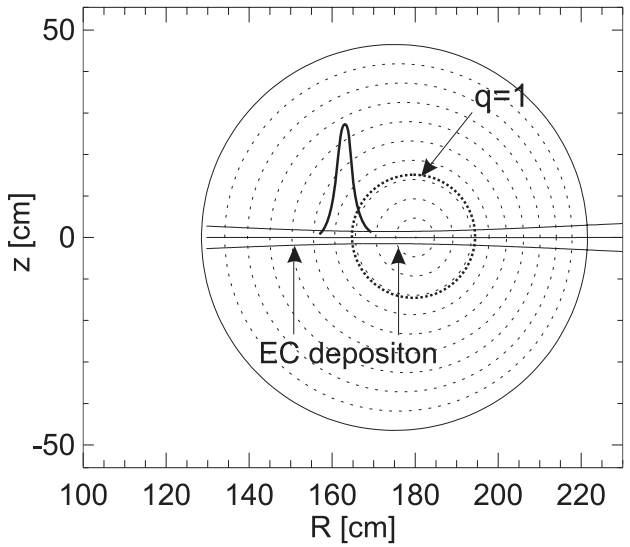

Figure 4.6: The poloidal cross section of the TEXTOR tokamak during the magnetic field ramp. The EC waves are injected from the low field side and focused near the centre of the plasma. Due to the magnetic field ramp the deposition region of ECCD is varied as shown over an area which includes $q = 1$ surface.

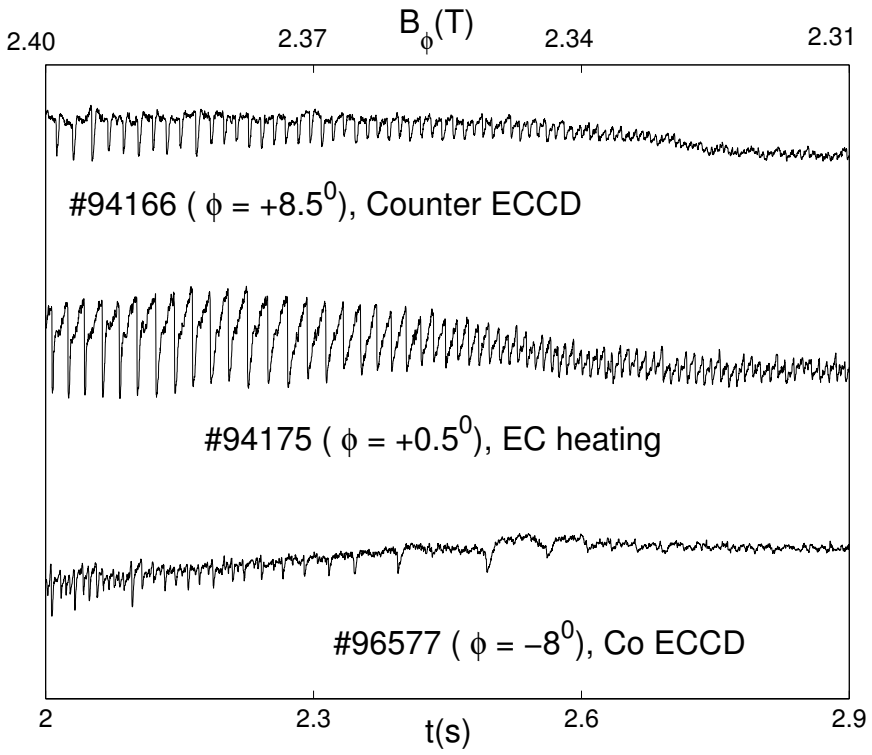

Figure 4.7: Examples of ECE (Electron Cyclotron Emission) traces during magnetic field ramp for counter-ECCD, pure EC heating and co-ECCD.

to 2.1 T in three seconds, while for the larger toroidal injection angles the magnetic field was ramped down from 2.4 T to 2.0 T. In this way for all injection angles the deposition position of ECCD was scanned from the centre of the plasma to the mid radius, including the $q = 1$ radius. For these experiments the gyrotron was operated at its nominal performance resulting for most discharges in an incident power of the injected EC waves which decays during the full 3 sec ECRH pulse from 760 kW down to 670 kW. This accounts for about 5 % losses in the transmission line. The neutral beam injection (NBI) was kept on a low level of 300 kW for diagnostic purposes. The Electron Cyclotron Emission (ECE) and Soft X-Ray (SXR) diagnostics were surveying the plasma for further sawtooth oscillation analysis (see Figure 4.7).

4.4.2 Experimental results

The ECE traces have been chosen to be the main source of the information on sawtooth crashes. Firstly, the sawtooth crashes have been identified resulting in the sawtooth period as a function of time. Secondly, the TORBEAM code [22] has been used to calculate the deposition position and amount of the noninductive current drive, based on the experimental density, temperature, magnetic field, plasma current and the actual value of the injected wave power at that time. This numerical code incorporates the beam tracing technique to calculate a noninductive current drive induced by EC waves. Since the magnetic field was swept in the experiment, the deposition position can be

Discharge #	ϕ	$I_{\mathrm{eccd}}(kA)$	W	$I_{\mathrm{eccd}}(2I_{q=1}W^2)^{-1}$	W_{eff}	$I_{\mathrm{eccd}}(2I_{q=1}W_{\mathrm{eff}}^2)^{-1}$
98105	-13^0	18	0.12	4.0	0.14	2.9
94044	-11.5^0	17	0.11	5.0	0.13	3.4
96577, 98102	-8^0	14	0.07	10.5	0.10	4.8
98103	-5^0	9	0.06	7.4	0.09	3.0
93120, 1, 3, 9	-3.5^0	5	0.05	6.1	0.09	2.1
94175	$+0.5^0$	-1	0.04	2.0	0.08	0.6
98095, 7	$+2^0$	-3	0.04	4.0	0.08	1.2
94166	$+8.5^0$	-17	0.08	7.8	0.11	4.5

Table 4.1: Results of TORBEAM calculations for discharges presented in this paper. All quantities related to ECCD are taken at the $q = 1$ surface.

represented as a function of time. Finally, these time dependant functions resulted in the sawtooth period as a function of the deposition radius $\tau_{saw}(r_{dep})$.

A large number of discharges have been performed for different toroidal injection angles ranging from -13.0^0 for co- to $+8.5^0$ for counter-current drives. All discharges are presented in Table 4.1, which provides the driven current at the $q = 1$ surface, according to TORBEAM, and the corresponding profile width. Also given in this Table is the corresponding value for the sawtooth stabilisation criterion Equation 4.3. All discharges in the data set are seen to satisfy the criterion. However, TORBEAM predictions do not include the effect of radial diffusion, which is expected to broaden some of the more narrow current density profiles. The current density profile width introduced by radial diffusion is given by $W_D \sim (D\tau_{SD})^{1/2}$, where D is a radial diffusion coefficient and τ_{SD} is the collisional slowing down time of the current carrying electrons. Since the toroidal injection angles used in most experiments are relatively small the EC power will be deposited in the bulk of the distribution function. The relevant slowing down time is then that of the thermal electrons. Together with the typical diffusion coefficient $D = 1\,\mathrm{m}^2/\mathrm{s}$, this would give a profile width due to transport equal to $W_D = 1$ cm. The profile width obtained from TORBEAM without radial diffusion can be corrected by $W_{\mathrm{eff}} = (W^2 + W_D^2)^{1/2}$. The values for W_{eff} are also given in Table 4.1. When radial diffusion is accounted for the discharge #94175 with the smallest toroidal injection angle $\phi = +0.5^0$, the driven current drops well below the requirement for efficient sawtooth control. Furthermore, it is noted that the injection angles are only known with an experimental uncertainty of the $\pm 1^0$. This identifies this discharge as one with almost pure ECRH and therefore it will be used as a reference case.

One of the difficulties to study the influence of the noninductive current drive on the sawteeth is to discriminate between the effect produced by the electron cyclotron current drive and a similar effect induced by the concurrent heating. To exclude the contribution from the heating to the change of the sawtooth period all discharges with ECCD have been compared with the reference discharge with only ECRH. The exclusion of the ECRH influence is defined as a normalisation of the $\tau_{saw}(r_{dep})$ function to the one obtained for the discharge with pure ECRH. The Figure 4.8 illustrates the choice of the fitting function used for normalisation. This assumes that the effect of the heating

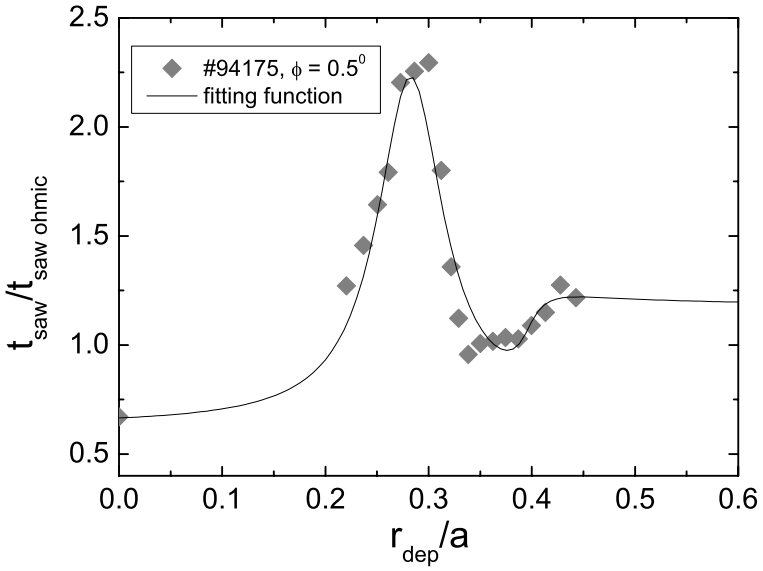

Figure 4.8: The fitting function of the sawtooth period as achieved with pure ECRH. The sawtooth period for on-axis heating was estimated by taking the average of co- and counter- ECCD cases.

in the ECCD and ECRH discharges is identical and, consequently that the temperature profiles are identical as well. To check this we have compared the ECRH only reference discharge with the discharge #94166 with counter-ECCD and found good agreement between the temperature profiles as measured with the 11 channel ECE radiometer. The Figure 4.9 compares the electron temperature profiles at two different positions of the ECRH during the magnetic field ramp in these two discharges.

The Figures 4.10a, 4.10b, 4.10c show the sawtooth period normalised to the corresponding sawtooth period for the EC heating case as a function of ECCD deposition position, $\rho_{dep} = r_{dep}/a$, for a set of discharges with co-current drive. Discharges #93120, #93121, #93123 and #93129 have the same toroidal angle of the launcher mirror, $\phi = -3.5^o$ which results in a narrow ECCD deposition profile with Gaussian width of $W \approx 0.04$ (according to the TORBEAM calculations). The #98105 discharge has rather large toroidal angle of -13^0 and therefore much wider ECCD deposition profile width $W \approx 0.12$. The $q = 1$ surface is located around $\rho = 0.3$ for all discharges. One can see clear destabilization/stabilization effect inside/outside of $q = 1$ surface, which is in agreement with the model predictions. Also, the maximum effect on the sawtooth period for the wider ECCD profile (discharge #98105) is shifted further to the right from $q = 1$ surface. A similar set of discharges with counter drive is plotted in Figures 4.11a and 4.11b. There are three shots #998095, #98097, #94166 with different toroidal injection angles of $+2^0$,$+2^0$ and $+8.5^0$, respectively. In Figure 4.11b the stabilization/destabilization effect clearly occurs when the counter-ECCD is deposited inside/outside of the $q = 1$ surface. However, for the smaller toroidal angle (see Fig-

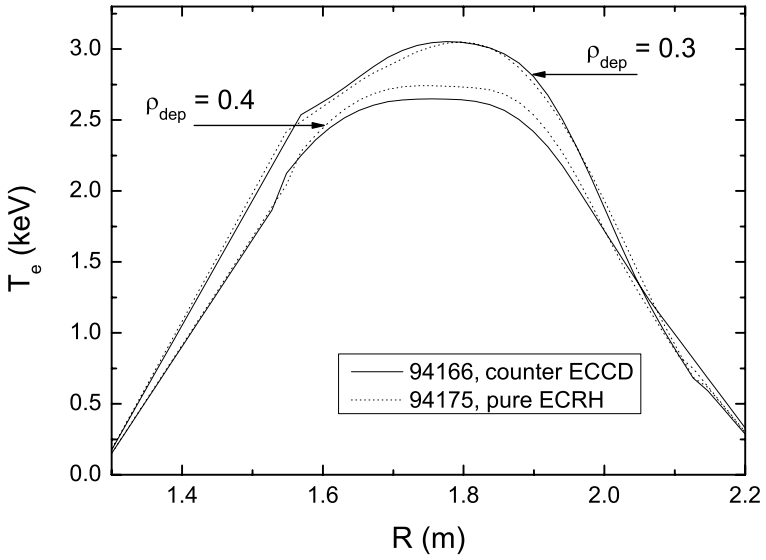

Figure 4.9: The electron temperature as a function of major radius for the pure ECRH discharge #94175 and counter-ECCD discharge #94166. The profiles correspond to the different ECRH deposition positions.

ure 4.11a) the effect of the current drive is far less distinct. Also the $q = 1$ surface may well change its position in the plasma during the magnetic field ramp, which can possible explain the relative shift towards the plasma centre of the whole curve in Figure 4.11b.

In order to perform quantitative comparison between experimental values of the sawtooth period and the shear evolution one has to provide the critical shear at which the sawtooth crash is triggered. The calculation of the critical shear at $q = 1$ is beyond the scope of the present article. However, a qualitative comparison can be realised by comparing the sawtooth period shown in Figures 4.10a, 4.10b, 4.10c, 4.11a, 4.11b to the ratio of the shear $s_1^{\text{no eccd}}(t = 20ms)/s_1^{\text{eccd}}(t = 20ms)$ at $q = 1$ obtained from our model calculations with the driven current and profile width as realised at any given time in the experiment. For each deposition radius the driven current and profile width have been calculated for the experimental conditions with the TORBEAM code neglecting radial diffusion. The solid black line in Figures 4.10 and 4.11 represents the $s_1^{\text{no eccd}}(t = 20ms)/s_1^{\text{eccd}}(t = 20ms)$ ratio calculated using the plasma and ECCD parameters for the corresponding discharge. The regions of predicted increased/decreased shear at the $q = 1$ surface correspond well to the observed lengthening/shortening of the sawtooth period. The magnitude of the shortening of the sawtooth period even corresponds reasonable well to the predicted value of $s_1^{\text{no eccd}}(t = 20ms)/s_1^{\text{eccd}}(t = 20ms)$. This is less the case for the lengthening of the sawtooth period, which can be understood from the behaviour of the shear evolution as illustrated in Figure 4.12. This Figure compares the shear evolution with co-ECCD for two deposition radii to the case

without current drive. For deposition outside $q = 1$, $x_c = 1.12$, the lengthening of the sawtooth period can depend strongly on the precise value of the critical shear. However, the present model is oversimplified and does not seem to be consistent with the observed very long sawtooth periods. The counter-current drive case with a relatively small injection angle of 2^0 shows very little effect on the sawtooth period. As can be seen in Table 4.1 this could be a consequence of the current density profile broadening by radial diffusion.

4.5 Conclusions

We have presented a simplified model of the poloidal field evolution following the sawtooth crash in the presence of localised non-inductive current drive. The simplicity of the model allowed us to scan a wide range of parameters of current drive such as amplitude and Gaussian width of the deposition profile. The equations have been solved in a dimensionless form to allow easy scaling of the solution.

Taking a factor of two change in the shear (either increasing or decreasing) as a necessary requirement for a significant change in the sawtooth period, the results of the model calculations can be summarised in terms of a required noninductive current for sawtooth period control given by

$$I_{cd} \gtrsim 2 \left(\frac{\Delta r}{r_{q=1}} \right)^2 I_{q=1}, \tag{4.4}$$

where Δr is the Gaussian width of the noninductive current profile, $r_{q=1}$ is a radius of the $q = 1$ surface and $I_{q=1}$ is the total current inside $q = 1$. The obtained requirement is well fit with the choice of the discharge with pure ECRH heating, which is below the proposed criterion, whereas other discharges are above it (see Table 4.1).

These results are in qualitative agreement with experimental observations during ECRH and ECCD on TCV [9, 12] and on TEXTOR [10, 16]. These clearly indicate the increased sawtooth period with co-ECCD just outside and with counter-ECCD just inside the $q = 1$ surface. However, in the experiments it is difficult to separate the effects of current drive from the unavoidable effects of additional heating [12]. Therefore, the sawtooth behaviour in discharges with identical heating profiles but different current drive efficiencies have been compared. By normalising the sawtooth period response as a function of deposition radius on a discharge with heating only, it has been possible to identify clearly the effects of both co- and counter- current drives. In both cases the anticipated effects of localised current drive on the sawtooth period are confirmed. Altogether the observations confirm that a critical shear value around $q = 1$ determines the moment of sawtooth crashes as predicted by theory [7]. The absolute value of the critical shear has still to be measured and is probably dependent on other variables like β, pressure gradients and collisionality.

Acknowledgment

This work, supported by the European Communities under the contract of Association between EURATOM/FOM, was carried out within the framework of the European Fusion Programme. The views and opinions expressed herein do not necessarily reflect those of the European Commission.

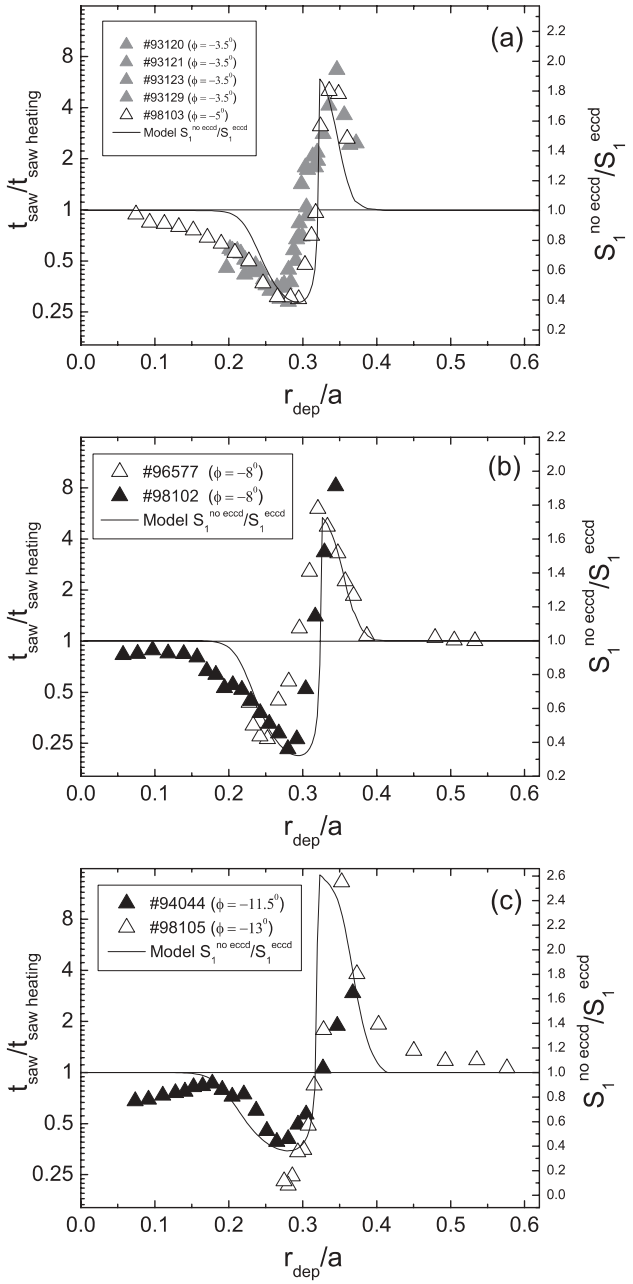

Figure 4.10: Experimental observations of the sawtooth period in presence of the co-current drive and model calculations of s_1^{noeccd}/s_1^{eccd} quantity for the experimental conditions a) The sawtooth period normalised to the corresponding value in the discharge with pure ECRH as a function of deposition position. Four discharges in this plot have the same toroidal injection angle of the ECRH launcher mirror $\phi = -3.5^0$ and one has $\phi = -5^0$. b) As in a) all discharges with $\phi = -8^0$ c) As in a) #94044 with $\phi = -11.5^0$ and #96105 with $\phi = -13^0$

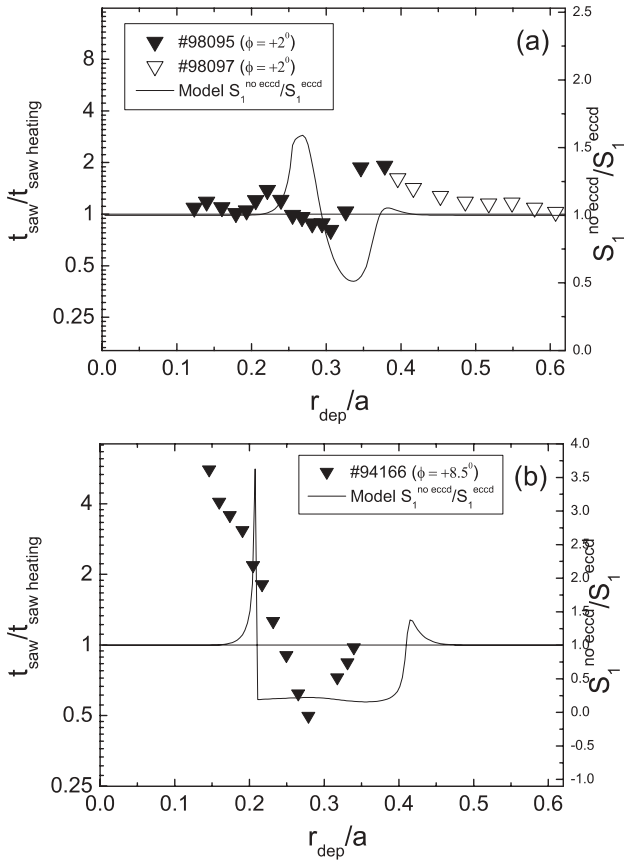

Figure 4.11: Experimental observations of the sawtooth period in presence of the counter-current drive and model calculations of s_1^{noeccd}/s_1^{eccd} quantity for the experimental conditions a) The sawtooth period normalised to the corresponding value in the discharge with pure ECRH as a function of deposition position. All discharges in this plot have the same toroidal injection angle of the ECRH launcher mirror $\phi = +2^0$ b) As in a) #94166 with $\phi = +8.5^0$

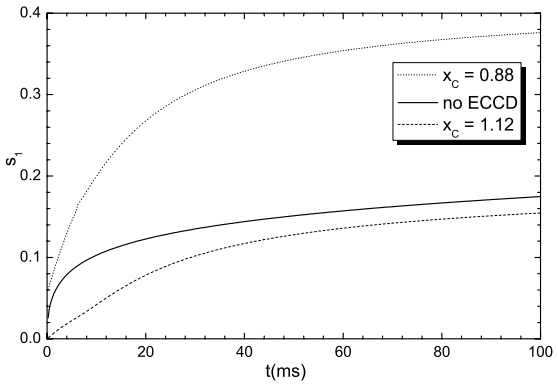

Figure 4.12: The shear at the $q = 1$ surface as a function of time calculated for the ECCD deposition inside/outside of the $q = 1$ surface and in the absence of the current drive. The plasma parameters are identical to the discharges #96577 and #98102 which have the toroidal injection angle $\phi = 8^0$.

Bibliography

[1] Hastie R 1998 *Astrophysics and Space Science*, **256** 177

[2] Sauter O *et al* 1997 *Phys. Plasmas* **4** 1654

[3] Engelmann F 1980 *Comments Plasma Phys. Controlled Fusion* **5** 261

[4] Taylor R *et al* 1980 *Comments Plasma Phys. Controlled Fusion* **13** 227

[5] Reiter D *et al* 1990 *Nuclear Fusion* **30** 2141

[6] Kadomtsev B 1975 *Sov. J. Plasma Phys.* **1** 389

[7] Porcelli F *et al* 1996 *Plasma Phys. Control. Fusion* **38** 2163

[8] Sauter O 1998 *Theory of Fusion Plasmas* 403

[9] Henderson M *et al* 2001 *Fusion Eng. Des.* **53** 241

[10] Westerhof E *et al* 2003 *Nucl. Fusion* **43** 1371

[11] Mück A 2005 *Plasma Phys. Contr. Fusion* **47** 1633

[12] Angioni C *et al* 2002 *Nucl. Fusion* **43** 455

[13] Isayama A *et al* 2001 *Fus. Eng. Des.* **53** 129

[14] Graves J P 2005 *Plasma Phys. Contr. Fusion* **47** 121

[15] Pereverzev G *et al* August 1991 *ASTRA, Report IPP 542*

[16] Westerhof E *et al* 17-20 May 2004 *Proceedings of the* 13$^{\text{th}}$ *Joint Workshop on Electron Cyclotron Emission and Electron Cyclotron Heating* Nizhny Novgorod, Russia, Ed. A. Litvak, Institute of Applied Physics RAS p. 266

[17] Soltwisch H *et al* 1986 *Plasma Phys. Contr. Nuclear Fusion Res 1986 (Vienna, IAEA)* **I** 433

[18] O'Rourke J 1991 *Plasma Phys. Contr. Fusion* **30** 1475

[19] Weller A *et al* 1987 *Phys. Rev. Lett.* **59** 2303

[20] Gill R *et al* 1992 *Nucl. Fusion* **32** 723

[21] Osborne T *et al Phys Rev. Lett.* **49** 734

[22] Poli E *et al* 2001 *Computer Physics Communication* **136** 90

Chapter 5

Fokker-Planck modelling of current penetration including Electron Cyclotron Current Drive

A Merkulov, E Westerhof, F C Schüller

FOM-Institute for Plasma Physics Rijnhuizen, Association EURATOM-FOM, Trilateral Euregio Cluster, The Netherlands, www.rijnh.nl

This paper is submitted to Plasma Physics and Controlled Fusion

Abstract.

The current penetration during electron cyclotron current drive(ECCD) on the resistive time scale is studied with a full Fokker-Planck simulation which includes a model for the magnetic diffusion that determines the parallel electric field evolution. The existence of the synergy between the inductive electric field and EC driven current complicates the process of the current penetration and invalidates the standard method of calculation in which Ohm's law is simply approximated by $j - j_{\mathrm{cd}} = \sigma E$. Here we propose to obtain at every time step a self-consistent approximation to the plasma resistivity from the Fokker-Planck code, which is then used in a concurrent calculation of the magnetic diffusion equation in order to obtain the inductive electric field at the next time step. We have performed a series of Fokker-Planck calculations including a self-consistent evolution of the inductive electric field. We have varied both the ECCD power and the electron density, thus varying the well known non-linearity parameter for ECRH $P_{\mathrm{ecrh}}[\mathrm{MW/m^{-3}}]/n_e^2[10^{19}\,\mathrm{m^{-3}}]$ (Harvey et al 1989 Phys. Rev. Lett 62 426). This parameter turns out to be also a good predictor of the synergetic effects.
The results then are compared with the standard method of calculations of the current penetration using the ASTRA transport code. At the low values of the Harvey parameter the standard method is in quantitative agreement with Fokker-Planck calculations. However, at high values of the Harvey parameter, significant amounts of non-thermal electrons are generated forming the basis for the synergetic effects.

5.1 Introduction

Present day electron cyclotron resonant heating (ECRH) and current drive (ECCD) systems are characterised by highly flexible wave launchers which can focus the wave power in well collimated Gaussian beams into the plasma [1, 2, 5, 7, 10]. This has resulted into the capability of flexible and well localised deposition of the high power electron cyclotron waves, as well as the possibility of significant non-inductive current drive [11, 12, 13, 8, 20, 14]. In recent years ECCD has become an invaluable tool in a number of major physics studies. It has been used as a tool to tailor the current density profile both during the current ramp up phase [15, 16] as well as during the current plateau phase [3] in order to improve confinement through negative central shear. The flexibility of off-axis ECCD current profile tailoring also played a major role in the achievement of fully non-inductive operation at high beta in DIII-D [17]. Furthermore, fully non-inductive plasmas have been achieved with ECCD as the only source of additional heating [4]. The precise localisation of the ECCD, finally, has been extensively utilised for the control of MHD instabilities. In particular, neoclassical tearing modes have been suppressed by ECCD in a number of experiments [18, 6, 9]. Not surprisingly then, in the next generation fusion experiments like ITER ECCD will have the major tasks of both on and off-axis current drive for steady state operation, as well as the stabilisation of neoclassical tearing modes by current drive at the $q = 3/2$ and $q = 2$ surfaces.

In most ECCD experiments only part of the current is driven by the electron cyclotron waves, and a residual loop voltage or parallel electric field stays responsible for the remaining inductive part of the current. Even in case of full non-inductive current drive, transient electric fields will play a significant role during phases of current initiation or redistribution. Comparison of the measurements of the efficiency of the ECCD with Fokker-Planck code simulations shows the existence of a significant synergy between the electron cyclotron power and the residual loop voltage [11, 19, 20]. However, these calculations refer to a steady state in which the residual loop voltage is supposed to be known. Yet, when the electron cyclotron wave power is suddenly switched on and a non-inductive current is being build up, the first response of the plasma will be to produce a backward inductive loop voltage. Given the synergy between the electron cyclotron wave and the loop voltage the behaviour of the system on this dynamic time scale can only be properly described with a full Fokker-Planck simulation including a proper model for the evolution of the inductive loop voltage [21]. In the standard method for solving the problem of penetration of the non-inductive driven current, one solves the magnetic diffusion equation by obtaining the value of the parallel electric field from the approximation to Ohm's law given by

$$\eta_{\mathrm{neo}} \left(j - j_{\mathrm{cd}} \right) = E, \tag{5.1}$$

where η_{neo} is the neoclassical resistivity for a thermal plasma. The self consistent simulation of the current penetration with a Fokker-Planck code and the comparison of these results with those obtained by the standard method is the topic of the present paper. A numerical implementation of the induction equation for the loop voltage quickly becomes unstable and is impractical. Here we propose to obtain at every time

step a self-consistent approximation to the plasma resistivity from the Fokker-Planck code, which is then used in a concurrent calculation of the magnetic diffusion equation in order to obtain the inductive electric field at the next time step.

The layout of this paper is as follows. In Section 5.2, the basic plasma model based on the bounce averaged Fokker-Planck equation is described. The Fokker-Planck equation is solved with the numerical code RELAX [22]. The details of how to obtain within the numerical code the self-consistent evolution of the loop voltage are discussed. In Section 5.3, we give the results of a number of calculations for ECCD in the TEXTOR tokamak. Both the wave power and plasma density have been varied, thus varying a well known parameter for the occurrence of nonlinearities in ECCD alone [23] $[P_{\mathrm{RF}}(\mathrm{W/cm^3})]/[n_e(10^{13}\,\mathrm{cm^{-3}})]^2 \geq 0.5$, which we call the Harvey criterion from hereon. Next these results are compared to the standard method of the calculations of the current penetration by the transport code ASTRA [24]. Finally, the conclusions are summarised in Section 5.4.

5.2 Fokker-Planck model including magnetic diffusion

In this section we present the physics model used for these numerical studies and the basic approximations. The basic equation is the bounce-averaged quasi-linear Fokker-Planck equation, which for the present study has to be supplemented with an equation for the self-consistent evolution of the parallel electric field. The equations are solved in the numerical code RELAX.

5.2.1 Bounce-averaged Fokker-Planck equation

RELAX is a quasi-linear Fokker-Planck code in toroidal geometry [22]. The physics models incorporated in the code include bounce averaged approximate collision operators, electric field driven momentum space convection, and quasi-linear diffusion due to Electron Cyclotron Resonant Heating (ECRH). The code has an interface with the ray-tracing code TORAY [25]. The magnetic equilibrium is approximated by concentric circular flux-surfaces. The RELAX code solves the bounce-averaged Fokker-Planck equation in the following form [22]:

$$\frac{\partial f_e}{\partial t} = \left\langle \sum_s C(f_e, f_s) \right\rangle - \langle \Gamma_q \rangle - \left\langle q_e \vec{E_{||}} \cdot \vec{b} \frac{\partial f_e}{\partial p_{||}} \right\rangle , \tag{5.2}$$

where f_e is the bounce-phase independent part of the electron distribution function, $\Gamma_q = \langle q_e \left(E + (\upsilon/c) \times B\right) f_e \rangle$ is the quasi-linear flux, $\vec{E_{||}}$ is the parallel electric field, $\vec{b}$ is a unit vector in the direction of the magnetic field and $C(f_e, f_s)$ is a collision operator. The bounce averaging operation $\langle ... \rangle$ is defined as

$$\langle Q \rangle = \frac{1}{\tau_B} \oint Q \frac{ds}{\upsilon \cos \vartheta}, \tag{5.3}$$

where τ_B is the bounce period and $\vartheta = \arccos(p_{||}/p)$ is the pitch angle. In RELAX the bounce averaged electron distribution function is written in terms of the momentum and pitch angle on the low field side of the flux surface: i.e. $f_e((p,\vartheta)_{\mathrm{lfs}})$.

5.2.2 The truncated collision operator

In the general case of an anisotropic distribution function the electron-electron collision operator is rather complex. Moreover, the bounce-averaging of such an operator can only be done numerically, leading to high requirements on the computing power. Therefore, the RELAX code was designed to minimise the needed computer power yet retaining the most essential physics. The calculations presented in this paper have been done by using the truncated electron-electron collision operator. It is based on the expansion of the electron distribution function about a Maxwellian distribution:

$$f_e(\vec{p}) = f_{\mathrm{em}}(p) + f_{e1}(\vec{p}), \tag{5.4}$$

where f_{em} is the relativistic Maxwellian distribution. Neglecting terms of order f_{e1}^2, the self-collision operator $C(f_e, f_e)$ is approximated by the linearised operator

$$C_{\mathrm{lin}}^{e/e}(f_e, f_e) = C\left(f_e(\vec{p}), f_{\mathrm{em}}(p)\right) + C\left(f_{\mathrm{em}}(p), f_e(\vec{p})\right). \tag{5.5}$$

To obtain a truncated version of this operator the total distribution function can be expressed as a sum of Legendre harmonics, $f_e(\vec{p}) = \Sigma_{l=0}^{\infty} f_e^l(p) P_l(\cos\vartheta)$, where $P_l(x)$ are the orthonormal set of Legendre polynomials. Please note that f_e^0 contains all particles and energy, whereas $f_e^1(p)P(\cos\vartheta)$ contains all macroscopic momentum. Hence, only the contributions from parts with $l = 0, 1$ need to be evaluated to ensure the conservation of energy, density and momentum. The truncated collision operator is defined by replacing $f_e^0(p) = f_{\mathrm{em}}(p)$ in the evaluation of the second term in Equation (5.5):

$$C_{\mathrm{trunc}}^{e/e}(f_e(\vec{p}) = C\left(f_e(\vec{p}), f_{\mathrm{em}}(p)\right) + C\left(f_{\mathrm{em}}(p), f_e^1(p)P_1(\cos\vartheta)\right). \tag{5.6}$$

The truncated collision operator no longer conserves energy, but still density and momentum. This approximation is well suited for the calculations of the current drive efficiency and resistivity. Electron-ion collisions are assumed to contribute only to pitch angle scattering and are accounted for as an effective ion charge.

The advantage of this approximated collision operator is that the bounce average is now reduced to a simple multiplication of the Fokker-Planck coefficients with some orbit integrals that can be calculated at the beginning of each run [22].

5.2.3 The EC quasi-linear diffusion operator

The detailed description of the bounce-averaged EC diffusion operator can be found in [26]. The test particle approach—which is based on the calculation of the effect of the waves on test particles averaged over all possible orbits—is employed to obtain the bounce-averaged EC wave driven quasi-linear diffusion operator. The results are

expressed in terms of the diffusion of the magnetic moment, $\mu \equiv m_e c^2/k_B T_e$,

$$D_{\mu\mu} = \frac{\pi e^2}{m_e^2 \omega} \frac{\gamma p_\perp^2}{B^2} \left|\bar{G}\right|^2 \frac{e^{-(\gamma - n\omega_c/\omega - N_{||}x_{||})/\Delta Q}}{\sqrt{\pi \Delta Q}} \frac{P_0 e^{-\int \alpha ds}}{\Pi \cos\chi} \frac{B}{2\pi \tau_B v_{||} R B_p}, \tag{5.7}$$

where $p_\perp$ is a perpendicular momentum, γ is the relativistic mass increase, ω_c is the cyclotron frequency, n is the number of the resonance, $x_{||}$ is the normalised parallel momentum, B is a magnetic field, R is a major radius, $N_{||}$ is a parallel refractive index and the rest of the variables will be discussed later. The first few factors in this expression, including the factor $\left|\bar{G}\right|^2$, are identical to the results obtained from the standard quasi-linear theory in the homogeneous field, plane wave limit as given in [28],

$$\bar{G} = \frac{n\omega_c}{v_\perp \gamma \omega} \left[v_\perp (E^+ J_{n+1} + E^- J_{n-1}) + v_{||} E_{||} J_n \right]. \tag{5.8}$$

This factor accounts for the effect of wave polarisation and has been normalised to an electric field amplitude $E = 1$, $E^\pm = E_x \pm i E_y$.

The major difference is in the total resonance broadening ΔQ, which is the combined effect of the variation of wave and particle variables both along individual particle trajectories and between the different trajectories crossing the beam:

$$\Delta Q = \tag{5.9}$$
$$\left[\frac{L_\theta \partial}{r \partial \theta}(\gamma - n\omega_c/\omega - N_{||}x_{||})\right]^2 + \left[\frac{L_\varphi \partial}{r \partial \varphi}(\gamma - n\omega_c/\omega - N_{||}x_{||})\right]^2 + \frac{\gamma^2 R^2 \dot{\varphi}^2}{\omega L_\varphi^2}.$$

where $R\dot{\varphi}$ is the toroidal velocity, L_φ and L_θ are the beam widthes in toroidal and poloidal directions, respectively. The first two terms in brackets can be obtained from a bounce-averaging of the local delta function resonance and only the last term describes the resonance broadening due to the finite wave-particle interaction time during a beam crossing.

The term $P_0 e^{-\int \alpha ds}$ represents the total wave power crossing the flux surface weighted by the factor $1/\Pi \cos\chi$, where Π is the power flux for a normalised electric field vector and $\cos\chi$ is the cosine of the angle between the direction of wave propagation and the normal of the flux surface. The total injected power is P_0 and the factor $e^{-\int \alpha ds}$, where α is the absorbtion coefficient, represents the power absorbed along the beam trajectory s.

The last term, $B/(2\pi \tau_B v_{||} R B_p)$, is a division by the effective flux surface area. In the limit of constant B over a flux surface this term becomes exactly equal to the flux surface area. This is easily verified by substituting $\tau_B = 2\pi q R_{\text{axis}}/v_{||}$ and $q = rB/RB_p$.

5.2.4 Self-consistent electric field

As described in [21] the Fokker-Planck model itself does not take into account changes in the parallel electric field. They are caused by the changes in the current density, which are in turn introduced by the EC waves. Also the electrical conductivity may change due to the generation of energetic electrons and, consequently, it becomes

impossible to obtain the electric field from a modified Ohm's. The most obvious approach is to introduce an additional Maxwell's equation for the electromagnetic field, for example, the loop voltage at the given flux surface is determined from Faraday's law:

$$V_{\text{loop}}(r,t) = -\frac{\partial}{\partial t}\int \vec{B}\cdot d\vec{S}, \tag{5.10}$$

where the magnetic flux from the right hand side consists of externally generated field from the primary circuit as well as contributions from the changes in the plasma current distribution. Using the cylindrical approximation, neglecting the displacement current and keeping the total plasma current constant, one obtains

$$V_{\text{loop}}(r,t) = V_{\text{ext}}(r,t) - \mu_0 R_0 \int_0^a \frac{\partial I(r',t)}{r'\partial t} dr', \tag{5.11}$$

where $V_{\text{ext}}(r,t)$ is a loop voltage over the last closed flux surface, $I(r',t)$ is the plasma current contained inside r', and R_0, a are the major and minor tokamak radii, respectively. The straightforward discretization of this equation shows that the loop voltage is dependent on the time derivative of the plasma current inside r', which uses the information from the previous time step:

$$\frac{\partial I(r',t_{n+1})}{\partial t} = \frac{I(r',t_{n+1}) - I(r',t_n)}{\delta t}. \tag{5.12}$$

It has been reported [27] that this method is numerically unstable when the inductance of the system is above a certain threshold, which is true for most tokamaks. Therefore, we propose a new approach of calculating the changes in the electric field in this paper.

Our approach is based on a concurrent solution of the Fokker-Planck and the magnetic diffusion equation

$$\frac{\partial \vec{B}(r,t)}{\partial t} = \nabla \times \left(\eta \nabla \times \vec{B}(r,t)\right). \tag{5.13}$$

These equations are coupled through the resistivity and the parallel electric field. Each time step the resistivity is calculated and both the distribution function and the magnetic field are stepped forward in time. Based on the old resistivity and the new magnetic field a new value for the parallel electric field can be calculated (see below), which is then used in the next time step of the calculation. The main problem lies in the calculation of the plasma resistivity. We chose to approximate the resistivity simply as the ratio of the parallel electric field and the total current density, i.e. including any non-inductive contributions

$$\eta(r,t) = \frac{E_{||}(r,t)}{j(r,t)}. \tag{5.14}$$

This approximation becomes invalid when the driven current density is much larger then the inductive current density, $j_{\text{cd}} \gg j_{\Omega}$. In this way we introduce a magnetic field evolution, which is not only consistent with the plasma described by the Fokker-Planck equation, but also provides the necessary feedback on the changes in the electric field. To illustrate this, let us rewrite the Equation (5.13) for the poloidal magnetic field in the cylindrical approximation

$$\frac{\partial B_\theta(r,t)}{\partial t} = \frac{\partial}{\partial r}\frac{\eta(r,t)}{\mu_0 r}\frac{\partial}{\partial r}\left(rB_\theta(r,t)\right). \tag{5.15}$$

This simple approach is chosen for easy implementation yet being able to provide physical results. The evolution of the poloidal magnetic field requires an initial condition, which is calculated from the plasma current density based on the momentum distribution.

$$B_\theta(r,t_0) = \frac{\mu_0}{r}\int_0^r r\left\langle j(r,\theta,t_0)\right\rangle dr = \frac{\mu_0}{r}\int_0^r r j(r,t_0)_{\mathrm{lfs}}\frac{R_0+r}{R_0}dr, \tag{5.16}$$

where $\left\langle j(r,\theta,t_0)\right\rangle$ is the flux-surface averaged current density. The factor $R_0/(R_0+r)$ appears after matching the flux-surface averaged current density, to the plasma current density, which is taken at the low field side in the RELAX code.

Let us go through one time step of the calculation to describe the presented algorithm. The poloidal magnetic field at the time t_n is calculated using the information of the momentum distribution function at this time step:

$$B_\theta(r,t_{n+1}) = B_\theta(r,t_n) + \Delta t\frac{\partial}{\partial r}\frac{\eta(r,t_n)}{\mu_0 r}\frac{\partial}{\partial r}\left(rB_\theta(r,t_n)\right), \tag{5.17}$$

where $\eta(r,t_n) = E_{||}(r,t_n)/j(r,t_n)$ is the plasma resistivity at the time t_n. The next logical step is to evaluate how much the electric field has been changed due to the evolution of the poloidal magnetic field:

$$\begin{aligned} E_{||}(r,t_{n+1})_{\mathrm{lfs}} &= \eta(r,t_n)j(r,t_{n+1})_{\mathrm{lfs}} = \eta(r,t_n) < j(r,t_{n+1}) > \frac{R_0}{R_0+r} \\ &= \frac{\eta(r,t_n)}{\mu_0 r}\frac{\partial}{\partial r}\left(rB_\theta(r,t_{n+1})\right)\frac{R_0}{R_0+r}. \end{aligned} \tag{5.18}$$

Here the factor $R_0/(R_0+r)$ appears because the flux-surface averaged quantities on the right hand side must be corrected into low field side coordinates for input into the RELAX code. In steady state the electric field profile will be proportional to $1/R$, which corresponds to a constant loop voltage in toroidal devices. The obtained electric field $E_{||}(r,t_{n+1})_{\mathrm{lfs}}$ is then passed further to the RELAX code closing the feedback loop between the magnetic diffusion and the momentum distribution calculations. At the end of every time step a consistency check is performed to ensure that the current density profile represented by the magnetic diffusion equation has remained identical to the current density profile represented by the Fokker-Planck equation. In the calculations the profiles from magnetic diffusion equation are identical to the Fokker-Planck current density profile all the way throughout the run.

5.3 Results

This section contains results obtained with the Fokker-Planck model, which includes self-consistent calculations of the electric field. The plasma conditions cover several

possible densities as well as different levels of the injected EC power. The obtained results are then compared with the output of a transport code which includes non-inductive current drive.

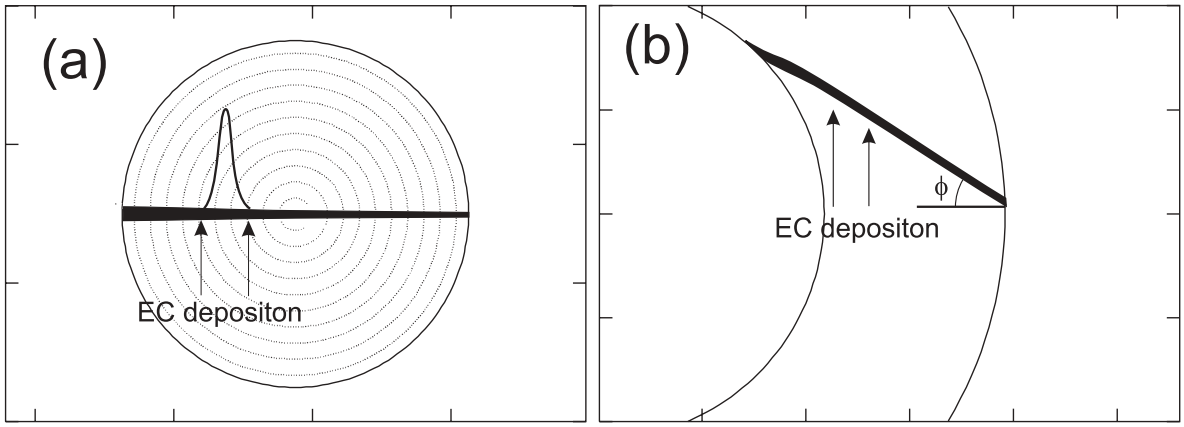

Figure 5.1: The results of the ray-tracing code TORAY show the trajectories of EC waves in plasma and the absorbtion region for a) poloidal and b) toroidal cross sections. The toroidal magnetic field $B_t = 2.12$ T.

5.3.1 Initial profiles

The target plasma was chosen to be identical to typical TEXTOR tokamak parameters, namely, the major radius $R_0 = 1.75$ m and the minor radius $a = 0.46$ m. The additional heating in our model is provided by ECRH delivering up to 2 MW at 140 GHz X-mode. The density and the injected EC power scans have been performed to address the importance of the synergy between EC waves and the ohmic current. The plasma density profile was set to a parabolical shape $n_e(r) = n_e(0)\,(1-(r/a)^2)$, where the central density $n_e(0)$ was assigned three different values: $1.4 \cdot 10^{19}$, $2.0 \cdot 10^{19}$ and $3.0 \cdot 10^{19}\,\mathrm{m}^{-3}$. The injected EC power also had three different levels of 0.5, 1.0 and 2.0 MW, for co- and counter-ECCD. This results in a total of 18 test cases. The bulk plasma temperature profile was fixed at $T_e(r) = T_e(0)\,(1-(r/a)^2)^2$, with a central temperature $T_e(0) = 2$ keV and $Z_{\mathrm{eff}} = 2$. The necessary ray tracing calculations were performed for the toroidal injection angles $\phi = -30^0$ and $\phi = +30^0$, for co- and counter-ECCD, respectively. The configuration of the EC wave launch position and absorbtion regions in the plasma are schematically plotted in Figure 5.1. The toroidal magnetic field was kept at $B_t = 2.12$ T and $B_t = 2.20$ T, which corresponds to the off- and on- axis depositions, at $\rho \equiv r/a = 0.34$ and $\rho = 0.18$, respectively. The values of the driven current obtained with the RELAX code calculations in absence of an electric field are collected in Table 5.1. Such wide variation of the density and injected EC power allow us to study situations with different fractions of ECCD compared to the total plasma current, which was set at $I_p = 320$ kA.

I_{eccd}, off axis	$n_e = 1.4 \cdot 10^{19}\,m^{-3}$	$n_e = 2.0 \cdot 10^{19}\,m^{-3}$	$n_e = 3.0 \cdot 10^{19}\,m^{-3}$
$P_{RF} = 0.5$ MW	15 kA	13 kA	10 kA
$P_{RF} = 1.0$ MW	29 kA	25 kA	20 kA
$P_{RF} = 2.0$ MW	57 kA	48 kA	37 kA

I_{eccd}, on axis	$n_e = 1.4 \cdot 10^{19}\,m^{-3}$	$n_e = 2.0 \cdot 10^{19}\,m^{-3}$	$n_e = 3.0 \cdot 10^{19}\,m^{-3}$
$P_{RF} = 0.5$ MW	22 kA	18 kA	14 kA
$P_{RF} = 1.0$ MW	47 kA	38 kA	29 kA
$P_{RF} = 2.0$ MW	98 kA	80 kA	60 kA

Table 5.1: Results of Fokker-Planck calculations in the absence of an electric field for the off- and on- axis depositions and different densities and levels of EC power.

5.3.2 Off axis deposition.

Firstly, we consider the off-axis deposition with a toroidal magnetic field of $B_t = 2.12$ T. Before calculating the current penetration let us estimate the amount of the nonlinear behaviour of the ECCD by using the non-linearity criterion which has been derived by Harvey [23]. This criterion is based on the injected power per volume and indicates the non-linear behaviour of the current drive efficiency when fulfilled:

$$\frac{P_{RF}(W/cm^3)}{[n_e(10^{13}cm^{-3})]^2} \geq 0.5, \tag{5.19}$$

where P_{RF} is the absorbed RF power averaged over the flux shell and n_e is the electron density. The calculated criterion as a function of minor radius is plotted in Figure 5.2. There is one curve for each density and injected power value, since there is almost no difference in the power absorbtion between co- and counter- deposition. The case with the lowest EC power of 0.5 MW and the highest density of $3.0 \cdot 10^{19}\,m^{-3}$ has the lowest value of the non-linearity criterion and can be considered as a benchmark for our method against transport code calculations which include non-inductive current.

The Fokker-Planck code with the self-consistent electric field was used to calculate the first 300 ms of the current penetration after the switch on of the EC power. The current penetration was also calculated with the transport code ASTRA using the non inductive ECCD profiles obtained from the Fokker-Planck model in the absence of the electric field (see Table 5.1). The loop voltage profiles from both methods were then compared at different time steps. The case with high density $n_e = 3.0 \cdot 10^{19}\,m^{-3}$ and low level of injected EC power $P_{RF} = 0.5$ MW produces almost identical results when comparing ASTRA and Fokker-Planck calculations (see Figure 5.3). However, the difference in the current penetration becomes noticeable with increasing injected EC power and decreasing electron density. Figure 5.4 compares the loop voltage for a relatively low density $n_e = 1.4 \cdot 10^{19}\,m^{-3}$ and high level of EC power, $P_{RF} = 2$ MW, as a function of radius between RELAX and ASTRA calculations for the different time points. It is clear that the current penetration is slowed down in the presence of co-ECCD. Also note, that the amount of ECCD in counter direction is less than in co-

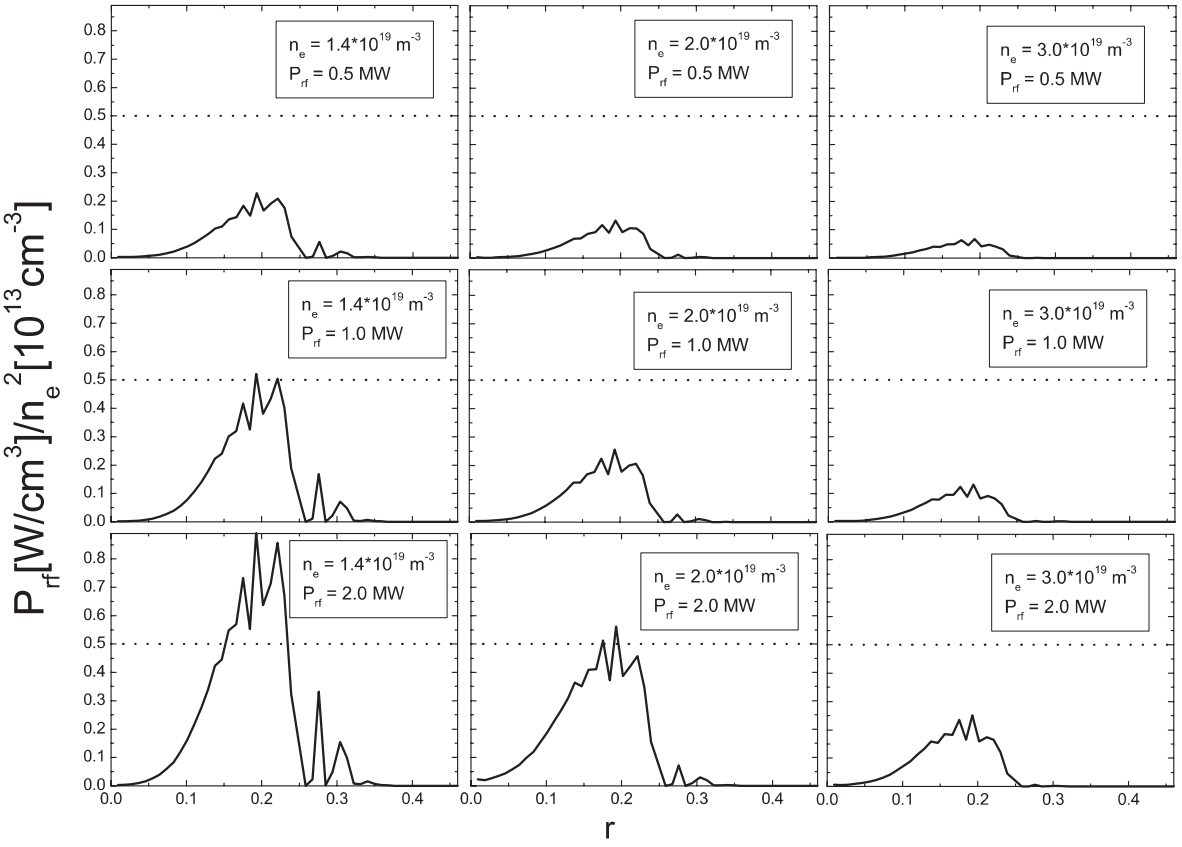

Figure 5.2: The non linearity criterion after Harvey as a function of minor radius for the off-axis deposition and different plasma densities and injected power levels, B_t = 2.12 T.

direction, since the perturbation of the loop voltage profile is smaller in the counter-ECCD case.

The following quantity is computed as a function of time to evaluate the difference between the standard approach implemented in the ASTRA code and the Fokker - Planck model with a self-consistent electric field :

$$\delta(t) = \frac{\sqrt{\sum_i \left(V_{\text{loop}}(r_i,t) - \langle V_{\text{loop}}\rangle_{r_i}(t)\right)^2}}{\langle V_{\text{loop}}\rangle_{r_i}(t)}, \tag{5.20}$$

where the index i denotes the flux surfaces and $\langle V_{\text{loop}}\rangle_{r_i}(t)$ is the loop voltage averaged over all radii at a given time. This quantity, $\delta(t)$, reflects the deviation of the loop voltage from the flat profile reached in steady state. The evolution of $\delta(t)$ gives the speed of the current penetration during ECCD. Figure 5.5 shows the evolution of $\delta(t)$ during off-axis deposition, where solid lines and diamond symbols represent ASTRA and Fokker-Planck results, respectively. The cases which satisfy the non-linearity criterion (5.19) show a difference in the evolution of $\delta(t)$ in the presence of co- and counter-current drives. For three different plasma conditions out of the calculated nine the current penetration in the presence of the co-current drive is noticeably slower than in the presence of identical counter-current drive. The explanation is the presence

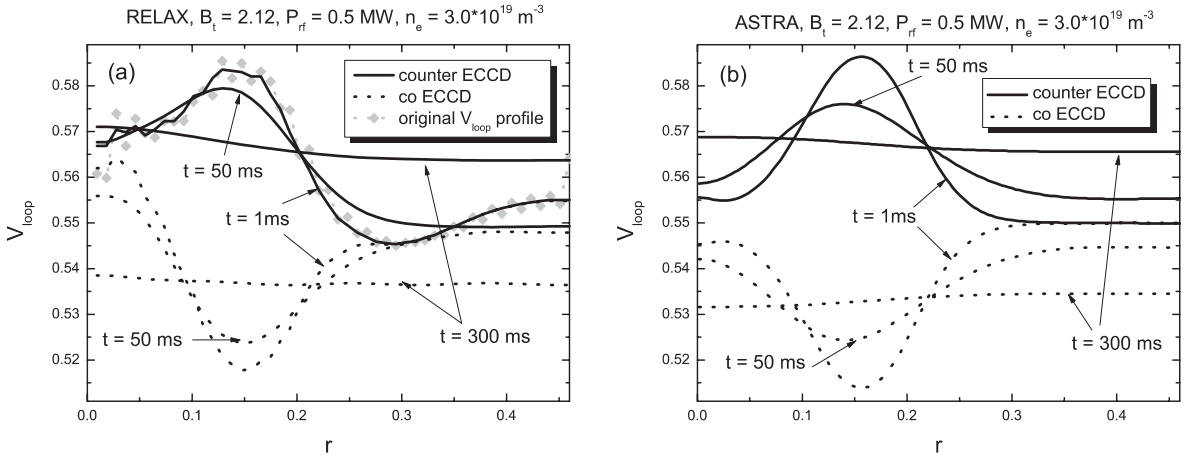

Figure 5.3: Loop voltage as a function of minor radius for the different times a) as calculated with RELAX code including the self-consistent electric field evolution (the gray diamonds show the original, not smoothed loop voltage profile), b) as calculated with the ASTRA transport code. The injected power in both cases is 0.5 MW and the plasma density $n_e = 3.0 \cdot 10^{19}$ m^{-3}, i.e. at a low value of the Harvey criterion.

of a substantial suprathermal electron population which locally leads to an increase of the plasma conductivity. Figure 5.6 plots the effective electron temperature which includes first order correction for relativistic effects

$$T_{\text{eff}} = \frac{2}{3} < E > -\frac{5}{9}\frac{< E >^2}{m_e c^2}, \tag{5.21}$$

where $< E >$ is the average energy at the given flux surface. When compared to the bulk temperature, which is constant during the calculations, the effective temperature reflects the magnitude of the suprathermal population. The cases with co-ECCD, which satisfy the non linearity criterion (5.19), also indicate the presence of a large non thermal population. In contrast, the effective temperature of the counter-ECCD cases shows a negligible deviation from the bulk temperature (see Figure 5.6).

5.3.3 Near axis deposition.

The near-axis deposition is a computationally more challenging situation, since the generated EC driven current densities are large and deposited closer to the plasma centre. Figure 5.7 shows the non-linearity criterion after Harvey for different densities and EC power levels. There are three cases when this criterion is fulfilled as for off-axis deposition. However, this time the deposition position is closer to the plasma centre. The Fokker Planck code, with self consistent calculations of the electric field, calculated the first 300 ms of the current penetration after the switch-on of the EC power. The effective electron temperature at each flux surface is plotted in Figure 5.8. It is clear that for the higher powers the present model cannot adequately describe on- and near-axis co-current drives, since the effective temperature at many surfaces is much larger than the plasma bulk temperature, which invalidates the use of the truncated collision

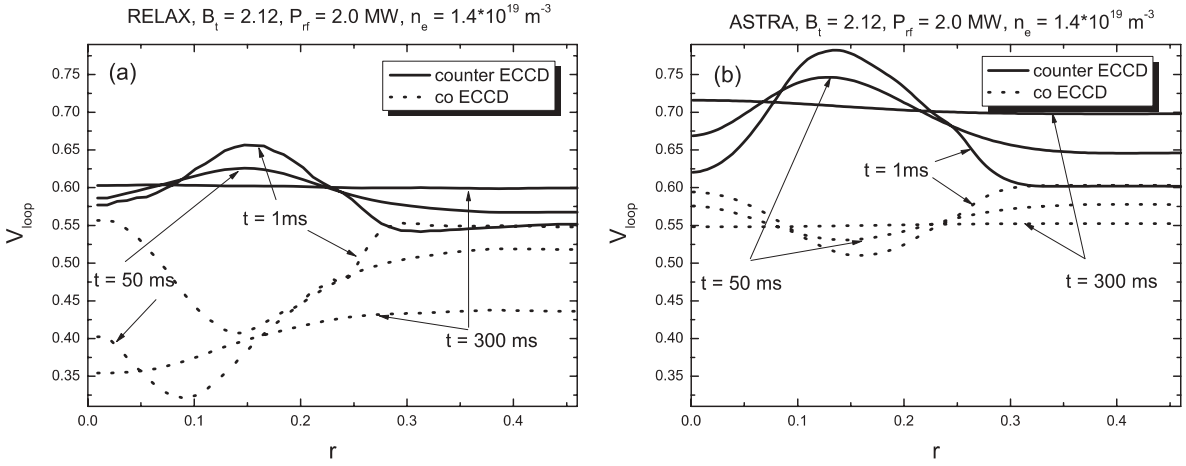

Figure 5.4: Loop voltage as function of minor radius for the different times a) as calculated with RELAX code including self-consistent electric field evolution, b) as calculated with ASTRA transport code. The injected power in both cases is 2.0 MW and the plasma density $n_e = 1.4 \cdot 10^{19}\,\mathrm{m}^{-3}$, i.e. above the Harvey criterion.

operator. The cases where the truncated collision operator becomes invalid for the co-ECCD are marked with exclamation marks in Figure 5.8.

Figure 5.9a shows the loop voltage as a function of minor radius for several time values as calculated by the Fokker-Planck code. They are than compared to the loop voltage profiles shown in Figure 5.9b, which are taken from ASTRA calculations for the same plasma conditions. The synergy between the co-ECCD and the parallel electric field leads to such a strong generation of suprathermal electrons, that the approximation of the collision operator in the Fokker-Planck model becomes invalid in a number of cases. This however does not apply to most of the counter-ECCD cases where the production of suprathermal electrons is much lower. In addition the net current generated with counter-ECCD is strongly reduced by the synergy with the parallel electric field. The generated net current is given by $I_{\mathrm{net}} = I_{\mathrm{tot}} \cdot \Delta V_{\mathrm{loop}}/V_{\mathrm{loop}}(a, t = 0)$ (see Table 5.2), where $\Delta V_{\mathrm{loop}} = V_{\mathrm{loop}}(a, t = 0) - V_{\mathrm{loop}}(a, t = 300\,\mathrm{ms})$ is the difference between initial and the final loop voltage at the plasma edge. Please note that even after 300 ms the current penetration is not complete and a full steady state is not yet reached. Therefore even for the ASTRA cases, the amounts of the net current in Table 5.2 are lower than the injected ECCD which is given in Table 5.1. The effect of a reduced counter-ECCD is absent for the case with the high density, $n_e = 3.0 \cdot 10^{19}\,\mathrm{m}^{-3}$, and low injected power, $P_{\mathrm{RF}} = 0.5$ MW and is at its maximum for the low density, $n_e = 1.4 \cdot 10^{19}\,\mathrm{m}^{-3}$, and high injected power $P_{\mathrm{RF}} = 2.0$ MW.

5.4 Conclusions

A Fokker-Planck model with self-consistent calculation of the electric field has been derived and presented. Typical plasma scenarios with off- and near- axis EC current drive for various plasma densities and EC power levels have been modelled. Finally,

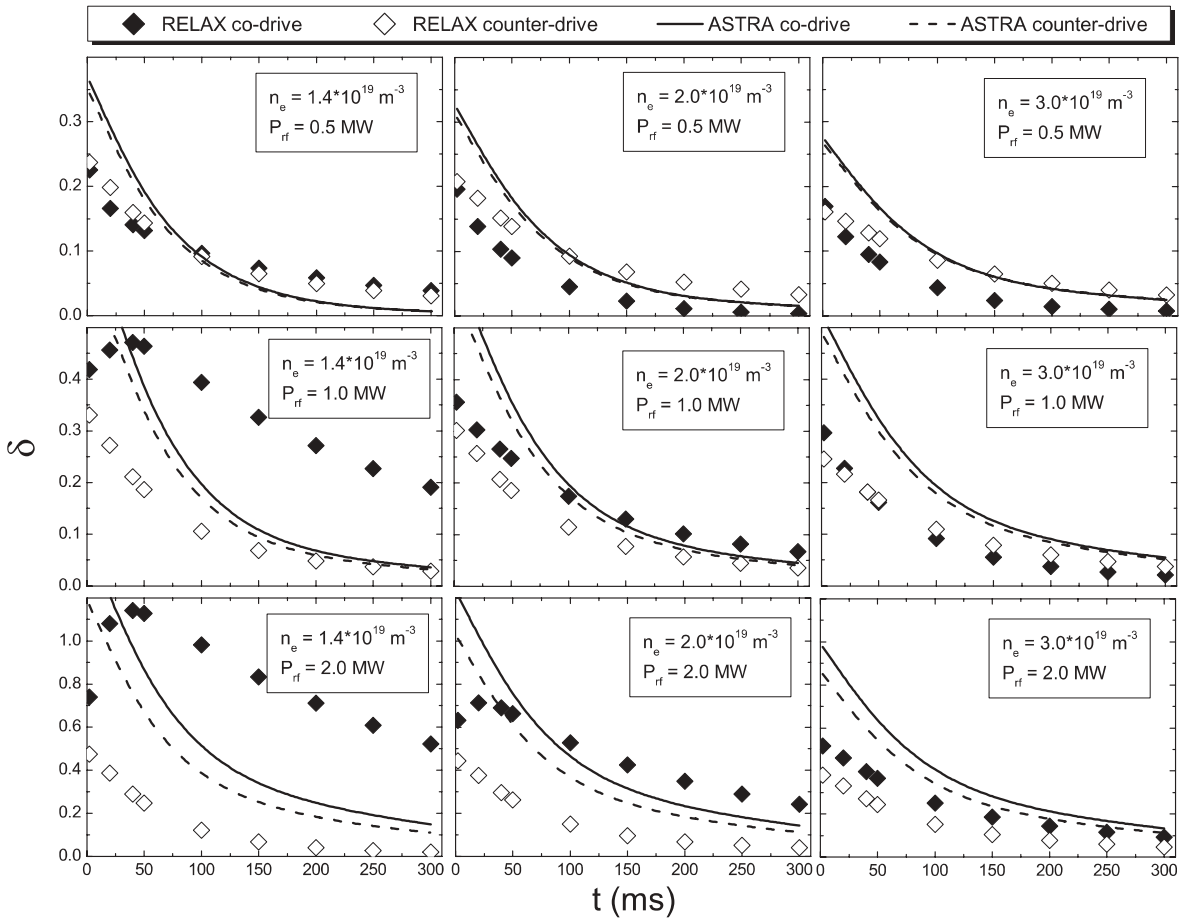

Figure 5.5: The quantity δ as a function of time for different densities and levels of injected EC power during the off-axis deposition. The solid lines represent ASTRA calculations and diamond symbols correspond to the Fokker-Planck calculations including the self-consistent electric field.

the results have been compared with the standard method of current diffusion calculations.

It is found that the non linearity criterion after Harvey for the injected RF power $[P_{\mathrm{RF}}(\mathrm{W/cm^3})]/[n_e(10^{13}\ \mathrm{cm^{-3}})]^2 \geq 0.5$ [23] can also be used to identify situations, where the synergy between EC driven and ohmic currents starts to play a role. The presence of synergy effects has been identified by comparing Fokker-Planck current penetration simulations for the co- and counter-current drive cases with calculations according to the standard method performed by the ASTRA code. For those cases where the power is well below the threshold for non-linear effects, there is reasonable agreement between the Fokker-Planck and ASTRA calculations. When the non-linearity criterion after Harvey is approached or exceeded, significant synergetic effects between the ECCD and the parallel electric field are predicted by the Fokker-Planck calculations.

The synergy between co-ECCD and the parallel electric field shows itself by a strong increase in the suprathermal electron population accompanied by a significant slowing down of the current penetration. The latter can be understood as due to the increase

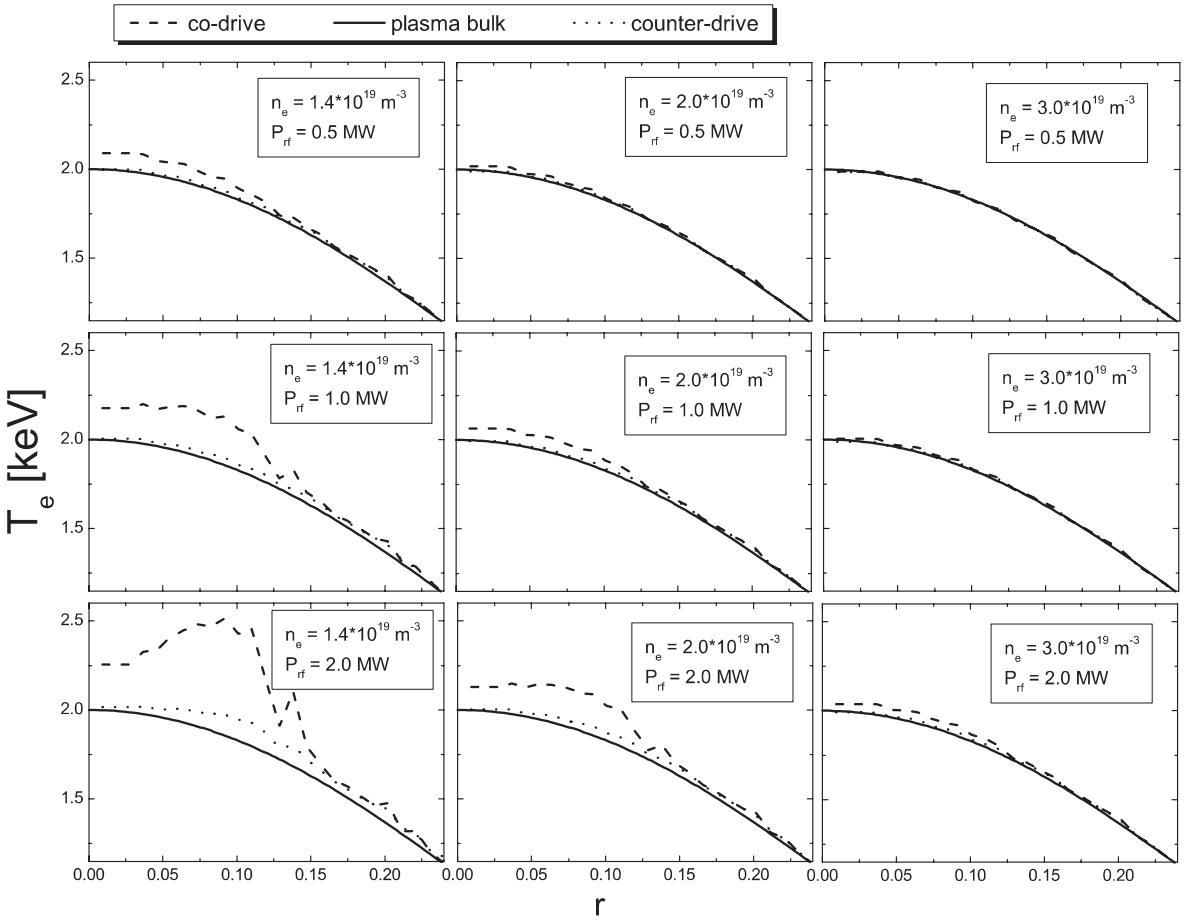

Figure 5.6: The effective temperature on the flux surface as a function of radius for the off-axis deposition ($B_t = 2.12$ T). The bold solid line corresponds to the bulk plasma temperature with $T_e(0) = 2$ keV. The dash and dot lines are for the co- and counter-injections, respectively. The effective temperature at the flux surface is proportional to the number of generated supra-thermal electrons on this surface.

in the electrical conductivity as a consequence of the large population of suprathermal electrons. In the cases of near-axis current drive, the synergy even leads to the generation of such a large population of suprathermal electrons that the approximation of the truncated collision operator becomes invalid.

In the case of counter-ECCD, the synergy with the parallel electric field leads to a decrease of the total driven current. The predicted generation of non-thermal electrons during counter-ECCD is significantly smaller than during co-ECCD.

Application of these findings for ECCD in ITER one can expect that the standard model is sufficient since the Harvey criterion will be very low and therefore synergy between the parallel electric field and the effect of the microwave field will be practically zero. However, in present-day tokamaks the synergy can be pronounced, thereby, delaying the current penetration more than predicted by the standard model.

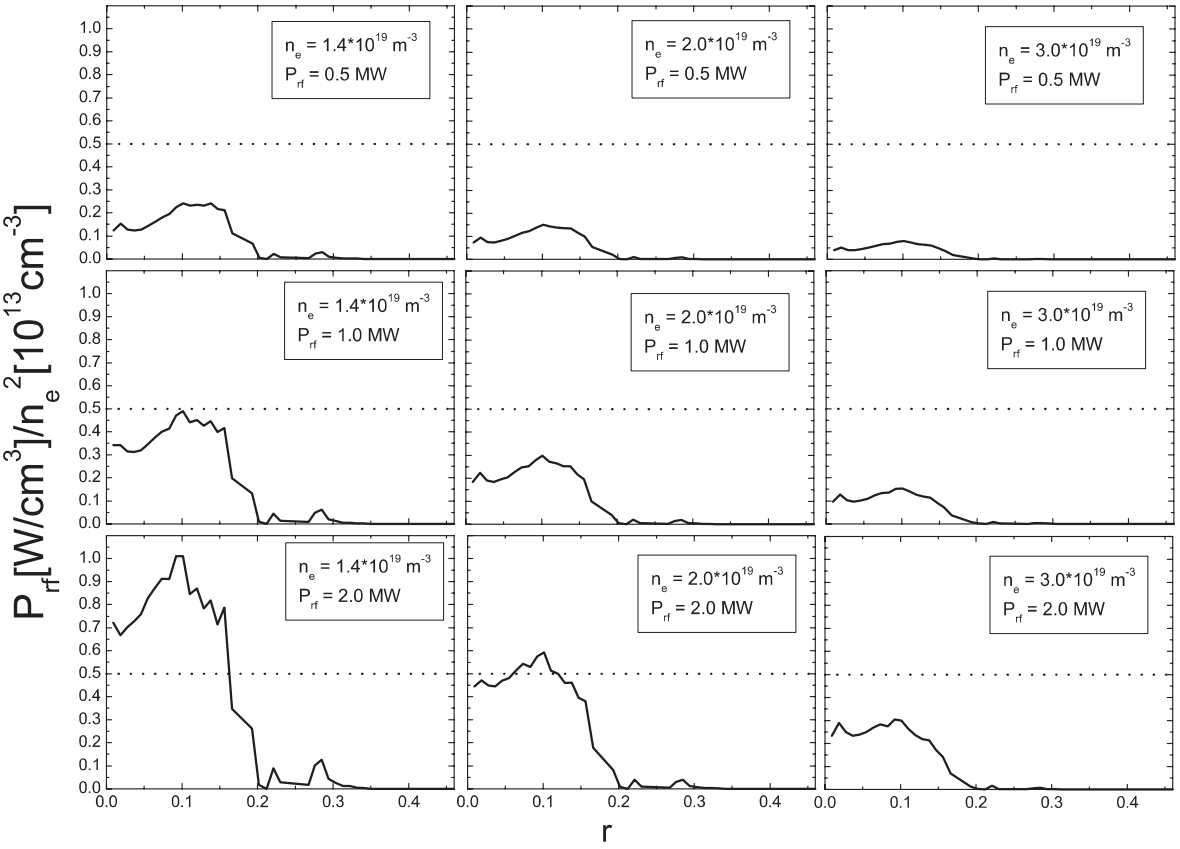

Figure 5.7: The non linearity criterion after Harvey as a function of minor radius for off-axis deposition and different plasma densities and injected power levels, $B_t = 2.20$ T.

Acknowledgment

This work, supported by the European Communities under the contract of Association between EURATOM/FOM, was carried out within the framework of the European Fusion Programme. The views and opinions expressed herein do not necessarily reflect those of the European Commission.

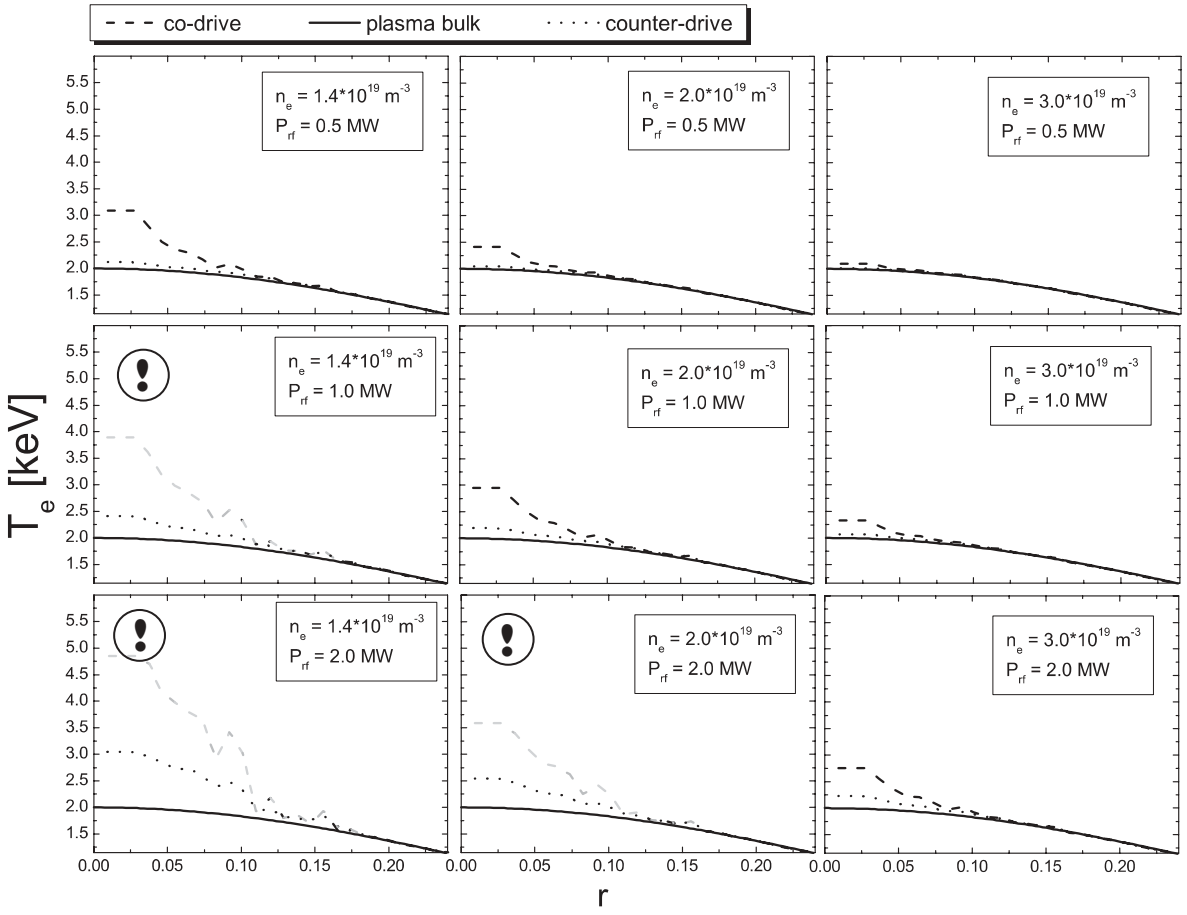

Figure 5.8: The effective temperature on the flux surface as a function of radius for the near-axis deposition ($B_t = 2.20$ T). The bold solid line corresponds to the bulk plasma temperature with $T_e(0) = 2$ keV. The dashed and dot lines are for the co- and counter-injections, respectively. The difference between the bulk and effective temperatures at the flux surface is proportional to the number of generated supra-thermal electrons on this surface. The cases where for the co-ECCD the truncated collisional operator approximation becomes invalid are marked with an exclamation mark.

$I_{\text{net}}(kA)$	$n_e = 1.4 \cdot 10^{19} m^{-3}$		$n_e = 2.0 \cdot 10^{19} m^{-3}$		$n_e = 3.0 \cdot 10^{19} m^{-3}$	
	RELAX	ASTRA	RELAX	ASTRA	RELAX	ASTRA
$P_{\text{RF}} = 0.5$ MW	-13	-15	-10	-12	-8	-8
$P_{\text{RF}} = 1.0$ MW	-17	-30	-15	-24	-11	-16
$P_{\text{RF}} = 2.0$ MW	-25	-62	-23	-47	-17	-32

Table 5.2: The comparison between Fokker-Planck (FP) and ASTRA calculations for the near-axis counter-ECCD. The generated net current is calculated at the end of the simulations, $t = 300$ ms, and based on a difference in the edge loop voltage with and without current drive.

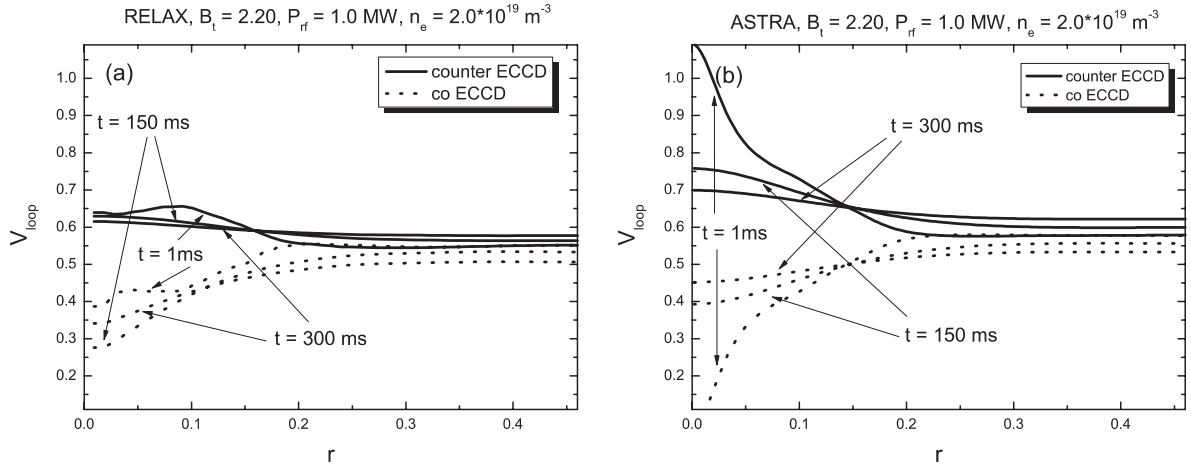

Figure 5.9: Loop voltage as function of minor radius for near-axis deposition and different times a) as calculated with RELAX code including self-consistent electric field evolution, b) as calculated with ASTRA transport code. The injected power in both cases is 1.0 MW and the plasma density $n_e = 2.0 \cdot 10^{19}\,\mathrm{m}^{-3}$

Bibliography

[1] T.P. Goodman et al., in Proc. 19th SOFT Lisbon, Vol. 1 pp. 565-568 (1996).

[2] F. Leuterer et al., Nucl. fusion **43** 1329-1342 (2003).

[3] Pietrzyk Z A *et al* 2001 *Phys. Rev. Lett* **86** 1530-1533

[4] Sauter O *et al* 2000 *Phys. Rev. Lett* **84** 3322-3325

[5] Callis R W *et al.* 2003 *Nuclear Fusion* **43** 1501-1504

[6] Petty CC *et al.* 2004 *Nuclear Fusion* **44** 243-251

[7] Ikeda Y *et al* 2001 *Fusion Engineering and Design* **53** 351-363

[8] Suzuki T *et al* 2002 *Plasma Phys. Control. Fusion* **44** 1-9

[9] Isayama A *et al.* 2000 *Plasma Phys. Control. Fusion* **42** L37-45

[10] Westerhof E *et al* 2001 *Nuclear Fusion* **41** 761-768

[11] James R A *et al* 1992 *Phys. Rev. A* **88** 8783

[12] Erckmann V *et al* 2003 *Nuclear Fusion* **43** 1313-1323

[13] Alikaev V V *et al* 1992 *Nuclear Fusion* **32** 1811-1821

[14] Prater R *et al* 2004 *Physics of Plasmas* **11(5)** 2349-2376

[15] Günter S *et al* 2000 *Phys. Rev. Lett* **84** 3097-3100

[16] Rimini F G *et al* 2005 *Plasma Phys. Control. Fusion* **47** 869-884

[17] Murakami M *et al* 2005 *Nuclear Fusion* **45** 1419-1426

[18] Gantenbein G *et al* 2000 *Phys. Rev. Lett* **85** 1242-1245

[19] Westerhof E *et al* 2001 *Fusion Engineering and Design* **53** 259266

[20] Petty C C *et al* 2002 *Nuclear Fusion* **42** 1366-1375

[21] Westerhof E 17-20 May 2004 Open Questions In Electron Cyclotron Wave Theory, *EC13 Joint Workshop on Electron Cyclotron Emission and Electron Cyclotron Resonance Heating*, Nizhny Novgorod, Russia

[22] Westerhof E *et al* 1992 *Rijnhuizen Report* RR 92-211

[23] Harvey R W *et al* 1989 *Phys. Rev. Lett.* **62** 426-429

[24] Pereverzev G *et al* August 1991 *ASTRA, Report IPP 542*

[25] Kritz A H *et al* 22-26 March 1982 *Proc.* 3^{rd} *Intern. Symposium on Heating in Toroidal Plasmas* **II** 707

[26] Peeters A G *et al* 1995 *Plasma Phys. Control. Fusion* **37** 525-540

[27] Eriksson L -G, Helander P 2003 *Computer Physics Communications* **154** 175-196

[28] Giruzzi G 1988 *Phys. Fluids* **31** 3305

Chapter 6

Modelling of the current ramp-up in TEXTOR

6.1 Introduction

The plasma current ramp-up phase is an important part of the plasma scenario that determines the flat-top phase of the subsequent plasma discharge. Moreover, a slow and instabilities-free current ramp is a necessary element of the discharge scenario to meet the requirements of an advanced tokamak like ITER [1]. The tailoring of the current profile during this phase, by means of additional heating, has been successfully realised in Tore-Supra [2], Asdex-Upgrade [3], DIII-D [5] and other tokamaks. However, the numerical modelling and interpretation of the current ramp-up phase is usually complicated by the presence of significant MHD activity, which has no proper theoretical description.

This chapter is focused on the interpretation of various TEXTOR discharges—with additional heating during the current ramp phase—with the help of the ASTRA [6] transport code. These calculations are validated against experimental evidence in order to asses the reliability of the transport code, which is intensively used before and after the plasma experiments. The ASTRA transport code has been mainly used for the current diffusion calculations, though it is a very flexible and expandable tool. Section 6.2 is a combination of the section *"ECRH during the current ramp phase"* from Ref. [7] and a poster [8] presented at the Plasma Physics and Short Time-scale Physics Springmeeting of the DPG (Deutsche Physikalische Gesellschaft) in Aachen. This section describes the experiments at the TEXTOR tokamak, with 110 GHz ECRH during the current ramp phase, aimed at achieving negative central shear (NCS). Section 6.3 covers recent experiments at TEXTOR with the 140 GHz ECRH system—this system is one of the major contributions of the FOM team in the framework of the Trilateral Euregio Cluster (TEC) agreement. These experiments targeted the realisation of a quiet current ramp-up scenario with minimal MHD activity. Finally, Section 6.4 summarises the results and evaluates the reliability of the utilised numerical codes.

6.2 110 GHz ECRH during the current ramp phase

Assuming that the electron heat conductivity displays dips (so-called transport barriers) to very low values near rational values of q [9], it is attractive to control the current density profile in such a way as to make optimal use of these barriers. One way to optimise the q profile is by creating NCS, i.e., a hollow current density profile, or at least very low central shear. Both in ASDEX-Upgrade and in TCV a strong electron transport barrier and high $T_e(0)$ have been obtained in discharges with central counter-ECCD [3, 4, 12]. In these experiments, the counter-ECCD is instrumental both for sustaining and achieving NCS as well as for supplying the central electron heating. The 270 kW of the preliminary 110 GHz ECRH system was insufficient to achieve a central shear reversal in TEXTOR during the flat-top phase and, consequently, another technique was used to create NCS.

Another widely used technique to create a hollow current density profile is by means of early heating during the current rise phase of the discharge; an increased temperature leads to an increased conductivity, slowing down current penetration and resulting in a hollow current profile [14, 15]. This method has been employed in TEXTOR discharges with the aim of exploring a possible NCS regime [16]. In the experiments, a fast initial ramp (100 ms) up to I_p = 200 kA is followed by a slower ramp up to 350 kA at t = 600 ms. Early heating is provided by 1 MW of counter-NBI from t = 200 ms. In addition to providing the required plasma heating, counter-beam injection was expected to induce central counter current drive in order to attain NCS. Somewhat later, ECRH (270 kW, t = 250 - 450 ms) is applied for additional electron heating to highlight the presence of electron transport barriers. Midway through the ECRH pulse, at t = 350 ms, the electron temperature profile is measured by Thomson scattering (TS).

The polarimetry system—which measures the poloidal magnetic field and therefore can be used to reconstruct the q profile—surveyed the plasma during the current ramp phase. The evidence from polarimetry just before and after the ECRH, as well as from current diffusion calculations which include the beam-driven currents, indicates that the central shear in this phase is, at best, marginally reversed or flat. The central and/or minimum q value just before ECRH is in the range of $1.5 - 2.5$. Unfortunately, no polarimetry data are available during ECRH as a consequence of perturbations to the measurements by the presence of EC waves. In particular, during central ECRH, experimental results indicate a fast evolution of the central current profile with q dropping below 1 near the end of the ECRH pulse. The presence of the $q = 1$ surface in the plasma is justified by the appearance of sawteeths. In normal discharges without early heating, sawteeth generally appear much later. Despite the higher temperature and lower resistivity, the strong central peaking of the T_e profile leads to a faster central current penetration because of the reduced gradient length, $L = T_e|dT_e/dr|^{-1}$. The current penetration time scale is determined by the resistive diffusion time scale $\tau_\eta \sim \mu_0 \sigma L^2$. This effect is confirmed by the current diffusion calculations using the ASTRA code. Figure 6.1 shows the evolution of the minimum value of the safety factor, $q_{\min}$, and is consistent with the time of the first appearance of the sawteeth in the discharges #89932, #89937 and #89940. The faster current penetration leads to peaked

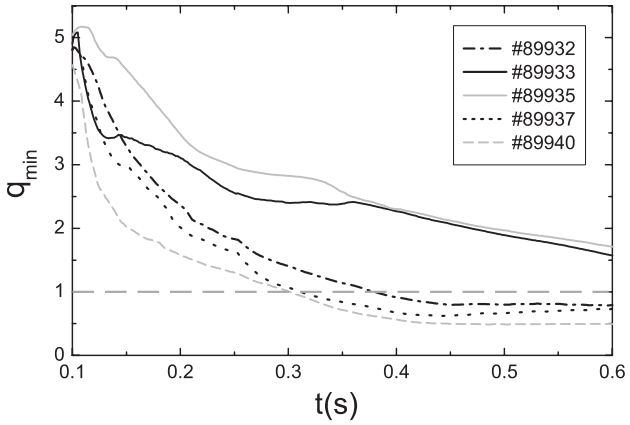

Figure 6.1: The evolution of $q_{\min}$ from current diffusion calculations using the ASTRA code for different positions of ECRH deposition: #89937 $\rho_{\text{dep}} = 0.00$, #89932 $\rho_{\text{dep}} = 0.06$, #89940 $\rho_{\text{dep}} = 0.13$, #89935 $\rho_{\text{dep}} = 0.23$, #89933 - NBI only.

current density profiles seen in Figure 6.3 and Figure 6.2 presents the corresponding safety factor profiles.

In conclusion, though an NCS regime has not been established, discharges with a broad low-shear region in the centre have been obtained. Nevertheless, the application of ECRH in this current-ramp phase have produced a number of striking observations. The T_e and n_e profiles for different positions of the ECRH deposition are shown in Figures 6.4 and 6.5, respectively. Two electron transport barriers are identified in these profiles at normalised minor radii of $\rho = 0.13$ and 0.35. The region inside the inner barrier is much larger than the width of the ECRH deposition profile (typically $\Delta\rho = 0.05$). The lack of polarimetry data during ECRH makes it impossible to link these barriers to specific values of q.

Apart from providing the necessary pre-heating, counter-NBI also proved essential for stability during central ECRH. Without NBI, ECRH during the current-ramp phase is accompanied by one or more strong core collapses. Core collapses are also observed with off-axis ECRH as seen in the central T_e evolution (Figure 6.6). A particularly strong core collapse is observed in the case where ECRH deposition coincides with the inner barrier (discharge no #89940).

Replacing partly or completely counter-NBI by co-NBI leads to increased MHD activity during ECRH as shown in Figure 6.7. Even when only part of the counter-NBI is replaced by co-NBI, the discharge evolution is strongly affected; increased MHD activity appears to prevent central current penetration, such that the central value of $q = 1$ and sawteeth are never attained. Instead, the discharge typically ends in a disruption some time after the ECRH. Only the combination of early additional heating with counter- NBI plus a subsequent pulse of central ECRH results in an evolution towards a stable sawtoothing discharge, while current ramp-up with only ohmic heating is stable at these low current ramp rates. When the current ramp-up is too fast with ohmic heating alone one gets similar MHD phenomena comparable to the lower ramp rate with early additional heating. Current diffusion calculations confirm that only with the combination of counter-NBI and central ECRH the central q value drops below 1 near

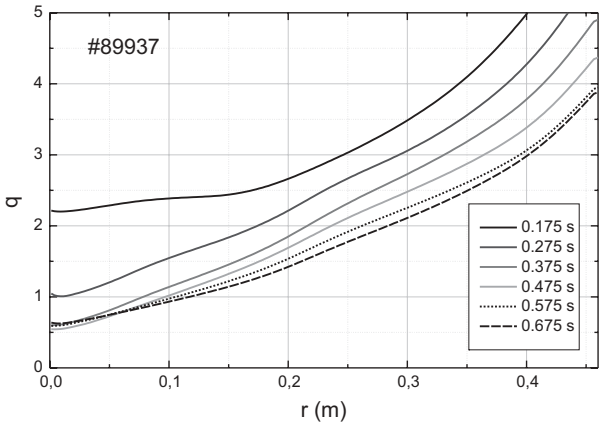

Figure 6.2: Safety factor profiles during the current ramp-up phase calculated using the ASTRA code for the discharge #89937 with the central ECRH.

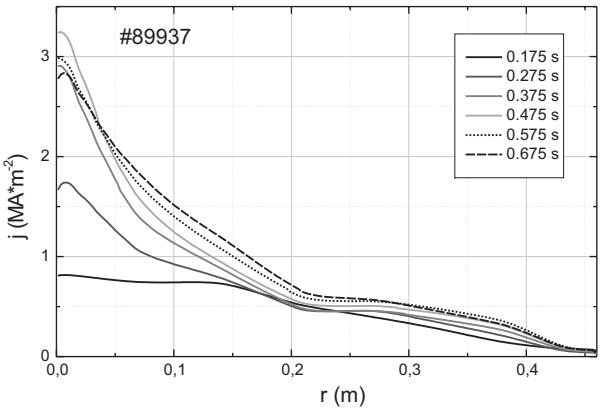

Figure 6.3: Plasma current density profiles during the current ramp-up phase calculated using the ASTRA code for the discharge #89937 with the central ECRH.

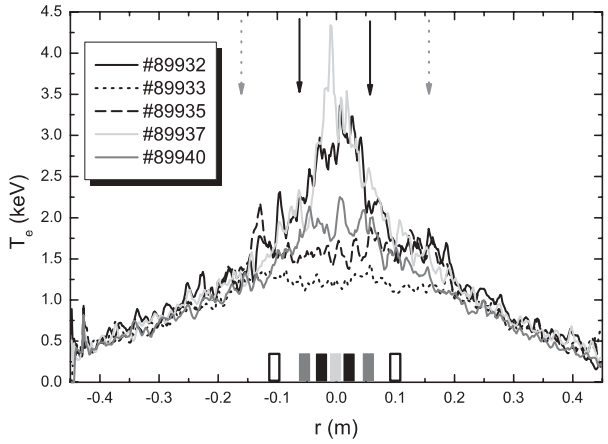

Figure 6.4: T_e profiles from Thomson scattering at t = 350 ms for different positions of ECRH deposition: #89937 ρ_{dep} = 0.00, #89932 ρ_{dep} = 0.06, #89940 ρ_{dep} = 0.13, #89935 ρ_{dep} = 0.23, #89933 - NBI only. The arrows indicate the positions of transport barriers and bars indicate the positions of ECRH deposition.

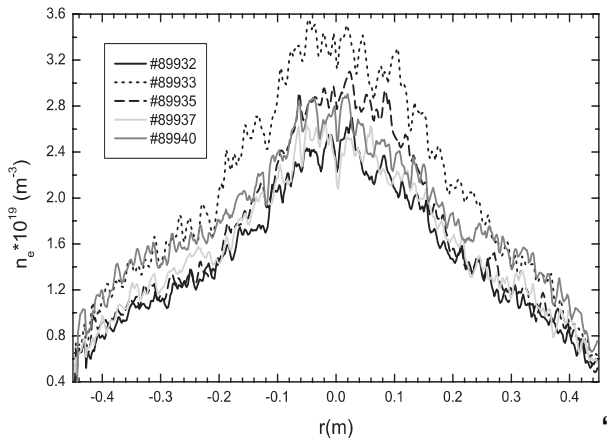

Figure 6.5: n_e profiles from Thomson scattering at t = 350 ms for different positions of ECRH deposition: #89937 ρ_{dep} = 0.00, #89932 ρ_{dep} = 0.06, #89940 ρ_{dep} = 0.13, #89935 ρ_{dep} = 0.23, #89933 - NBI only.

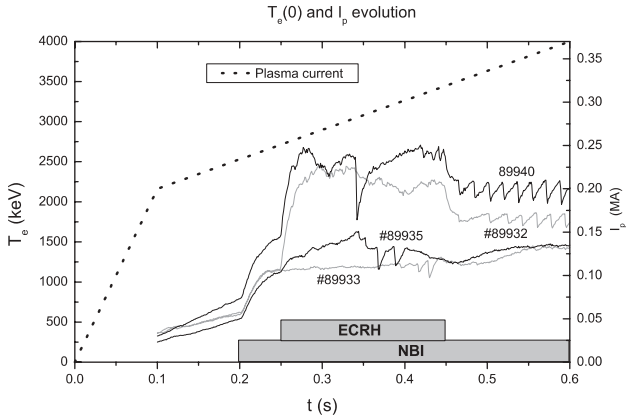

Figure 6.6: The evolution of $T_e(0)$ from ECE for different positions of the ECRH deposition: #89932 $\rho_{\rm dep} = 0.06$, #89940 $\rho_{\rm dep} = 0.13$, #89935 $\rho_{\rm dep} = 0.23$, #89933 - NBI only.

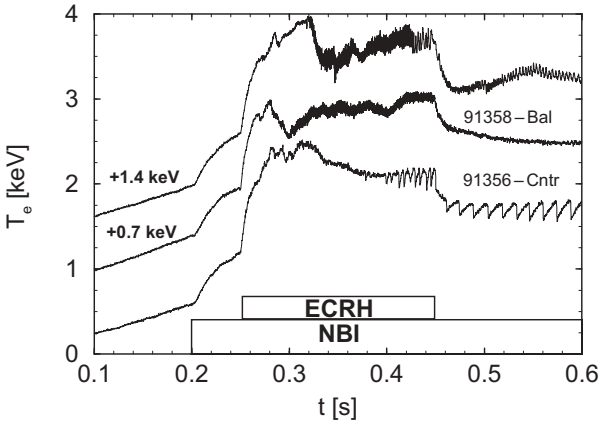

Figure 6.7: The evolution of $T_e(0)$ from ECE for different ratios of counter- and co-NBI: #91356 counter-NBI; #91358 balanced NBI; #91355 co-NBI.

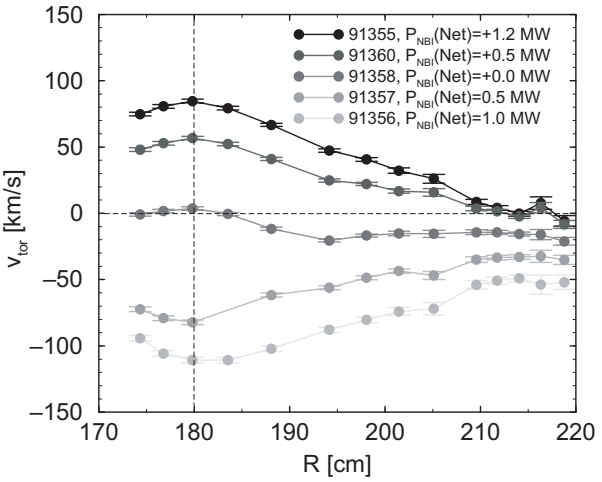

Figure 6.8: Profiles of rotation velocity (at t = 350-400 ms) from CXRS for discharges with different ratios of co- and counter-NBI. For each discharge, the net current driving power $P_{\rm co} - P_{\rm counter}$ is quoted. The total NBI power in all cases is 1.2 MW.

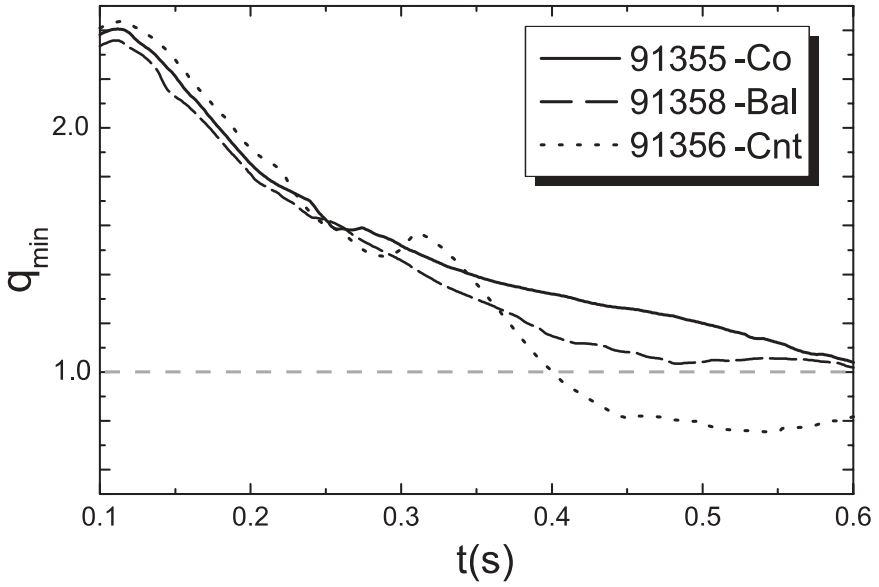

Figure 6.9: Evolution of the minimal value of the safety factor for discharges with different ratios of co- and counter-NBI.

the end of the ECRH pulse (see Figure 6.9). With either balanced or co-NBI the current density profile remains significantly broader. This might explain the susceptibility of these discharges to, for example, the $m = 2$, $n = 1$ tearing mode, which plays a major role in the subsequent evolution finally ending in a disruption. The differences in rotation between these discharges (Figure 6.8) might also play a role in their stability. It is seen that in the presence of the counter-NBI injection the plasma has a non-zero edge velocity which might improve the plasma stability by the effect of eddy currents in the vacuum vessel [13]. It is noted here that a later start of co-NBI, during the current flat top phase, is an often used method at TEXTOR to prevent or suppress MHD $m = 2$, $n = 1$ modes [17].

6.3 MHD free current ramp phase with the assistance of 140 GHz ECRH

A plasma current ramp-up with a minimum of MHD activity is a basis for a healthy flat-top phase. In the series of experiments at TEXTOR we have compared two different current ramp up rates combined with early additional heating. The fast initial ramp(0-100 ms) up to $I_p = 150$ kA is followed by a ramp up to 360 kA at $t = 0.5$ s for discharges #96507, #96518, #96519 and #96505 (see Figure 6.10). A slower ramp up to 360 kA at $t = 1.0$ s is employed in #96505 and #96521. All discharges experienced additional early NBI injection starting from 0.1 s. For some discharges ECRH is applied for additional electron heating during the current rise (see Table 6.1).

Figure 6.11 shows the line average electron density as a function of time during the current ramp up phase. The blue/red lines correspond to the discharges with a slower/faster ramp rate. It is seen that in the presence of dominant NBI heating

#Discharge	96507	96518	96519	96520	96505	96521
I_p ramp rate MA/s	0.5	0.5	0.5	0.5	0.22	0.22
NBI1, co- , MW	0.90	0.0	0.0	0.0	1.20	0.0
NBI2, cnt-, MW	0.45	1.2	1.2	1.2	0.25	1.2
I_{cd}^{nbi}, kA	+30	-80	-80	-80	+70	-80
ECCD, kA	0.0	0.0	10	0.3	0.0	14
ECRH (s)	no	1.5-3	0.2-1.2	0.2-1.2	no	0.2-1.2

Table 6.1: The parameters of the additional heating during the current ramp up with 800 kW ECRH at 140 GHz.

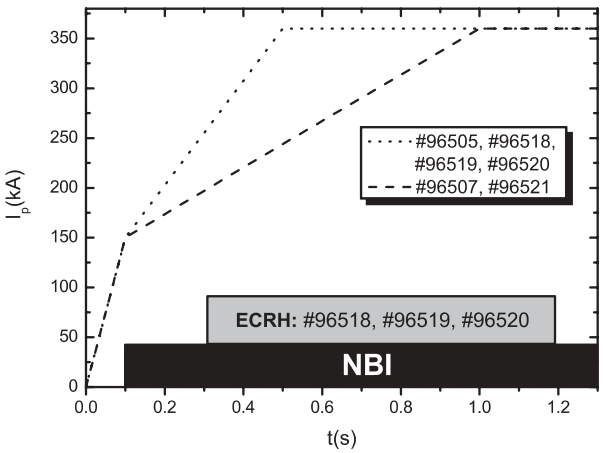

Figure 6.10: The total plasma current as a function of time.

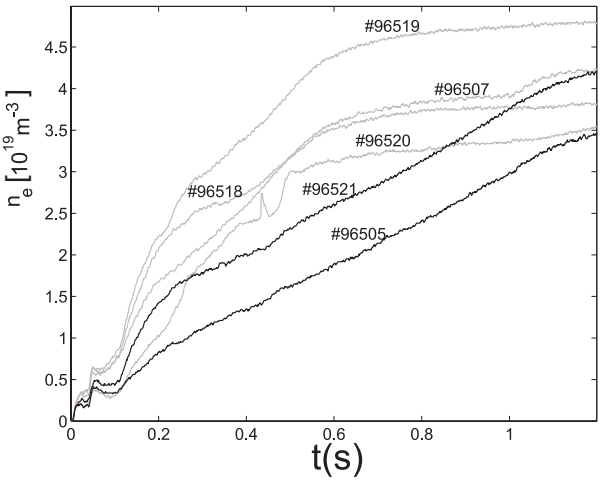

Figure 6.11: The line-averaged electron density as a function of time for different discharges during the current ramp up phase. The gray/black lines correspond to the fast/slow current ramp rate.

the slower current ramp gives a smoother rise of the plasma density. Moreover, with the faster ramp rate and additional NBI it is very difficult to keep the density within predefined limits.

The signal from Mirnov coils has been used to identify the presence of MHD activity. The Figure 6.12 combines the signal from the same poloidal Mirnov coil for all discharges presented here. As in Figure 6.11 the red/blue colour marks discharges with faster/slower current ramp rate. The discharges #96507 and #96505 with only co-NBI injection show almost no evidence of the MHD activity, whereas the rest of discharges, all with counter-NBI injection, exhibit considerable MHD activity. The presence of ECRH and a small amount of ECCD in some cases (see Table 6.1) does not affect the character of the MHD activity, since the NBI is the dominant additional heating. The difference in the plasma stability in presence of counter-NBI when comparing to discharges from previous Section might be explained by large variations in the wall conditions. A large density of neutrals at the edge of the plasma reduces the plasma

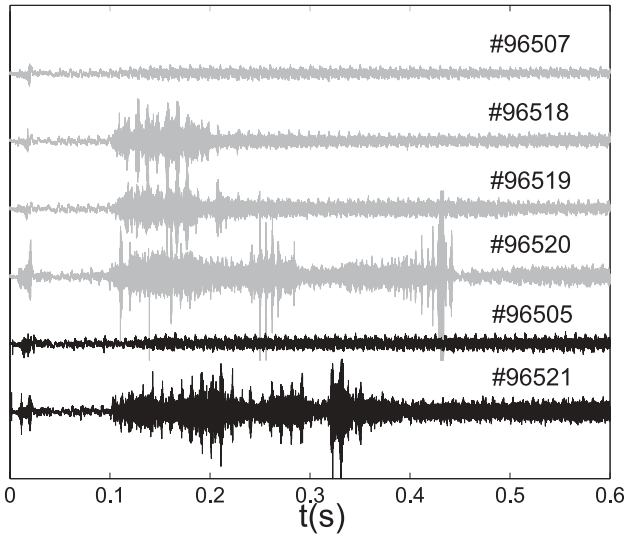

Figure 6.12: The raw signal from the poloidal Mirnov coil for different discharges during the current ramp phase. The gray/black lines correspond to the fast/slow current ramp rate.

edge rotation and, thereby, decreases the stabilising effects of eddy currents in the vacuum vessel, which were present in the previous experiments.

The two discharges #96507 and #96505 with a quiet ramp phase have been selected for the current diffusion calculations. The ASTRA code has been used to calculate the current penetration on the basis of the experimental temperature and density profiles. The NBI current drive was calculated with the NBCD (see Section 2.5.3) procedure. The Figure 6.13 shows the evolution of the central q_0 value. The initial conditions for the q profile were fixed for both discharges to highlight the difference in the evolution. The calculation show that the time when q_0 drops below unity is just before the first appearance of the sawteeth (see Figure 6.14).

Even though the current penetration calculations can be inaccurate for the discharges with significant MHD activity, it might be useful to analyse the discharge evolution on the well known $l_i - q$ operation space stability diagram [18], where l_i is a plasma internal inductance. The empirical stability boundaries on this diagram manifest two constraints for plasma operation during the current ramp up. The lower sawtooth-like boundary refers to the resistive tearing mode instability, which produces magnetic reconnection localised at the rational $q = m/n$ surface. This instability occurs when the current profile becomes too broad and therefore is associated with low values of l_i. The upper boundary refers to the high values of the plasma density, which leads to the edge cooling and current density profile shrinkage, hence, higher values of l_i. The excessive current profile shrinkage leads to the disruption from the 'density limit' category. The Figure 6.15 presents all discharges on the $l_i - q$ diagram with empirical stability boundaries taken from the JET tokamak. It is seen that discharges in TEXTOR with the additional counter-NBI injection have trajectories lower than with only co-NBI and therefore closer to the stability boundary.

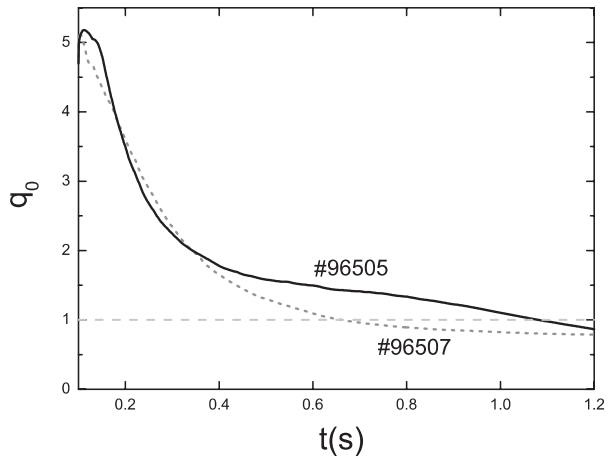

Figure 6.13: Evolution of the minimal value of the safety factor for discharges without MHD.

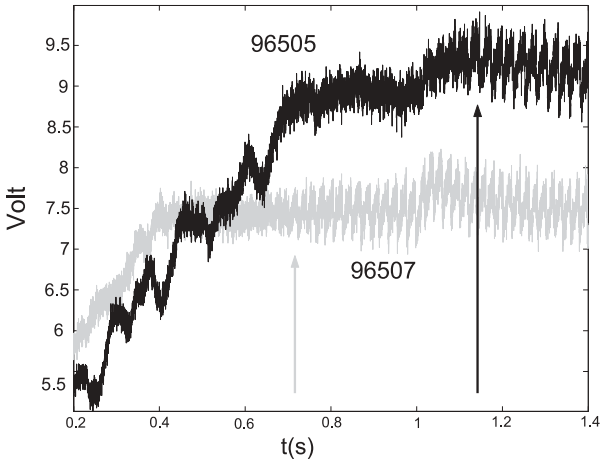

Figure 6.14: The traces of the ECE channels for the MHD-free discharges. The arrows indicate the appearance of the sawtooth oscillations.

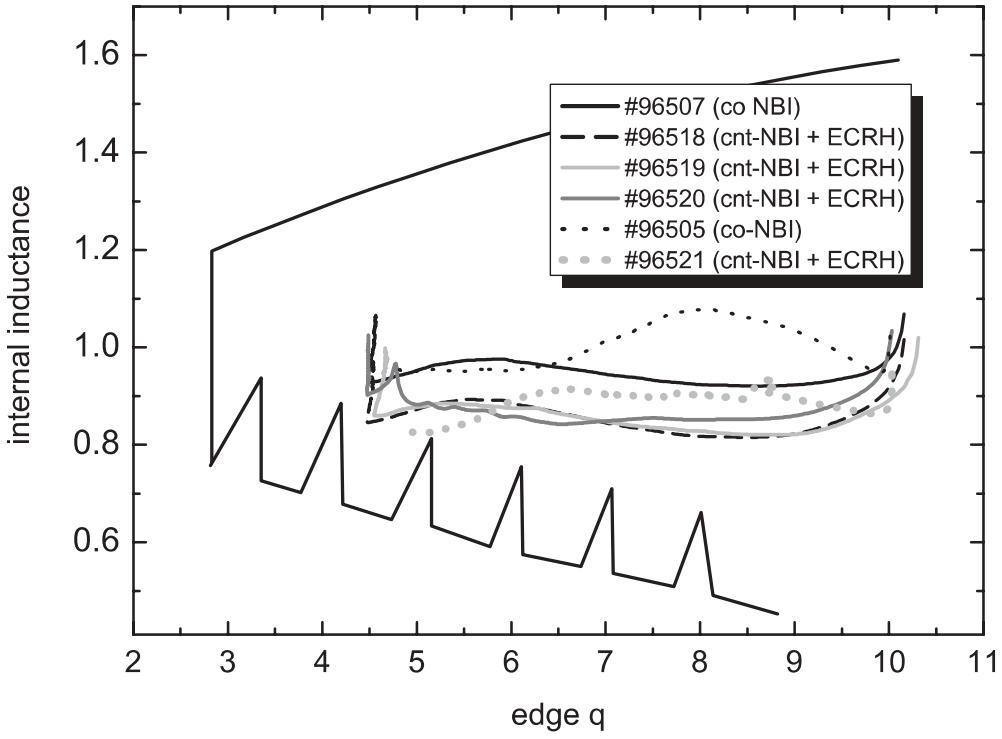

Figure 6.15: The internal plasma inductance as a function of the edge safety factor. The stability boundaries are indicative and taken from the calculations for TCV and JET tokamaks.

6.4 Conclusions

Current diffusion calculations have been performed to interpret the results from discharges with preliminary 110 GHz gyrotron as well as with its successor 140 GHz gyrotron. Both these experimental programmes concentrated on the plasma current ramp phase with additional heating. The most important conclusions are summarised as follows.

In the current ramp phase, central ECRH led to a faster current penetration and an early start of sawteeth near the end of ECRH, though only when combined with early additional heating from dominant counter-NBI. The faster current penetration is determined by a smaller resistive time scale, $\tau_R \sim \mu_0 \sigma L^2$, because of the reduced gradient length, $L = T_e |dT_e/dr|^{-1}$, in spite of the increased conductivity. The observations of current penetration are in quantitative agreement with the transport calculations by the ASTRA code. The presence of electron transport barriers have been observed during the current ramp-up phase. A finite edge rotation, controlled by NBI, improves the plasma stability by the effect of eddy currents in the vacuum vessel.

The decrease in the MHD activity during the current ramp phase can be achieved in TEXTOR by slowing down the ramp rate to 0.22 MA/s. However, the complete suppression of the MHD activity is not reached due to the presence of the additional counter-NBI. The discharges with only co-NBI injection during the current ramp up phase have shown no presence of MHD activity and, therefore, could be analysed with the ASTRA transport code. The presence of MHD activity in the discharges with counter-NBI might be explained by the absence of plasma edge rotation due to the different wall conditions. Again the results of the ASTRA simulations are in a quantitative agreement with experiments.

In conclusion,the ASTRA transport code proved to be a valuable and very flexible tool not only for interpreting existing experimental data, but also for predictive analysis.

Bibliography

[1] ITER Physics Expert Group *et al* 1999 *Nuclear Fusion* **39** 2577

[2] Rimini F G 2005 *Plamsa Phys. Control. Fusion* **47** 869

[3] Günter S *et al* 2000 *Phys. Rev. Lett.* **84** 3097

[4] Wolf R C *et al* 2001 *Nuclear Fusion* **41** 1259

[5] Greenfield C M *et al* 1999 *Nuclear Fusion* **39** 1723

[6] Pereverzev G *et al* August 1991 *ASTRA, Report IPP 542*

[7] Westerhof E *et al* 2003 *Nuclear Fusion* **43** 1371

[8] Merkulov A *et al* 2003 Safety factor profile evolution during the current ramp phase 30^{th} *IoP Annual Plasma Physics Conference* Aachen, Germany, March 24-28, P10.17 (poster)

[9] Hogeweij G M D 1998 *Nuclear Fusion* **38** 1881

[10] Poli E *et al* 2001 *Computer Physics Communication* **136** 90

[11] Wesson J 2004 *Tokamaks*

[12] Pietrzyk Z A *et al* 2001 *Phys. Rev. Lett.* **86** 1530

[13] Fitzpatrick R 1993 *Nuclear Fusion* **33** 1049

[14] Wolf R C 2003 *Plamsa Phys. Control. Fusion* **45** R1

[15] Sips A C C 1998 *Plamsa Phys. Control. Fusion* **40** 647

[16] Westerhof E *et al* 2001 Electron cyclotron resonance heating in the current ramp-up phase of TEXTOR-94 28^{th} *EPS Conf. on Control. Fusion and Palsma Physics (Maderia, Portugal, 18-22 June 2001)* vol 25A (ECA)

[17] Krämer-Flecken A *et al* 2003 *Nuclear Fusion* **43** 1437-1445

[18] Wesson J *et al* 1989 *Nuclear Fusion* **29** 641

Chapter 7

Conclusions & Outlook

This thesis presented several topics discussing the plasma profiles, transport and stability which had been manipulated through localised electron cyclotron heating (ECRH) and electron cyclotron current drive (ECCD). The main conclusions are summarised as follows.

In the context of the critical shear model for the sawtooth oscillation, a simplified model for the poloidal field evolution has been presented in Chapter 4. The results of the model calculations can be summarised in a criterion for the non-inductive current which is required for sawtooth period control

$$I_{cd} \gtrsim 2 \left(\frac{\Delta r}{r_{q=1}} \right)^2 I_{q=1}, \tag{7.1}$$

where Δr is the Gaussian width of the non-inductive current profile, $r_{q=1}$ is the radius of the $q = 1$ surface and $I_{q=1}$ is the total plasma current inside $q = 1$. The predictions of the sawtooth period behaviour during ECRH and ECCD are in qualitative agreement with experimental observation on TCV, ASDEX-Upgrade and TEXTOR. These observations clearly indicate the lengthening of the sawtooth period with co-ECCD just outside, and with counter-ECCD just inside, the $q = 1$ surface. Since non-inductive current drive always comes with additional heating, the effect of pure ECCD has been identified by normalising the sawtooth period as a function of the deposition radius to a similar discharge with only ECRH. The observations confirm the assumption that the critical shear at the $q = 1$ surface determines the moment of the sawtooth crash at values that are in agreement with theoretical predictions.

For the the work presented in Chapter 4, a possible future extension might be based on the coupling of the sawtooth trigger criterion with a transport code. In this way, the model could predict the exact sawtooth period and a direct comparison with experiment may be made. Moreover, the advantage of the combination with a transport code is that the effects of ECCD and ECRH can be treated together in a self-consistent manner.

Chapter 5 discussed the model of current penetration during ECCD on the basis of a Fokker-Planck code. The magnetic diffusion in this model evolves consistently with the momentum distribution function from the Fokker-Planck equation. Therefore, the plasma conductivity receives a more complete treatment than in the stan-

dard model—where the conductivity is calculated assuming a thermal velocity distribution of the electrons. Typical ECCD scenarios with off- and near-axis depositions have been modelled and compared with the standard model of current diffusion calculations. In conclusion, Harvey's non-linearity criterion for the injected EC power $[P_{\mathrm{EC}}(\mathrm{W/cm^3})]/[n_e(10^{13}\,\mathrm{cm^{-3}})]^2 \geq 0.5$ can be used to identify situations where the synergy between non-inductive and ohmic currents starts to play a role. When this criterion is approached or exceeded for the co-ECCD the synergetic effects are accompanied with a large population of suprathermal electrons and the current penetration is slowed. The synergy between counter-ECCD and the ohmic current leads to the decrease of the total driven current and the predicted generation of suprathermal electrons is significantly smaller than during co-ECCD.

The calculations presented in Chapter 5 await experimental investigation. Such experiments can only be performed marginally in the TEXTOR tokamak, due to the lack of proper diagnostics. The evolution of the parallel electric field on the current diffusion time scale poses demanding requirements for such a diagnostic. However indirectly one could observe the delay in current penetration time at high values of the Harvey criterion by careful evaluation of the loop voltage evolution or the change in the sawtooth period.

The experimental observations in Chapter 6, during the current ramp-up phase are split in two groups. In the first group, fast current penetration during ECRH has been observed due to the peaked temperature profile and increased gradient length. Moreover, electron barriers were present during the current ramp. The second group was aimed at minimising the MHD activity during the ramp phase. The discharges with co-NBI have shown no MHD activity, while the presence of counter-NBI has led to detectable MHD activity. The ASTRA transport code has been used to calculate the current penetration for the discharges with no MHD. The time of the appearance of the $q = 1$ surface is in agreement with the time of first observations of sawteeth in the experiment. In conclusion, the ASTRA transport code can be employed to analyse current diffusion of the discharges provided that there is no substantial MHD activity.

The experiments outlined in Chapter 6 could be extended in order to observe the stability boundary of TEXTOR plasmas on the diagram of internal plasma inductance, l_i, vs. the edge safety factor, q_a. The stability boundaries on this diagram could be obtained from theory and confirmed by future experimental observations by manipulating l_i with ECCD.

Summary

The work presented in this thesis addresses several topics from the physics of the magnetically confined plasma inside a tokamak. At the moment, the tokamak is the most successful concept for becoming a future thermonuclear reactor. However, there are plenty of physics and engineering problems to surpass before the prototype can become an economically and environmentally feasible device.

The plasma in the tokamak experiences periodic oscillations of the central temperature and density when the safety factor, q, drops below unity on-axis. The safety factor, q, is a measure of the helicity of the magnetic field line. These oscillations are called the sawtooth instability and are the subject of the first part of this thesis. The sawtooth oscillations are characterised by the relatively slow rise phase, when the central temperature increases, and a following crash phase, when the central temperature drops. The energy, particles and plasma current are redistributed during the sawtooth crash. Obviously, this leads to a confinement degradation and moreover, the sawtooth instability can trigger potentially other more dangerous instabilities, such as a neoclassical tearing mode. The sawtooth period control is realised on the basis of the sawtooth trigger model, derived by Porcelli. The main idea of this model is that the sawtooth crash is triggered when the magnetic shear at the $q = 1$ surface, s_1, reaches a critical value which depends on the local plasma parameters. The magnetic shear, s, is a measure for the rate of change in the direction of the field line as a function of the position in the plasma. The sawtooth period can be changed by affecting the evolution of s_1. The effects of the electron cyclotron current drive (ECCD) on the shear evolution are studied with a simple model for the poloidal field evolution. The results of the model are summarised in a form of a criterion for the amount of the non-inductive current drive required for sawtooth period control. The effects of the ECCD have been studied in the TEXTOR tokamak in order to confirm the outcome of the model. The observations are complicated by the unavoidable presence of concurrent heating, which also affects the sawtooth period. The effects of additional heating have been separated from the effects of current drive by normalising the sawtooth period, as a function of the power deposition radius, to a case with heating only. The results are in qualitative agreement with the predictions of the theory and confirm that the shear around the $q = 1$ surface determines the moment of the sawtooth crash.

The next topic addresses the current diffusion in the presence of the ECCD. It is known that the synergy between non-inductively driven current and the ohmic current can affect the current penetration. However, the standard method of calculations, which assumes neoclassical plasma resistivity, cannot describe the synergistic effects. We propose a model which combines a Fokker-Planck code and magnetic diffusion

calculation in a self-consistent manner; where the plasma resistivity is approximated from the Fokker-Planck code at every time step. In this way the parallel electric field is no longer a constant input profile for the Fokker-Planck code, but is a result of calculations of the magnetic diffusion. This model allowed us to identify situations where the synergy between the driven and the ohmic currents becomes significant and affects the current penetration. Both the ECCD power and the electron density have been varied over a wide range of parameters, thus changing the well known non-linearity criterion for ECCD after Harvey. This criterion indicates the non-linear behaviour of the current drive efficiency and also appears to be a good predictor for the synergistic effects. The results are compared with the standard method of calculations which were supplied by the ASTRA transport code. The standard method and the Fokker-Planck code with the self-consistent electric field show similar results in the absence of the synergy and therefore for low values of the Harvey parameter. For co-ECCD and high values of the Harvey parameter substantial synergy between ECCD and the ohmic current is observed and leads to the generation of a large population of suprathermal electrons and slows down the current penetration. The synergy between counter-ECCD and the inductive current results in a decrease of the total driven current and a much smaller population of suprathermal electrons.

Another plasma stability problem has been studied during the current ramp-up phase. Quiet and MHD free current ramp-up is a necessary requirement for a long and efficient flat-top phase. The current penetration in the plasma scenarios with various plasma ramp-up rates has been modelled with the ASTRA transport code. It is shown that in the absence of MHD activity the predictions of the ASTRA code are in a agreement with the experimental results.

Samenvatting

Het werk dat in deze thesis gepresenteerd wordt, belicht verscheidene onderwerpen van de fysica van magnetisch opgesloten plasma's. Momenteel is de tokamak het meest succesvolle concept om uit te groeien tot een toekomstige thermonucleaire reactor. Echter, vele fysische en technische horden moeten nog genomen worden vooraleer het prototype een milieuvriendelijke en economisch aanvaardbare machine kan worden.

Het plasma in een tokamak vertoont periodieke oscillaties van de centrale temperatuur en dichtheid wanneer de veiligheidsfactor, q, kleiner wordt dan één op de magnetische as. De veiligheidsfactor, q, is een maat voor de heliciteit van een magnetische veldlijn. Deze oscillaties worden zaagstand instabiliteiten genoemd en zij vormen het onderwerp van het eerste deel van dit proefschrift. De zaagtand instabiliteiten worden gekarakteriseerd door een relatief langzame fase waarin de centrale temperatuur toeneemt, gevolgd door een plotselinge instorting (crash) van de centrale temperatuur. De energie van het plasma, de deeltjes en de plasmastroom worden tijdens de zaagtand crash herverdeeld. Uiteraard leidt dit tot een degradatie van de opsluiting en daarenboven kan de zaagtand instabiliteit andere, nog gevaarlijker instabiliteiten aanslaan, zoals bijvoorbeeld een neoklassieke 'tearing mode'. Controle over de zaagtandperiode wordt gerealiseerd op basis van het zaagtand trigger model, opgesteld door Porcelli. Het basisidee van dit model is dat de zaagtand crash ingezet wordt wanneer de magnetische afschuiving of 'shear' op het q=1 oppervlak, s_1, een kritische waarde bereikt. Deze kritische waarde hangt af van de lokale plasma parameters. De magnetische shear, s, is een maat voor de verandering in richting van magnetische veldlijnen als functie van de positie in het plasma. De zaagtandperiode kan veranderd worden door de evolutie van s_1 te beïnvloeden. De effecten van elektron cyclotron gedreven stroom (ECCD) op de evolutie van de magnetische shear zijn bestudeerd met behulp van een eenvoudig model voor de evolutie van het poloïdale veld. De resultaten van het model zijn samengevat in de vorm van een criterium voor de hoeveelheid niet-inductief gedreven stroom die vereist is voor de controle van de zaagtandperiode. De effecten van ECCD zijn experimenteel onderzocht in de TEXTOR tokamak, om zodoende de conclusies van het model te bevestigen. De observaties zijn echter gecompliceerd tengevolge van de eveneens aanwezige verhitting door elektron cyclotron straling. Deze verhitting beïnvloedt immers ook de zaagtandperiode. De effecten van verhitting werden ontkoppeld van de effecten door stroom aandrijving, door de zaagtandperiode te normaliseren met betrekking tot de situatie van enkel verhitting, als functie van het gedeponeerde vermogen. De resultaten zijn kwalitatief in overeenstemming met de voorspellingen uit de theorie en bevestigen dat de magnetische shear rondom het q=1 oppervlak het moment van de zaagtand crash bepaalt.

Een volgend onderwerp behandelt stroomdiffusie indien de stroomdichtheidsverdeling wordt verandert door instraling van electron cyclotron resonante microgolven (ECCD). Het is bekend dat de synergie tussen niet-inductief gedreven stroom en Ohmse stroom de stroompenetratie door magnetische diffusie kan beïnvloeden. Standaard berekeningsmethoden, waarbij neoklassieke resistiviteit van het plasma wordt verondersteld, kunnen echter deze synergetische effecten niet beschrijven. Wij stellen een model voor dat een Fokker-Planck code combineert met een magnetische diffusie berekening, en dit op een zelfconsistente manier; waarbij de resistiviteit van het plasma op elk tijdstip wordt benaderd met behulp van de Fokker-Planck code. Op deze wijze is het parallelle elektrische veld niet langer een constante invoer parameter voor de Fokker-Planck code, maar een resultaat van de magnetische diffusie berekeningen. Dit model stelde ons in staat situaties te identificeren waarbij de synergie tussen gedreven en Ohmse stroom belangrijk wordt en de stroompenetratie beïnvloedt. Zowel het ECCD vermogen als de elektronendichtheid werden gevarieerd over een brede gebied van waarden en zodoende werd ook het welbekende niet-lineariteitscriterium voor ECCD van Harvey veranderd. Dit criterium geeft een indicatie voor het niet-lineaire gedrag van de efficiëntie van de stroomaandrijving en blijkt eveneens de synergetische effecten goed te voorspellen. De resultaten zijn vergeleken met de standaard berekeningsmethode, geleverd door de ASTRA transport code. De standaard methode en de Fokker-Planck code met zelfconsistent elektrisch veld, vertonen gelijkaardige resultaten in afwezigheid van synergie en dus bij lage waarden van de Harvey parameter. Voor co-ECCD en hoge waarden van de Harvey parameter is een substantiële synergie tussen ECCD en Ohmse stroom waargenomen, die leidt tot de generatie van een grote populatie aan superthermische elektronen en een afremming van de stroompenetratie door magnetische diffusie. De synergie tussen counter-ECCD en de inductieve stroom resulteert in een afname van de totaal gedreven stroom en een veel kleinere populatie van superthermische elektronen.

Een ander probleem betreffende plasma stabiliteit werd onderzocht gedurende de opbouw fase van de plasma stroom. Een rustige en MHD-vrije stroomtoename is noodzakelijk voor een goede daaropvolgende 'flat-top' fase. De stroom penetratie voor verscheidene plasma scenario's met verschillende snelheden van stroomtoename werd gemodelleerd met de ASTRA transport code. Het is aangetoond dat in afwezigheid van MHD activiteit de voorspellingen van de ASTRA code in overeenstemming zijn met de experimentele resultaten.

Acknowledgements

I would like to thank everyone who contributed to this thesis, especially my co-promotor Dr. Egbert Westerhof and promotor Prof. Dr. Chris Shüller. Dr. Westerhof has been my daily supervisor and offered great support and thorough scientific guidance on an everyday basis. Prof. Dr. Shüller was an example of the perfect promotor; regularly supervising his student during the study period and not losing his grip until the thesis was ready for public defence.

Although I was a PhD student with the FOM Institute for Plasma Physics "Rijnhuizen" in the Netherlands, this work was performed at the Institut für Plasmaphysik, Forschungszentrum Jülich, Germany. I therefore want to thank the scientists from the TEXTOR team who helped me to prepare, perform and analyse various plasma experiments. Special thanks go to the ECW technical support group who made sure that both gyrotrons operated reliably.

I am thankful to Dr. Roger Jaspers for discussions on technical aspects of the TEXTOR. I thank Prof. Dr. N. J. Lopes Cardozo for his comments on my work during his visits to Jülich. I am also grateful to Dr. Hugo de Blank for his elaborate remarks on Chapter 3 of this thesis. I would like to thank Dr. Dick Hogeweij who introduced me to the ASTRA code, which contributed greatly to the simulations presented in this work. I am grateful to Dr. Fenton Glass for his patient review and corrections of the whole text. Thanks also to Maarten de Bock for translating the summary into Dutch.

Finally, I would like to thank my family—especially my wife Maria—for their love and constant support.

Curriculum Vitae

I was born on 27th August, 1980 in Chernigov, USSR/Ukraine. In 1996 I finished the Ukrainian Phys. Math. Lyceum and entered the National Taras Shevchenko University of Kiev. In July 2001 I graduated from the Radiophysical Faculty of this university and received a Specialist Degree in Radiophysics with distinction. My diploma work, "Inhomogeneous states induced by the strong magnetic field in the ladder AFM with impurities" was performed under the supervision of Prof. Dr. Boris Ivanov. After several months of employment at the National Institute of Cybernetics, Kiev, Ukraine, I started research towards a PhD at the FOM Institute for Plasma Physics 'Rijnhuizen' (Nieuwegein, the Netherlands) in February 2002. The work presented in this thesis was carried out at the Institut für Plasmaphysik, Forschungszentrum Jülich, Germany. From the 1st of July 2006 I will begin work in the Macromolecular Ion Physics group at the AMOLF Institute, Amsterdam, the Netherlands.